CWP-987

ELASTIC TIME-REVERSE IMAGING AND TRANSMISSION TOMOGRAPHY FOR MICROSEISMIC AND DAS VSP DATA

by

Can Oren

A thesis submitted to the Faculty and the Board of Trustees of the Colorado School of Mines in partial fulfillment of the requirements for the degree of Doctor of Philosophy (Geophysics).

Golden, Colorado

Date ____________________

Signed: ____________________

Can Oren

Signed: ____________________

Dr. Jeffrey C. Shragge
Thesis Advisor

Golden, Colorado

Date ____________________

Signed: ____________________

Dr. Paul C. Sava
Professor and Head
Department of Geophysics

ABSTRACT

Wavefield migration and tomography are considered to be state-of-the-art methodologies used for subsurface geological characterization. Seismic tomography produces accurate velocity models that commonly serve as input into seismic migration algorithms that produce high-quality passive-source (e.g., microseismic) images or structural images of geological interfaces constructed using controlled-source energy (e.g., vibroseis truck or dynamite). Most existing wavefield migration and tomography techniques employed in the oil and gas industry are well-developed under the acoustic assumption. One of the main shortcomings of this assumption is that conventional acoustic imaging algorithms generally use single-component P-wave data and thus do not account for multicomponent elastic (P- and S-mode) data that can provide additional subsurface information such as fracture distributions and elastic properties. To account for more accurate wave physics in passive and active seismic scenarios, I propose a suite of novel full-wavefield methods for imaging and multiparameter (i.e., P- and S-wave) model estimation in elastic media.

Passive-style image-domain elastic tomography operates with multicomponent P- and S-wave first-arrival waveforms of a microseismic event and optimizes the background velocity model by improving the quality of source images constructed by a procedure called time-reverse imaging (TRI). To formulate a robust image-domain inversion framework, I develop a 3D extended imaging condition for surface-recorded microseismic data based on the correlation of individual P- and S-wavefield energy as well as the energy norm. The proposed PS energy imaging condition not only effectively locates microseismic events for complex isotropic/anisotropic models but also provides useful information about P- and S-wave velocity model as well as anisotropy parameter $[\epsilon, \delta, \gamma]$ accuracy.

Based on the kinetic energy term of the PS energy imaging condition, I propose an image-domain elastic wavefield tomography framework to build plausible P- and S-wave velocity models that improve the quality of microseismic event images. I present synthetic numerical experiments to demonstrate that the estimated model parameters result in enhanced source images, which greatly reduce event mispositioning errors. Finally, I apply the developed image-domain elastic inversion method on an active-source distributed acoustic sensing 3D vertical seismic profiling data set acquired in the North Slope of Alaska to investigate potential methane gas hydrate reservoirs. I exploit source-receiver reciprocity to create an acquisition configuration that resembles passive-seismic surface monitoring scenarios. I first validate the accuracy of the inverted elastic velocity models using a TRI-based source location analysis. Next, I construct numerous 3D structural images of the area of interest through elastic reverse time migration (RTM). The elastic RTM results exhibit coherent reflectivity associated with a complex near-surface ice-bearing permafrost zone, as well as two gas hydrate reservoirs that satisfactorily match the existing log data in well-ties due to the improved velocity model estimates.

TABLE OF CONTENTS

LIST OF FIGURES

LIST OF ABBREVIATIONS

Center for Wave Phenomena . . . . CWP

Colorado School of Mines . . . . CSM

Distributed Acoustic Sensing . . . . DAS

European Association of Geoscientists and Engineers . . . . EAGE

Full Waveform Inversion . . . . FWI

Migration Velocity Analysis . . . . MVA

Reverse Time Migration . . . . RTM

Signal-to-Noise Ratio . . . . S/N

Society of Exploration Geophysicists . . . . SEG

Time-Reverse Imaging . . . . TRI

Vertical Seismic Profiling . . . . VSP

ACKNOWLEDGMENTS

There are many people that I would like to acknowledge for making this PhD journey at Mines an amazing one within the past three and a half years. First and foremost, I am grateful to my advisor Dr. Jeffrey Shragge for accepting me into the PhD program at Center for Wave Phenomena (CWP), as well as for all his support and guidance throughout my graduate studies at Mines. It was a real privilege working with Jeff and I have enjoyed all our technical/non-technical conversations during our meetings. I have learned a great deal from Jeff, which has helped me grow on both professional and personal levels.

I would like to thank my thesis committee members, Dr. Paul Sava, Dr. Ebru Bozdag, Dr. Mahadevan Ganesh, and Dr. Gabriel Walton for kindly serving on my committee and their insightful comments on my thesis. The knowledge I gained through Paul's wavefield seismic imaging class has greatly contributed to my thesis projects. I also thank the rest of the CWP faculty, Dr. Ilya Tsvankin and Dr. Roel Sneider, for their support in various aspects of my research. I have benefited a lot from Ilya's advanced seismology class while working on the anisotropic imaging project presented in Chapter 3.

I would like to thank the CWP consortium sponsors, whose financial support made this research possible. Special thanks to Michelle Szobody, Debra Marrufo, Noelle Vance, Gina Schwieger, and Emilia Clayton for their continuous administrative support, which has made my life in graduate school much easier. I am deeply grateful to Diane Witters not only for her technical support to improve my writing and communication skills, but also for her sincere friendship over the years. I acknowledge Dr. Ken Larner for his numerous feedback to improve our presentation skills during consortium meeting rehearsals. I would like to thank Dr. Seth Haines and Dr. Tim Collet for their help with the use of the field data set presented in Chapter 5. I learned a lot from many enlightening discussions that we had during our weekly meetings within the past six months. Also, thank you to the C-Team and

CWP colleagues for their valuable insights into my research projects.

I have been fortunate enough to spend two amazing summers involving in various internship projects at Total Energies. I acknowledge Dr. Vincent Saubestre, Dr. Paul Williamson, Dr. Fuchun Gao, Bertrand Denel, Yen Sun, and the rest of the E&P research and technology team for their support and the opportunity to gain such a valuable industry experience.

None of these achievements would have been possible if the management of Turkish Petroleum Corporation (TPC) did not let me put a hold on my responsibilities at TPC to pursue a PhD degree abroad. I would like to acknowledge the chairman Melih Han Bilgin, the vice president Dr. Mehmet Ferruh Akalin, the head of human resources department Abdulkadir Demir, my previous and current managers at the data processing center Dr. Suat Aktepe and Halil Dalabasmaz for the support that made this journey possible.

I have shared many great memories with my friends Ufuk Durmus and Tugrul Konuk who have always supported me since the beginning of graduate school. I am so grateful for their continued friendship and support. I truly enjoyed our times especially when we had barbecue events in Ufuk's backyard. Tugrul has kindly assisted me with technical issues whenever I got stuck in research. I have also shared many amazing moments with Odette Aragao and Jihyun Yang who have always been so friendly and supportive over the years. Odette has organized numerous unforgettable events that we have enjoyed a lot together and has kindly offered her tasty (birthday) cakes many times. I enjoyed our conversations with Jihyun who never hesitates to show her positive energy and unique sense of humor. I am also grateful to my lifelong friends Seren Sert, Saygin Ileri, and Gozde Eroglu for constantly being there for me within the past fifteen years. A heartfelt thank you to Aysegul Kuzulu who tremendously supported me with a smiling face during my final (and perhaps the most challenging) semester at Mines. Your love and encouragement mean a lot to me.

Finally, I would like to thank all my family especially my dear mother, father, brother, sister-in-law, and niece, Ece, for their unconditional love and support through all these years. There are no words to express how lucky I am to have you in my life.

To my parents...

CHAPTER 1
INTRODUCTION

Exploration seismology deals with physical observations regarding the interior of the Earth's crust to search for economic deposits of, e.g., hydrocarbons or minerals. To serve this purpose, seismic imaging methods commonly are used to investigate variations and discontinuities in the elastic properties of the subsurface (e.g., reflectivity and seismic wave speed). To infer such material properties, one can use seismic waves generated with active (e.g., vibroseis and dynamite) or passive (e.g., earthquakes) sources depending on the type of project. For the latter category, various unconventional subsurface projects, such as hydraulic fracturing, enhanced oil/gas recovery, CO_2 sequestration, and wastewater disposal, may include high-pressure fluid injection activities that can induce stress changes in geologic structures (Maxwell and Urbancic, 2001). As a result of such activities, (micro-) earthquakes or so-called microseismic events (usually $M_w \ll 1$) may occur, which pose potential project risks and thus need to be mitigated for environmental safety purposes (Maxwell, 2014; Weingarten et al., 2015). Monitoring the spatial and temporal distribution of induced seismicity is not only crucial for understanding how the geologic formations respond to fluid injection (e.g., fracture distribution) and/or optimizing the production, but also critical for hazard assessment and risk mitigation (Dziewonski et al., 1981).

In conventional passive monitoring of potential fluid-induced seismicity, a group of seismometers is deployed in boreholes (Warpinski et al., 1998) and/or at the surface (Duncan and Eisner, 2010) to measure microseismic events as a function of ground motion. Whereas borehole monitoring has the advantage of recording events closer to the source points with higher signal-to-noise ratio (S/N), it requires expensive drilling operations. Surface monitoring typically provides better receiver coverage than borehole scenarios. However, surface-recorded microseismic data exhibit lower S/N due to anthropogenic noise generated at the surface and increased distance from the event location. Surface monitoring costs, though, are usually more economic relative to borehole acquisitions.

A key challenge to passive monitoring experiments is the substantial ambiguity with regard to the event location and origin time. The limited control over such event properties can directly affect the success of monitoring programs (Maxwell, 2014). There are several methods developed to estimate event locations. Traditional earthquake detection methods require often subjective picking of first arrivals, which may be a difficult task especially for microseismic data exhibiting low S/N that generally lead to large event location uncertainty. Therefore, Kirchhoff-based and wave-equation seismic migration approaches are now commonly used to infer the location of microseismic events because these methods do not require arrival-time picking and are typically less sensitive to low-quality data (Artman et al., 2010; Kao and Shan, 2004). Time-reverse imaging (TRI) is a migration procedure that effectively maps the recorded microseismic data to a source image that can be used to infer the event location. TRI typically involves propagating microseismic waveforms in reverse time using an adjoint wave equation (McMechan, 1982) and evaluating an imaging condition (Claerbout, 1971) to ideally produce a well-focused event image as a function of space. The success of TRI-based approaches, though, is mainly dependent on the accuracy of the velocity model (Gajewski and Tessmer, 2005). Thus, building reliable velocity models with passive seismic data remains a highly challenging problem particularly for complex geologic settings.

A number of different approaches including traveltime tomography (TTT) and full waveform inversion (FWI) have been developed to tackle the passive velocity model building problem (Grechka and Yaskevich, 2014; Sun et al., 2016); however, in the case of highly noisy data (e.g., S/N < 1) neither method may perform satisfactorily. This is because TTT deals with often subjectively picked arrivals that are contaminated by noise (Rawlinson and Sambridge, 2003) while FWI tends to fit forward-modeled data to noisy observations (Tarantola, 1984), both of which can lead to inaccurate velocity inversion results. Therefore, image-domain tomographic model building methods such as migration velocity analysis

(MVA) may be preferred in such rough scenarios as they are formulated directly based on stacked image metrics (Shen and Symes, 2008; Symes and Carazzone, 1991).

Existing passive seismic imaging and velocity model building techniques are well-developed under the acoustic-media assumption (i.e., the solid rock units are treated like fluids meaning that only compressional (P) waves exist); however, one can also exploit shear (S) waves by accounting for more realistic physical elastic phenomena (Shabelansky et al., 2015; Witten and Shragge, 2017a). An elastic parameterization can allow for more accurate subsurface characterization because S waves contain complementary material property and structural information. Moreover, given that most unconventional projects occur in massive anisotropic shale formations (Vernik and Nur, 1992), accurately handling anisotropy (i.e., directionally dependent wave propagation) in wave propagation likely yields solutions that are physically more plausible compared to simplistic isotropic elasticity assumptions (Li et al., 2016).

Apart from surface microseismic monitoring investigations, there has recently been a growing interest in downhole acquisition using active-source vertical seismic profiling (VSP) technology coupled with distributed acoustic sensing (DAS) optical fibers installed in wells to monitor numerous seismic activities such as CO_2 sequestration and unconventional production (Mateeva et al., 2013; Mestayer et al., 2011). One of the main advantages of DAS VSP data sets is that they can provide complementary information about near-well structures because these data commonly contain higher-frequency information due to shorter travel paths and decreased seismic attenuation relative to conventional surface geophone data. To fully benefit from high-quality active-source DAS VSP data, one can use full-wavefield imaging algorithms such as elastic reverse time migration (RTM) that offer a robust approach for imaging subsurface geologic structure. However, similar to wavefield-based microseismic imaging studies, constructing accurate velocity models is essential to the success of such 3D VSP imaging techniques (Egorov et al., 2018b; Li et al., 2015).

Another similarity between the active-source VSP acquisition and the aforementioned passive surface-monitoring scenarios is that the sources and receivers are not located on the same surface, which opens up the possibility of using similar approaches for imaging and inversion problems. For example, Figure 1.1 depicts two typical acquisition configurations for passive surface monitoring and active-source DAS 3D VSP surveying. By exploiting the principle of reciprocity, one can exchange the source and receiver locations in an active-source DAS 3D VSP scenario to create an acquisition design similar to passive-seismic surface monitoring configurations. Such a reciprocal adjustment can enable one to apply passive-style imaging and inversion methods on active-source DAS 3D VSP data sets. Furthermore, DAS 3D VSP data acquired on land exhibit highly elastic behaviour, which generates complementary information about subsurface properties for reservoir characterization (e.g., methane gas hydrates).

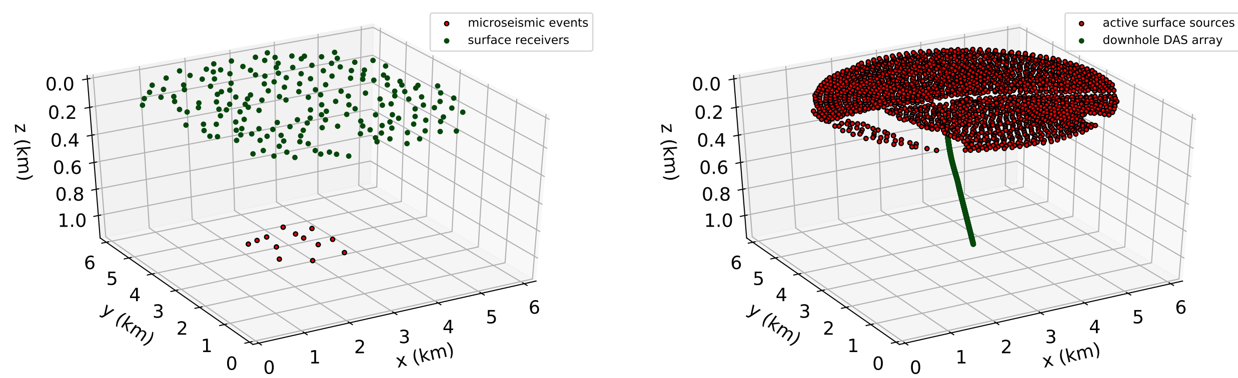

(a) (b)

Figure 1.1 Acquisition scenarios for (a) passive surface monitoring and (b) active-source DAS VSP surveying. Note that one can exploit source-receiver reciprocity to turn the active-source VSP acquisition in (b) into the passive-style surface acquisition in (a).

The main goal of this thesis is to develop an image-domain elastic wavefield tomography framework designed to reconstruct accurate P- and S-wave velocity models that improve the quality of source locations from surface-recorded microseismic and active-source DAS 3D VSP data. To achieve this goal, I first develop a suitable imaging condition that accurately produces elastic source images in isotropic and anisotropic media, as well as exhibit sufficient sensitivity to perturbations in velocity and anisotropy parameters for image-domain tomography algorithms. Using the developed imaging condition, I then propose an image-domain elastic transmission tomography framework that can be used to invert for V_P and V_S models from surface-recorded microseismic or active-source DAS 3D VSP data. I also apply the proposed imaging and inversion methodologies to a DAS 3D VSP data set acquired in the North Slope of Alaska. Finally, I verify the field data inversion results by conducting a well-tie analysis between elastic RTM images and petrophysical data.

1.1 Thesis outline

The thesis is structured into chapters, three of which have been published in peer-reviewed journals, and two of which will be submitted for publication. As the student first author of the following technical chapters, I developed the theory and performed the numerical computations. As the thesis advisor and second author, Dr. Jeffrey Shragge supervised the analytical and numerical findings. Both authors discussed the results and equally contributed to writing the manuscripts and documenting the research work.

In Chapter 2, entitled "PS Energy Imaging Condition for Microseismic Data - Part 1: Theory and Applications in 3D Isotropic Media", I present a novel extended PS energy imaging condition that operates under the TRI concept to effectively image microseismic events. I also study the influence of the V_P and V_S models on the zero-lag and extended source images in 3D isotropic media. This analysis demonstrates that the proposed imaging algorithm shows decent sensitivity to model errors, which may make it a favorable candidate for migration velocity analysis. This chapter was published in *Geophysics*:

- Oren, C. and J. Shragge, 2021, PS energy imaging condition for microseismic data - Part 1: theory and applications in 3D isotropic media: Geophysics, 86, no. 2, KS37–KS48, doi: 10.1190/geo2020-0476.1.

In Chapter 3, entitled "PS Energy Imaging Condition for Microseismic Data - Part 2: Sensitivity Analysis in 3D Anisotropic Media", I present an extension of the PS energy imaging condition to 3D anisotropic media, wherein I analyze the sensitivity of the imaged events to the Thomsen (1986) anisotropy parameters (ϵ, δ, and γ) for three types of TI symmetries: VTI (transversely isotropic with a vertical symmetry axis), HTI (transversely isotropic with a horizontal symmetry axis), and ORT (orthorhombic). This sensitivity analysis shows that the moveout patterns of misfocused energy on the event images are mainly controlled by the distorted Thomsen parameters ϵ and δ, whereas the γ parameters have rather negligible influence on source images. This chapter was presented at a Society of Exploration Geophysicists (SEG) Annual Meeting and was published in *Geophysics*:

- Oren, C. and J. Shragge, 2019, 3D anisotropic elastic time-reverse imaging of surface-recorded microseismic data: Proceedings of the 89^{th} Annual International Meeting, Society of Exploration Geophysicists, 3076-3080.
- Oren, C. and J. Shragge, 2021, PS energy imaging condition for microseismic data - Part 2: sensitivity analysis in 3D anisotropic media: Geophysics, 86, no. 2, KS49–KS62, doi: 10.1190/geo2020-0477.1.

In Chapter 4, entitled "Passive-Seismic Image-Domain Elastic Wavefield Tomography", I propose an image-domain elastic wavefield tomography methodology for multicomponent passive data to invert for V_P and V_S models in isotropic media. I define a multiterm objective function designed to optimize the focusing of auto/crosscorrelation source images, which are formed based on the kinetic energy term of the PS energy imaging condition described in Chapter 1 as the kinetic term tends to provide sufficient information when forming isotropic model gradients. The inversion results suggest that the image misfocusing as well as the location errors are significantly reduced by means of the recovered velocity models. The outcomes of this chapter were presented at an SEG Annual Meeting, at an European Association of Geoscientists and Engineers (EAGE) Annual Meeting, and were published in *Geophysical Journal International*:

- Oren, C. and J. Shragge, 2020, Image-domain elastic wavefield tomography for passive data: Proceedings of the 90^{th} Annual International Meeting, Society of Exploration

Geophysicists, 3669-3673.

- Oren, C. and J. Shragge, 2021, 3D microseismic image-domain elastic velocity inversion: Proceedings of the 82^{nd} Annual International Meeting, European Association of Geoscientists and Engineers.

- Oren, C. and J. Shragge, 2022, Passive-seismic image-domain elastic wavefield tomography: Geophysical Journal International, 228(3), 1512–1529, doi: 10.1093/gji/ggab415.

In Chapter 5, entitled "3D Image-Domain DAS-VSP Elastic Transmission Tomography", I present an implementation of the passive-style inversion framework presented in Chapter 4 on active-source DAS 3D VSP data. To create a suitable inversion setup, I exploit the principle of reciprocity by exchanging the locations of sources and receivers to mimic a passive-seismic surface monitoring scenario, for which the inversion procedure is successfully validated in the previous chapter. I illustrate the efficacy of the tomography method using a DAS 3D VSP data set acquired in the North Slope of Alaska. Using the inverted elastic models in the TRI procedure leads to a reduction of 70% and 92% in the total and vertical RMS mispositioning errors, respectively, as well as a considerable improved image focusing. To further verify the inversion results, I also compute elastic RTM images that better match the existing petrophysical log data in well-ties when using the estimated velocity models. I submitted the field data inversion results presented in this chapter for peer review in *Geophysical Journal International*. Moreover, I co-authored a recently submitted manuscript that investigates the same Alaskan North Slope gas hydrates deposits from acoustic RTM near-well imaging optimized with a V_P model constructed using the proposed image-domain elastic inversion framework:

- Oren, C. and J. Shragge, 2022, 3D image-domain DAS-VSP elastic transmission tomography: Geophysical Journal International (submitted).

- Young, C., J. Shragge, W. Schultz, S. Haines, C. Oren, J. Simmons and T. Collett, 2022, Advanced distributed acoustic sensing vertical seismic profile imaging of an Alaska

North Slope gas hydrate field: Energy and Fuels (submitted).

I will also prepare another manuscript that focuses on the DAS VSP elastic RTM imaging aspect of this chapter. I will submit these outcomes to a peer-reviewed journal:

- Oren, C. and J. Shragge, 2022, 3D full-wavefield multi-mode elastic imaging of DAS VSP data: Geophysical Journal International (to be submitted).

Chapter 6 presents the general conclusions of the thesis along with a discussion of future recommendations on various applications of the presented methods at different scales.

CHAPTER 2

PS ENERGY IMAGING CONDITION FOR MICROSEISMIC DATA - PART 1: THEORY AND APPLICATIONS IN 3D ISOTROPIC MEDIA

A paper published[1] in *Geophysics*

Can Oren[2,3,4], Jeffrey Shragge[4]

Accurately estimating event locations is of significant importance in microseismic investigations because this information greatly contributes to the overall success of hydraulic fracturing monitoring programs. Full-wavefield time-reverse imaging (TRI) using one or more wave-equation imaging conditions offers an effective methodology for locating surface-recorded microseismic events. To be most beneficial in microseismic monitoring programs, though, the TRI procedure requires using accurate subsurface models that account for elastic media effects. We develop a novel microseismic (extended) PS energy imaging condition that explicitly incorporates the stiffness tensor and exhibits heightened sensitivity to isotropic elastic model perturbations compared to existing imaging conditions. Numerical experiments demonstrate the sensitivity of microseismic TRI results to perturbations in P- and S-wave velocity models. Zero-lag and extended microseismic source images computed at selected subsurface locations yields useful information about 3D P- and S-wave velocity model accuracy. Thus, we assert that these image volumes potentially can serve as the input into microseismic elastic velocity model building algorithms.

2.1 Introduction

Subsurface monitoring using microseismic data is an important tool for evaluating subsurface fluid-injection programs (Maxwell, 2014). The monitoring process enables one to

[1]Reprinted with permission of *Geophysics*, Vol. 86, No. 2, (March-April 2021), p. KS37—KS48

[2]Primary researcher and author.

[3]Author for correspondence

[4]Graduate student and Associate Professor, respectively, Center for Wave Phenomena, Colorado School of Mines, Golden, Colorado, USA.

characterize the properties of microseismic events caused by hydraulic fracturing, such as source location, origin time, magnitude, and fracture type and orientation (Dziewonski et al., 1981), thereby allowing for an assessment of fluid-injection operations. Accurate and timely determination of such geophysical observations is important when making engineering decisions ranging from optimizing production to evaluating and/or mitigating potential risks related to induced seismicity.

Over the past few decades, time-reverse imaging (TRI) of surface-recorded microseismic data has received increasing interest (Artman et al., 2010; Gajewski and Tessmer, 2005; McMechan, 1982; Nakata and Beroza, 2016; Witten and Shragge, 2015). A key reason is that full-wavefield methods can produce more accurate simulated wavefield results than ray-based approaches in complex Earth models. Implementing full-wavefield TRI generally involves backpropagating recorded P- and S-wavefield data using an adjoint acoustic or elastic wave equation and applying an imaging condition that stacks wavefield energy over the full wavelet, ideally obtaining a well-focused microseismic event image at the true source coordinates. TRI effectively migrates surface-recorded microseismic events exhibiting low signal-to-noise ratios (S/Ns) (Witten and Shragge, 2017a); however, the success of the TRI methodology primarily depends on the accuracy of the subsurface model (i.e., velocity and anisotropy parameters), which can be challenging to constrain with minimal well control of the subsurface velocity profiles in many field investigations.

An important consideration in successful applications of TRI is the choice of imaging condition used to generate the final event images. The conventional (zero-lag) imaging condition is based on the point-wise correlation between two wavefields (Claerbout, 1971). A conventional pseudo-acoustic imaging condition enables one to generate converted-wave images (i.e., PS) associated with P- and S-wave modes (Rosales et al., 2008; Sava and Fomel, 2005). An extended imaging condition (EIC) is a more general approach that outputs a multidimensional wavefield correlation gather computed at a number of nonzero spatial and/or temporal lags (Rickett and Sava, 2002; Sava and Fomel, 2006).

In passive-style microseismic monitoring applications, wavefield-based migration images carry not only valuable information about the source location and mechanism, but also can reveal velocity model inaccuracy that leads to both event mislocation and misfocusing in zero-lag images and EIC gathers (Witten and Shragge, 2015). In particular, passive EIC gathers resulting from the correlation between temporarily and/or spatially shifted microseismic wavefields can be used to update velocity models based on image misfocusing criteria, as is commonly done in reflection seismology through image-domain tomography (Shen and Symes, 2008; Symes and Carazzone, 1991). Moreover, combining extended wavefield imaging and adjoint-state tomography (Plessix, 2006) leads to an effective passive seismic approach for automatically updating 3D isotropic P- and S-wave velocity models using an elastic (Shabelansky et al., 2015) or a pseudo-acoustic (Witten and Shragge, 2017a,b) formulation.

For microseismic elastic TRI, conventional imaging conditions generally rely on the auto/crosscorrelation between the distinct wave modes (i.e., P and S waves). When using an accurate Earth model for time-reverse propagation, sufficient (surface) wavefield sampling, and microseismic data exhibiting high S/N levels, the resulting correlation images will yield peak amplitudes at the true source location. The quality of these results depends on the accuracy of wave-mode decomposition applied during the backpropagation step, which is straightforward to compute for isotropic Earth models. However, for 3D anisotropic elastic Earth models, wave-mode decomposition in the wavefield domain is significantly more computationally expensive (Dellinger and Etgen, 1990; Yan and Sava, 2011). To mitigate this drawback, Rocha et al. (2019) develop and apply a 3D energy imaging condition for passive elastic TRI that involves the stress, strain, and displacement variables along with the model stiffness tensor components. This imaging condition requires no wave-mode separation and is applicable to any type of medium anisotropy. Moreover, it has a number of additional advantages over its counterparts because it naturally attenuates low-wavenumber artifacts and enhances the correlation between distinct wave modes. Rocha et al. (2019) also introduce the passive EIC gather version of the energy imaging condition.

In this study, we present a novel (extended) PS energy imaging condition that inherits the advantages of the extended energy imaging condition of Rocha et al. (2019), but also exhibits an increased sensitivity to velocity $[\Delta V_P, \Delta V_S]$ model perturbations. This increased sensitivity can be exploited to refine velocity models (e.g., through tomographic updating) to more accurately and consistently image microseismic events in contrast to lower sensitive imaging conditions that can lead to a wavefield focus at incorrect location. To demonstrate this, we investigate the sensitivity of zero-lag images and EIC gathers formed by the energy and the proposed PS energy imaging conditions to $[\Delta V_P, \Delta V_S]$ model perturbations.

We begin by reviewing the theory of elastodynamics on which we base our 3D elastic forward and time-reverse (adjoint) propagation operators. We present the zero-lag conventional and energy imaging conditions as well as their extended-domain generalizations. We then introduce the PS energy imaging condition, and demonstrate through 3D passive imaging experiments involving a complex Earth model that the associated zero-lag images and EIC gathers have greater sensitivity to velocity model perturbations than those formed by the conventional approaches. We also present a methodology to attenuate imaging-related artifacts. The paper concludes with a discussion on the sensitivity results as well as our thoughts on the further use of the PS energy imaging condition in an image-domain adjoint-state inversion framework with a potential extension to anisotropic elastic media applications, a sensitivity analysis of which is presented in Oren and Shragge (2021b).

2.2 Theory

2.2.1 3D elastic wave equation

Derivation of the Cartesian 3D elastic wave equation begins with the equation of conservation of linear momentum given by

$$\rho\, \ddot{u}_i = \partial_j \sigma_{ij}, \quad i, j = 1, 2, 3, \tag{2.1}$$

where $u_i(\mathbf{x}, t)$ represents the displacement field as a function of space $\mathbf{x}$ and time t, $\rho(\mathbf{x})$ is the medium density, $\sigma_{ij}(\mathbf{x}, t)$ is the stress tensor, two superscript dots denote the second-order temporal derivative, and ∂_j is the spatial derivative in the j$^{\text{th}}$ direction. Here and throughout we use summation notation over repeated indices (e.g., $\partial_j \sigma_{ij} = \partial_1 \sigma_{i1} + \partial_2 \sigma_{i2} + \partial_3 \sigma_{i3}$).

Assuming linear elasticity, stress tensor $\sigma_{ij}(\mathbf{x}, t)$ may be related to strain tensor $\varepsilon_{kl}(\mathbf{x}, t)$ according to a constitutive relation

$$\sigma_{ij} = c_{ijkl}\, \varepsilon_{kl} + m_{ij}, \tag{2.2}$$

where $c_{ijkl}(\mathbf{x})$ is the fourth-rank stiffness tensor, and $m_{ij}(\mathbf{x}, t)$ is introduced as the seismic moment tensor source acting as a stress perturbation (Backus and Mulcahy, 1976a,b; Moczo et al., 2014). Accordingly, the equation of motion, rewritten as a function of the strain tensor, is given by

$$\rho\, \ddot{u}_i = \partial_j (c_{ijkl}\, \varepsilon_{kl} + m_{ij}). \tag{2.3}$$

Assuming small displacements ($\|\varepsilon\| \ll 1$), the linear relationship between displacement field $u_i(\mathbf{x}, t)$ and strain tensor $\varepsilon_{kl}(\mathbf{x}, t)$ is given by

$$\varepsilon_{kl} = \frac{1}{2}\big(\partial_k u_l + \partial_l u_k\big). \tag{2.4}$$

Consequently, we rewrite equation 2.3 as a generally anisotropic 3D elastic wave equation using the material symmetry of the Cartesian stiffness tensor

$$\rho\, \ddot{u}_i = \partial_j (c_{ijkl} \partial_k u_l + m_{ij}). \tag{2.5}$$

Numerical elastic wavefield solutions computed via equation 2.5 can be extrapolated forward and backward in time given the spatial distribution of the stiffness tensor $c_{ijkl}(\mathbf{x})$.

2.2.2 Review of extended imaging conditions (EICs)

Elastic TRI involves backpropagating injected surface-recorded multicomponent microseismic data throughout a subsurface Earth model. One can then use correlation-based imaging conditions that exploit the wavefield focusing exhibited by the time-reversed elastic wavefield. To form more clearly focused microseismic source images that have reduced cross-mode contamination (i.e., crosstalk between the unseparated wave modes), one can use Helmholtz decomposition during backpropagation to separate P- and S-wave modes from displacement field $u_i(\mathbf{x}, t)$ (Dellinger and Etgen, 1990; Yan and Sava, 2009),

$$P = \partial_i u_i \tag{2.6}$$

and

$$S_i = \varepsilon_{ijk} \partial_j u_k, \tag{2.7}$$

where $P = P(\mathbf{x}, t)$ and $S_i = S_i(\mathbf{x}, t)$ are the scalar compressional and vector transverse wave modes, respectively. A vector extended imaging condition (EIC) can be formed by correlating P- and S_i-wave modes that are symmetrically shifted in space (Rickett and Sava, 2002; Sava and Vasconcelos, 2011; Witten and Shragge, 2015):

$$I_i^{PS}(\mathbf{x}, \boldsymbol{\lambda}) = \int_0^T P(\mathbf{x} + \boldsymbol{\lambda}, t) S_i(\mathbf{x} - \boldsymbol{\lambda}, t) \, \mathrm{d}t, \tag{2.8}$$

where $\boldsymbol{\lambda} = (\lambda_x, \lambda_y, \lambda_z)$ is the vector space-lag extension, and the integral evaluation in theory starts from the maximum time of the data window ($t = T\,\mathrm{s}$) and progresses in reverse time back to the window origin time ($t = 0\,\mathrm{s}$). Because $S_i(\mathbf{x}, t)$ is a vector containing three components after 3D Helmholtz decomposition, the imaging condition in equation 8 results in three images where the P-wave mode is correlated with each S_i-wave vector component. We note that while extended images also may be described as functions of time shifts (Sava and Fomel, 2006), herein we only examine spatial lags because they are sufficient for constraining the moveout sensitivity to velocity model perturbations. In addition, a 3D space-lag extended image typically ranges over a volume of $(2N_{\lambda_x} + 1, 2N_{\lambda_y} + 1, 2N_{\lambda_z} + 1)$ evaluation points, where N_{λ_i} is the number of positive lag shifts in the i^{th} direction. Finally, the zero-lag imaging condition is a special case of the extended imaging condition where $(N_{\lambda_x}, N_{\lambda_y}, N_{\lambda_z}) = (0, 0, 0)$.

Because a scalar image is preferable for interpretation relative to vector images, one can use the S-wave energy density (E_S) of the decomposed S wavefield (Artman et al., 2010;

Morse and Feshbach, 1953; Rocha et al., 2019; Yang and Zhu, 2019) given by

$$E_S(\mathbf{x}, t) \equiv \mu(S_i S_i)^{1/2}, \tag{2.9}$$

where $\mu(\mathbf{x})$ is the shear-modulus parameter. This definition allows for the specification of a scalar extended PS image (Rocha et al., 2019):

$$I^{PS}(\mathbf{x}, \boldsymbol{\lambda}) = \int_0^T P(\mathbf{x} + \boldsymbol{\lambda}, t) E_S(\mathbf{x} - \boldsymbol{\lambda}, t) \, \mathrm{d}t. \tag{2.10}$$

Although 3D Helmholtz decomposition is relatively straightforward for isotropic media, for anisotropic media applications, one needs to compute computationally expensive solutions of the Christoffel equation (Tsvankin, 2012) to correctly decompose the wavefield into different wave-mode components. To address this issue, Rocha et al. (2019) introduce an extended energy imaging condition that results in a scalar image:

$$\begin{aligned} I^{EN}_{+/-}(\mathbf{x}, \boldsymbol{\lambda}) = \int_0^T & \Big(\rho(\mathbf{x} + \boldsymbol{\lambda}) \, \dot{u}_i(\mathbf{x} + \boldsymbol{\lambda}, t) \, \dot{u}_i(\mathbf{x} - \boldsymbol{\lambda}, t) \\ & \pm c_{ijkl}(\mathbf{x} + \boldsymbol{\lambda}, t) \, \varepsilon_{kl}(\mathbf{x} + \boldsymbol{\lambda}, t) \, \varepsilon_{ij}(\mathbf{x} - \boldsymbol{\lambda}, t) \Big) \mathrm{d}t. \end{aligned} \tag{2.11}$$

Because the contraction of $c_{ijkl}(\mathbf{x} + \boldsymbol{\lambda}, t) \, \varepsilon_{kl}(\mathbf{x} + \boldsymbol{\lambda}, t)$ is identical to $\sigma_{ij}(\mathbf{x} + \boldsymbol{\lambda}, t)$ without the $m_{ij}(\mathbf{x}, t)$ term, equation 2.11 may be rewritten as

$$I^{EN}_{+/-}(\mathbf{x}, \boldsymbol{\lambda}) = \int_0^T \Big(\rho(\mathbf{x} + \boldsymbol{\lambda}) \, \dot{u}_i(\mathbf{x} + \boldsymbol{\lambda}, t) \, \dot{u}_i(\mathbf{x} - \boldsymbol{\lambda}, t) \pm \sigma_{ij}(\mathbf{x} + \boldsymbol{\lambda}, t) \, \varepsilon_{ij}(\mathbf{x} - \boldsymbol{\lambda}, t) \Big) \mathrm{d}t. \tag{2.12}$$

Equation 2.12 corresponds to the Hamiltonian (Lagrangian) operators defined as the summation (difference) between the wavefield kinetic and potential energy terms (Ben-Menahem and Singh, 1981; Rocha et al., 2019). The Hamiltonian operator measures the total wavefield energy and produces images with strong low-wavenumber patterns, whereas the Lagrangian operator measures the differential wavefield energy that suppresses the low-wavenumber artifacts caused by two wavefields sharing the same polarization and propagation direction (Rocha et al., 2019). Therefore, though equation 2.12 involves the autocorrelation of particle velocities $\dot{u}_i(\mathbf{x}, t)$, the extended energy imaging condition with the Lagrangian operator produces images with attenuated low-wavenumber artifacts due to the subtraction operation.

Further advantages include requiring no wave-mode separation during backpropagation prior to the imaging condition evaluation, and handling arbitrary anisotropy due to the explicit introduction of c_{ijkl}. However, as we demonstrate and discuss the possible reasons in the following numerical experiments, the energy imaging condition is somewhat insensitive to model perturbations, which motivates us to explore related alternatives.

2.2.3 Extended PS energy imaging condition

Based on the advantages of the extended energy imaging condition discussed in Rocha et al. (2019), we propose the extended PS energy imaging condition:

$$
\begin{aligned}
I^{\alpha\beta}_{+/-}(\mathbf{x},\boldsymbol{\lambda}) = \int_0^T \Big(& 2\rho(\mathbf{x}+\boldsymbol{\lambda})\, \dot{u}^{\alpha}_i(\mathbf{x}+\boldsymbol{\lambda},t)\, \dot{u}^{\beta}_i(\mathbf{x}-\boldsymbol{\lambda},t) \\
& \pm \sigma^{\alpha}_{ij}(\mathbf{x}+\boldsymbol{\lambda},t)\, \varepsilon^{\beta}_{ij}(\mathbf{x}-\boldsymbol{\lambda},t) \pm \sigma^{\beta}_{ij}(\mathbf{x}+\boldsymbol{\lambda},t)\, \varepsilon^{\alpha}_{ij}(\mathbf{x}-\boldsymbol{\lambda},t)\Big)\mathrm{d}t, \quad \alpha,\beta = P,S,
\end{aligned}
\tag{2.13}
$$

where one injects wave modes separated beforehand in the data domain through preprocessing, rather than the full multicomponent wavefield. While α and β can represent P- or S-wave data in equation 2.13, herein we use different wave modes for α and β (i.e., $\alpha \neq \beta$) in the ensuing numerical experiments. Data-domain separation of individual wave modes is usually a straightforward procedure for surface-recorded microseismic data due to traveltime separation and can be carried out using user-specified or, ideally, automatically chosen hyperbolic time mute functions. We note that this imaging condition is also applicable to conventional PS imaging of seismic reflection data in a converted wave sense; however, herein we are using it exclusively to image the forward-propagated P- and S-wave contributions from individual microseismic events.

Equation 2.13 respectively takes the form of the Hamiltonian (Lagrangian) operator based on the summation (subtraction) operation between the kinetic and potential terms. However, due to the crosscorrelation of now wave-mode separated particle velocities $\dot{u}^{\alpha}_i(\mathbf{x},t)$ and $\dot{u}^{\beta}_i(\mathbf{x},t)$, the Hamiltonian operator no longer produces images with low-wavenumber artifacts; rather, it yields more symmetric and stronger focused events relative to the Lagrangian operator. We validate this inference with realistic examples in the following section. The main advantage of the proposed PS energy imaging condition in equation 2.13 is its greater sensitivity to velocity $[\Delta V_P, \Delta V_S]$ model perturbations than that of the energy imaging condition in equation 2.12. We demonstrate this assertion in the section below.

2.3 Numerical examples

We undertake a number of synthetic numerical experiments using complex models along with realistic acquisition configuration in 3D isotropic elastic media. We begin by investigating the PS energy and energy images exhibiting the estimated microseismic source location for correct velocity models. We then discuss an efficient methodology for attenuating artifacts present in the resulting zero-lag source images. Subsequently, we highlight the different sensitivities of the zero-lag images and EIC gather volumes to velocity model perturbations to examine the benefits of the proposed (extended) PS energy imaging condition.

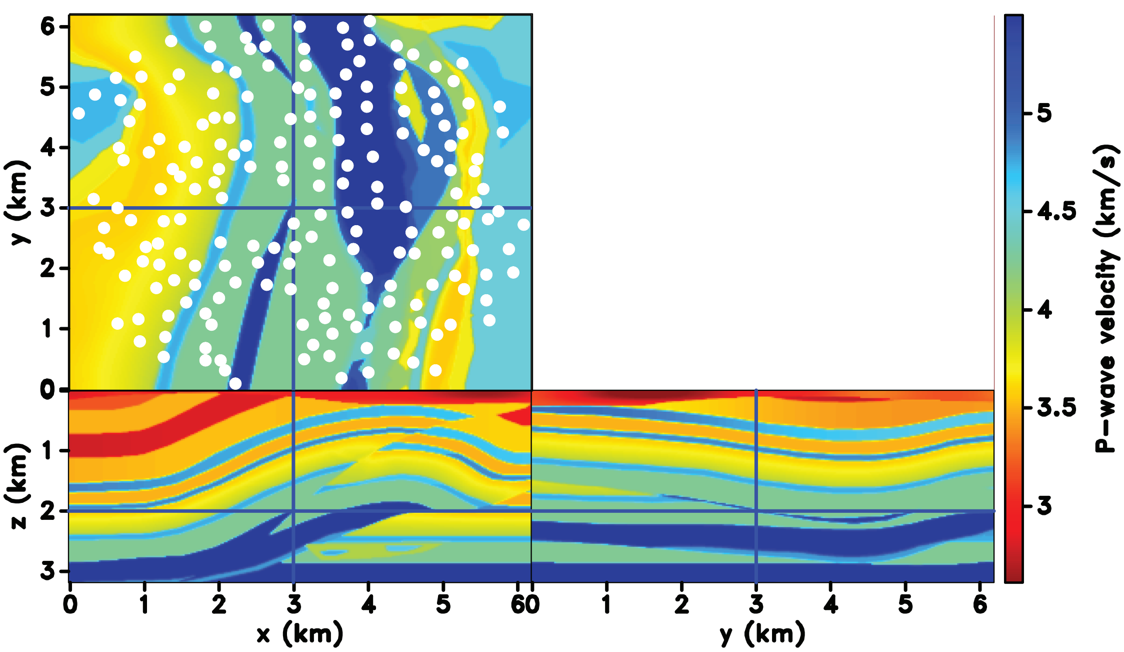

Figure 2.1 P-wave velocity component from the SEG/EAEG 3D Overthrust model. The 3C multicomponent receivers, denoted by the white dots, are deployed at the surface.

2.3.1 3D forward/adjoint elastic propagators

We perform 3D isotropic elastic forward and adjoint (time-reverse) propagation using a stress-displacement formulation on a singly staggered grid (SSG). We use a graphics processing unit (GPU)-based finite-difference time-domain (FDTD) solver with second-order temporal and eighth-order spatial accuracy stencil (Weiss and Shragge, 2013).

Figure 2.1 depicts the SEG/EAEG 3D Overthrust P-wave velocity model (Aminzadeh et al., 1994) along with the multicomponent (3C) receivers (white dots) used in the following numerical tests. This experimental setup offers a realistic test that mimics field-like acquisition conditions. We define an S-wave velocity model by assuming $V_S = V_P/\sqrt{3}$ along with an accompanying density model (not shown) that ranges between $\rho = 2.0 - 3.0\,\mathrm{g/cm}^3$. Both model components share the same structural complexity with the illustrated V_P model. A slightly smoothed version of these models are used during the forward modeling and imaging stages to reduce the scattering effects caused by sharp boundaries.

Our surface receiver array consists of 192 non-uniformly distributed 3C receivers covering an approximately 6×6 km^2 area. The receiver geometry is extracted from a field experiment (Witten and Shragge, 2017b). We simulate a microseismic source located at $[x, y, z] = [3.0, 3.0, 2.0]$ km using a stress-source mechanism (m_{ij} in equation 2.3) oriented at 45$^{\mathrm{o}}$ with respect to the horizontal axis (i.e., non-zero stress components of m_{xx}=-1 and m_{zz}=1) with a 15 Hz Ricker wavelet. We forward model synthetic elastic 3C microseismic data using a 3D computational domain of dimension $[N_x, N_y, N_z] = [248, 248, 128]$, $N_t = 2400$ time steps, temporal and spatial sampling intervals of $\Delta t = 1\,\mathrm{ms}$, and $\Delta x = \Delta y = \Delta z = 0.025\,\mathrm{km}$ with no free-surface boundary condition applied. The simulation time for this 3D isotropic elastic forward modeling takes about 50 s on a single NVIDIA V100 GPU card.

Figure 2.2a and Figure 2.2b shows the forward-modeled vertical u_z and horizontal u_x component data associated with a single microseismic event propagated through the isotropic Earth model shown in Figure 2.1. The PS energy imaging condition uses P- and S-wave modes that require separation on all three components prior to time reversal. Here, we use data-domain hyperbolic mute functions as shown by the blue curves in Figure 2.2 to perform the separation. We note that this represents an additional processing step compared to the energy imaging condition, which uses the full recorded waveforms as input. To improve the S/N of imaged events, we mute waveforms arriving later and earlier than the hyperbolic mute function to better isolate the P- and S-wave modes, respectively.

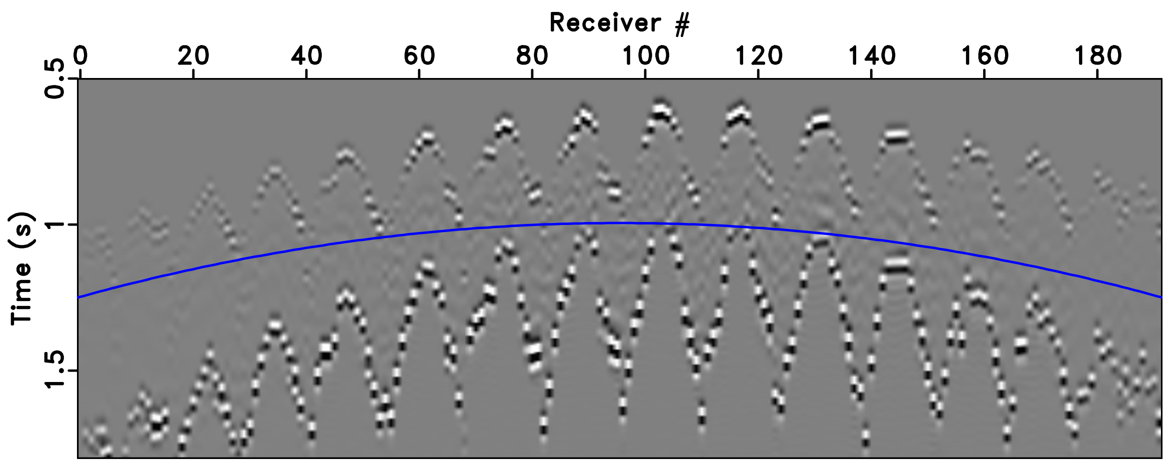

(a)

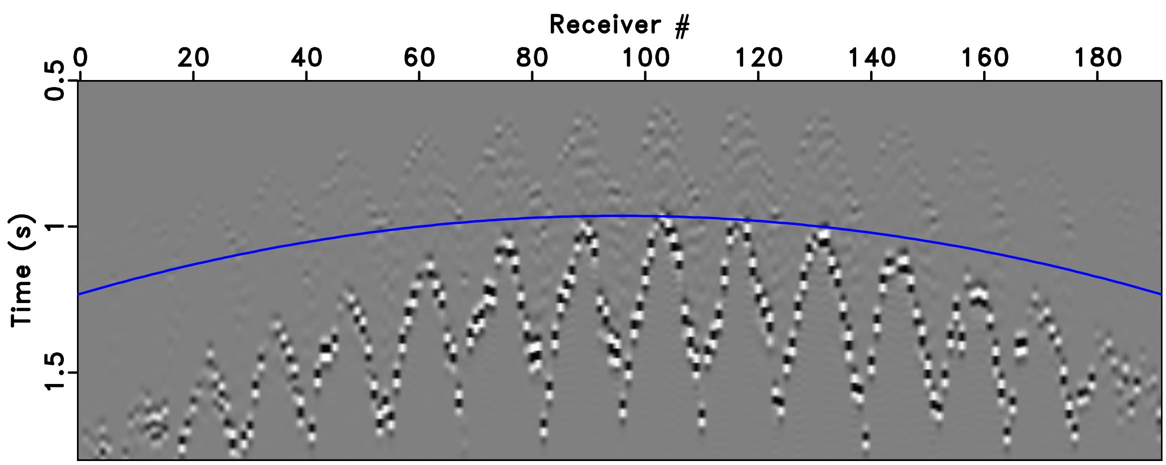

(b)

Figure 2.2 Simulated (a) u_z and (b) u_x components of 3C microseismic data (u_y not shown). P- and S-wave modes are separated in the data domain using the hyperbolic time mute functions like the ones denoted by the blue curves.

2.3.2 Experiment 1: TRI with correct velocity models

Our first numerical experiment examines the TRI results generated by applying the (extended) PS energy and energy imaging conditions. Because we use the correct velocity models in this scenario, we expect the resulting zero-lag and extended image volumes to exhibit energy that is well-focused at the true source location and about zero lag in all dimensions, respectively. We note that this holds even when applied to an event recorded with a sparse geometry and backpropagated through a complex model. Figure 2.3a-Figure 2.3c presents the zero-lag Hamiltonian PS energy, Lagrangian PS energy, and energy images, respectively, constructed using the adjoint propagation operator applied to the elastic data shown in Figure 2.2. Using their correct respective models, all imaging conditions yield strong coherent focusing at the true source location, which is indicated by the intersecting cross-hair lines on the 3D image panels. We also note that the PS energy images exhibit a positive peak amplitude at the correct source location whereas the energy image produces a negative peak amplitude. Compared to its Lagrangian counterpart, the Hamiltonian PS energy image exhibits a more symmetric and relatively stronger focused event. The Hamiltonian and Lagrangian PS energy images arguably show a better resolved event focus than the energy image. However, all images in the upper row of Figure 2.3 exhibit artifacts at shallow depths mainly due to elastic wavefield extrapolation effects of using a sparse and spatially limited surface acquisition aperture and fictitious modes (Rocha et al., 2019; Yan and Sava, 2009).

Figure 2.4 presents the 3D EIC gathers computed with the Hamiltonian PS energy, Lagrangian PS energy, and energy imaging conditions in the same layout as Figure 2.3. All images exhibit energy well-focused at zero lag due to the correct velocity models. Similar to their zero-lag versions, the extended Hamiltonian PS energy image shows a more symmetric focused energy and contains fewer tail artifacts near zero lag compared to its Lagrangian counterpart. The PS energy and energy EIC gathers are respectively evaluated at a single spatial point that is associated with the maximum and minimum peak amplitude (i.e., true source location) of the corresponding zero-lag source image. The minimum peak amplitude in the zero-lag energy images occurs due to the subtraction operation applied to attenuate the low-wavenumber artifacts in the formulation of equation 2.12. Because the peak amplitude point is usually determined automatically for extended imaging evaluation, it is critical to minimize the spurious imaging artifacts on zero-lag images. Selecting an irrelevant spatial point for (extended) imaging condition evaluation could result in incorrect interpretation of microseismic event locations.

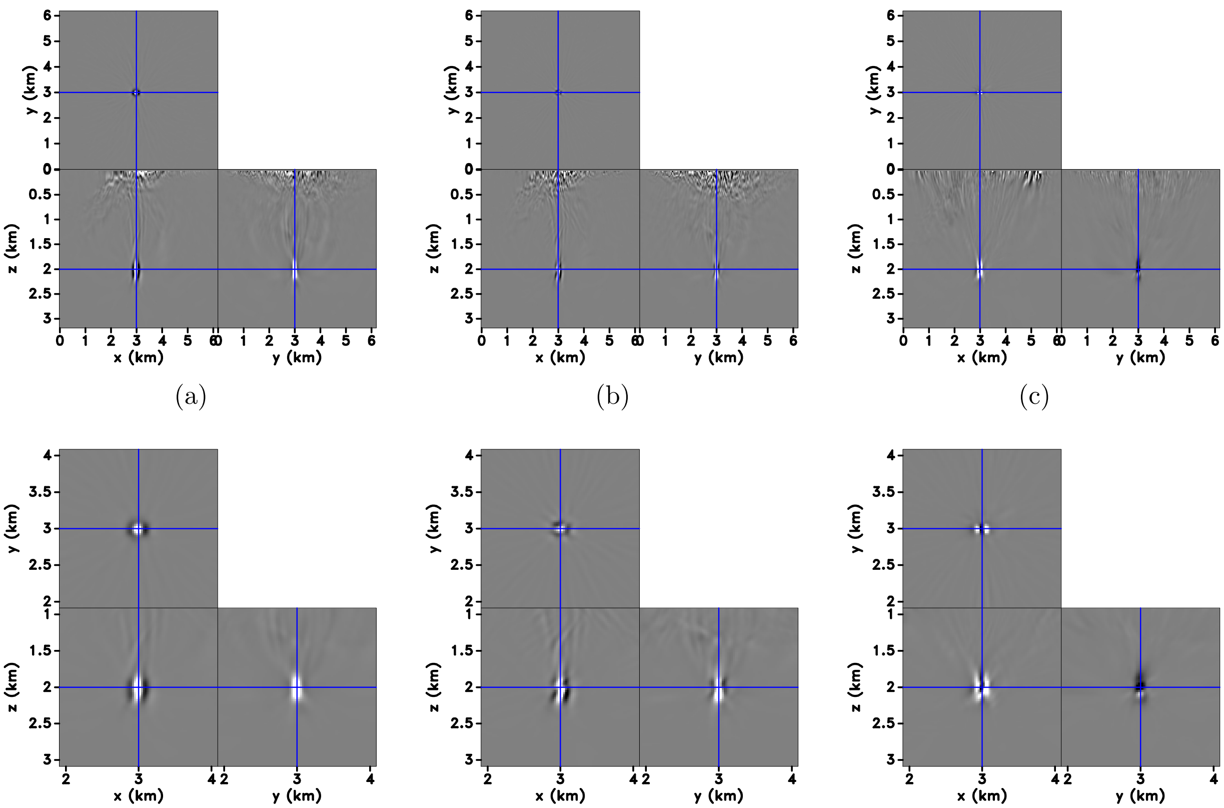

(a) (b) (c)

(d) (e) (f)

Figure 2.3 3D elastic zero-lag images obtained using (a) the Hamiltonian PS energy ($I_+^{\alpha\beta}$ in equation 2.13), (b) Lagrangian PS energy ($I_-^{\alpha\beta}$ in equation 2.13), and (c) energy (I_-^{EN} in equation 2.12) imaging conditions along with their zoomed sections in (d)-(f). The intersecting cross-hair lines indicate the true source location, which corresponds to the maximum image focus for all cases.

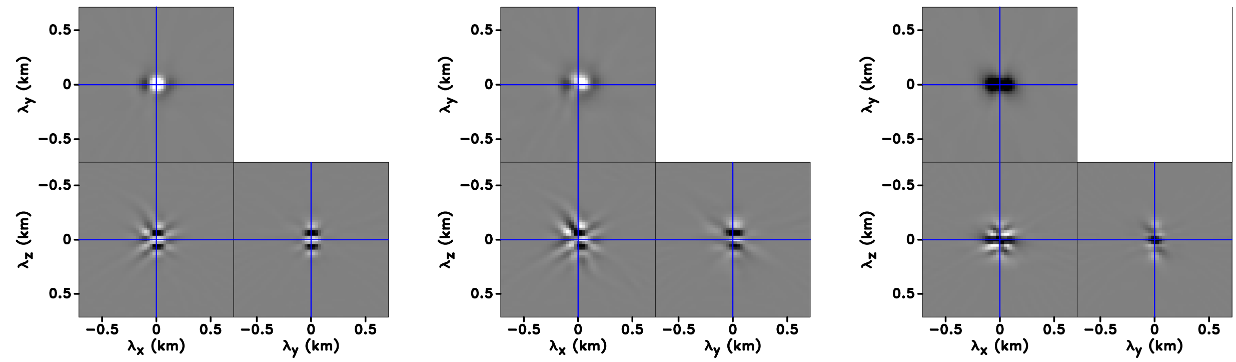

(a) (b) (c)

Figure 2.4 3D space-lag (a) Hamiltonian PS energy ($I_{+}^{\alpha\beta}$ in equation 2.13), (b) Lagrangian PS energy ($I_{-}^{\alpha\beta}$ in equation 2.13), and (c) energy (I_{-}^{EN} in equation 2.12) EIC gathers. We respectively evaluate the PS energy and energy EIC gathers at the maximum and minimum amplitude point, which corresponds to the true source location for both cases. The energy is well-focused at zero lag for all extended images due to the correct velocity models used in the imaging.

2.3.3 Experiment 2: Attenuation of imaging artifacts

In our second experiment, we investigate a method for attenuating artifacts otherwise present in the resulting zero-lag source images. For microseismic field data, wavefield-based imaging conditions involve summation over time (e.g., equation 2.13) because the origin time of the events is unknown. During the backpropagation of receiver wavefields, spurious extrapolation artifacts arise from the sparse and spatially limited surface acquisition aperture as well as from the fictitious P- and S-wave modes generated due to the elastic wavefield injection (Rocha et al., 2019; Yan and Sava, 2008). The correlation of extrapolation-related artifacts with true P- and S-wave modes can degrade the overall image quality and/or increase the uncertainty of source location estimates. Furthermore, such artifacts in zero-lag source images can yield abnormally high amplitudes, which can effectively prevent a successful extended imaging evaluation based on a source location estimate. To mitigate these artifacts, we apply the imaging condition and stack over a time window narrower than the window length of the input microseismic data. Ideally, such a narrower time window closely brackets the source origin time. By using the proposed approach, one can improve image-focusing quality by excluding irrelevant partial image contributions for time steps that are equivalent to the early stages of time-reverse propagation when near-surface spurious correlations dominate the source image.

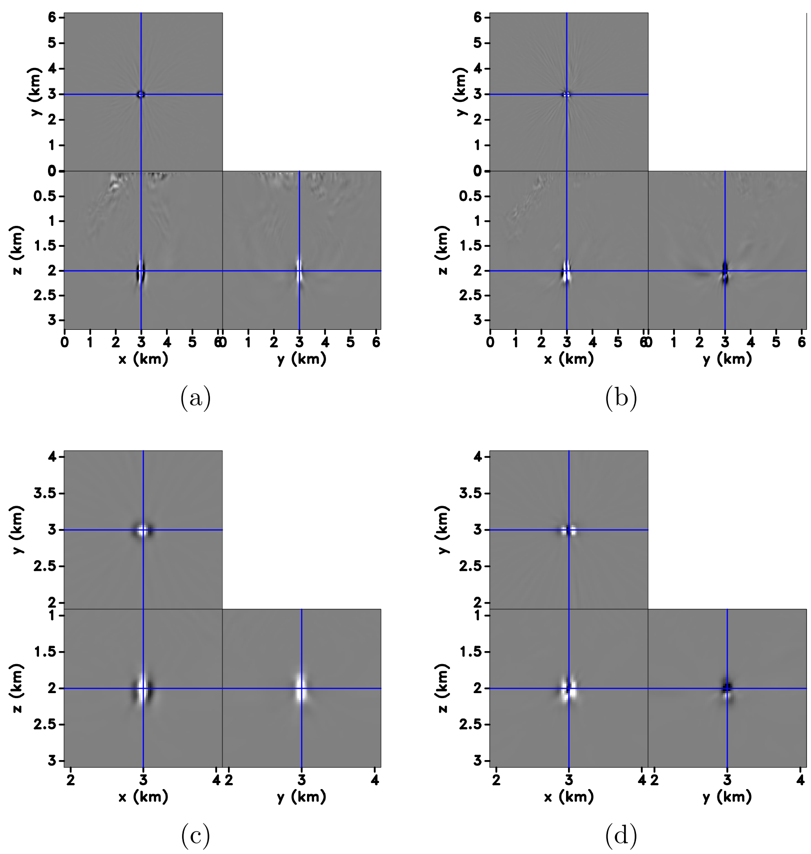

Figure 2.5 3D elastic zero-lag images obtained using the (a) PS energy and (b) energy imaging conditions along with their zoomed sections in (c) and (d). Comparing these results with those in Figure 2.3 illustrates how applying imaging conditions with designated time window $[t_{min}, t_{max}] = [0, 0.15]$ s attenuates the artifacts and enhances image focusing.

Here and hereafter we only compute the PS energy images based on the Hamiltonian operator (i.e., I_+^{PS}) due to its aforementioned advantages over the Lagrangian operator. Figure 2.5 shows the zero-lag PS energy and energy images computed in the time window $[t_{min}, t_{max}] = [0, 0.15]$ s. Note how the partial stacking approach helps attenuate image artifacts in the top 1.5 km depth (Figure 2.3a-Figure 2.3c) relative to those computed for the entire time record $[t_{min}, t_{max}] = [0, 2.4]$ s. We also apply a 40-sample cosine taper function to the partial images that correspond to the edges of the time window, which demonstrably improves the S/N of the stacked image. Because the origin time is known for this synthetic example, only t_{max} is reduced when we design the time window. Currently, we identify the optimal t_{max} through trial and error based on evaluating the quality of the image focusing. Generally, as the user-defined time window broadens, the S/N of the resulting image is reduced. Although residual artifacts still exist, particularly in the PS energy image at the shallow depths (down to 0.5 km depth), the attenuation procedure significantly improves the image S/N, which is clearly observed in the zoomed sections presented in Figure 2.5.

2.3.4 Experiment 3: Sensitivity to velocity model perturbations

The third experiment compares the PS energy and energy imaging condition results when we perform TRI using P- and S-wave velocity model combinations that are globally perturbed by $\pm 10\%$. Figure 2.6 and Figure 2.7 show the zero-lag PS energy and energy images where the top, middle and bottom rows correspond to -10%, 0%, $+10\%$ perturbations in the P-wave velocity, and the left, middle and right columns correspond to -10%, 0%, $+10\%$ perturbations in the S-wave velocity. The PS energy images (Figure 2.6) exhibit a higher degree of misfocusing and moveout patterns that are more observable than those of the energy images (Figure 2.7). Additionally, the depth slices of the PS energy images show a radial "halo" at large offsets from the true microseismic event location. These diagnostic halo effects represent an imprint of model errors and are thus an indicator of velocity model inaccuracy. The energy images, however, do not include these radial patterns and exhibit deteriorated energy focusing on the depth slices. These results suggest increased sensitivity of the PS energy imaging condition to velocity model inaccuracy relative to the energy imaging condition.

The reason for the limited sensitivity of the energy imaging condition is that during the subtraction operation, the kinetic energy term appears to dominate the resulting event focusing that resembles an autocorrelation-like image, which can still lead to a wavefield focus at incorrect source location when using inaccurate velocities. However, due to the individual P- and S-wave modes separated beforehand in the data domain, the proposed PS energy imaging condition yields a crosscorrelation-like image that typically tends to be more sensitive to velocity errors. We again stress that this sensitivity information is important for evaluating and validating model accuracy using an elastic TRI process.

Figure 2.8 and Figure 2.9 depict the corresponding EIC gathers computed with the PS energy and energy imaging conditions, respectively. For plotting purposes, the nine subfigures in these figures follow the same P- and S-wave velocity perturbation layout as presented in Figure 2.6 and Figure 2.7. We evaluate these PS energy and energy EIC gathers at a single spatial point located at the maximum and minimum amplitude of the corresponding zero-lag image, respectively. Similar to the zero-lag TRI results, the extended PS energy images (Figure 2.8) arguably show more characteristic moveout patterns than the extended energy images (Figure 2.9) and are more indicative of the directions of the required P- and S-wave velocity updates. We also note that the PS energy EIC gathers exhibit greater sensitivity with respect to the model perturbations only in the S-wave velocity (Figure 2.8d and Figure 2.8f) compared to only P-wave velocity model perturbations (Figure 2.8b and Figure 2.8h). Thus, the two images may provide complementary information for elastic image-domain tomography updating of model parameters (Shabelansky et al., 2015). The increased sensitivity with respect to S-wave velocity inaccuracy is mainly due to the double-couple stress source mechanism radiating stronger S-wave energy that dominates the resulting source images.

2.4 Discussion

The numerical experiments demonstrate that space-lag EIC gathers computed with the PS energy imaging condition provide valuable insight into P- and S-wave velocity model accuracy. Using accurate Earth models, the energy in the resulting EIC gathers is well-focused at zero lag in the absence of wavefield sampling or illumination issues. Conversely, EIC gathers exhibit poor focusing quality about zero lag when using inaccurate velocity models. As highlighted in Rocha et al. (2019), the energy imaging condition offers a number of advantages over its counterparts (e.g., crosscorrelation imaging condition of the individual wave modes) because it: (1) accounts for the effects of the source radiation pattern during backpropagation due to the elastic formulation; (2) yields a peak amplitude at the source location; and (3) obviates the need for wave-mode decomposition during backpropagation. However, this imaging method exhibits lower sensitivity to model errors, which could decrease its applicability for use in elastic image-domain inversion. The sensitivity (i.e., smeared energy and/or focus shifted away from zero lag on extended images) with respect to velocity inaccuracy can be effectively used for determining relative P- and S-wave velocity updates to improve the focusing of the extended images. The proposed PS energy imaging condition inherits all the aforementioned advantages of the energy imaging condition. Additionally, it produces images that exhibit improved sensitivity to P- and S-wave velocity model perturbations. Therefore, PS energy EIC gathers are more likely to be useful for elastic migration velocity analysis of microseismic data to update P- and S-wave velocity models (Witten and Shragge, 2017a,b).

In practice, one can efficiently calculate the traveltimes of direct P- and S-wave modes by tracing rays from a selected point in the hydraulic stimulated volume to each surface receiver. The selected point is ideally expected to represent the approximate event location. Based on this traveltime information, one can obtain mute functions that possibly result in a more accurate separation of the individual wave modes. Using such an approach, one could better eliminate the undesirable portion of the data (i.e., converted waves and/or noise), and thereby enhance image quality. The further benefits of the proposed approach involve determining time windows that closely brackets the approximate source origin time as discussed in Experiment 2, which has the potential to preclude the possible failures caused by a trial and error analysis.

It is also worth noting that the wave-mode separation procedure becomes more challenging in the presence of extremely low S/N and/or overlapping P- and S-wave arrivals recorded from multiple events initiated at nearby event locations and times. PS energy images constructed with imperfectly separated P and S wavefields can still produce reasonably focused event images, but this inaccurate data separation would reduce the resulting S/N. Thus, the method does not completely fail, and appears to hold no strict requirements in data separation process. Additionally, in image-domain tomography algorithms, the proposed imaging condition can be exploited by selecting microseismic events that are suitable for separation and/or exhibit relatively high S/N as demonstrated in Witten and Shragge (2017b).

The primary drawback of the proposed method is that its computational cost is nearly $1.85\times$ more expensive than that of the energy imaging condition due to the elastic backpropagation of the separated wave modes. However, both imaging methods can be implemented in a reasonable time frame using GPU computing resources. Using the previously introduced experimental setup in the TRI process, computing both 3D zero-lag and extended images related to a single microseismic event takes about 70 s and 130 s when using the energy and PS energy imaging conditions, respectively, on a single NVIDIA V100 GPU card. The extended images presented in the numerical examples include $(2N_{\lambda_x}+1, 2N_{\lambda_y}+1, 2N_{\lambda_z}+1) = (57, 57, 57)$ samples, a number of which is another factor affecting the overall run time. However, because the extended images are constructed at a single spatial point (i.e., estimated source location), their computational cost is generally insignificant. Moreover, the general computational expense can be further reduced using a domain-decomposition strategy across multiple GPU devices.

Finally, the proposed extended PS energy imaging condition can be conveniently formulated for any type of (visco)elastic medium anisotropy because the formulation handles arbitrary anisotropy due to the explicit introduction of stiffness tensor c_{ijkl} in equation 2.11. This straightforward extension can be implemented by incorporating additional required anisotropy parameters and stiffness coefficients into the adjoint propagation operator. We illustrate this supposition by conducting a detailed sensitivity analysis of the proposed imaging method for 3D anisotropic media (e.g., transversely isotropic with a vertical and horizontal symmetry axes as well as orthorhombic) in Oren and Shragge (2021b).

2.5 Conclusions

We introduce a novel (extended) PS energy imaging condition that is applicable for locating microseismic events in 3D elastic media. By conducting realistic synthetic numerical experiments of three different cases, we demonstrate that the proposed PS energy imaging condition exhibits improved sensitivity to the P- and S-wave velocity model perturbations. These benefits come at the marginal cost of performing a straightforward data-domain separation of P- and S-wave modes prior to time-reverse propagation. The PS energy imaging condition represents a theoretical extension of the energy imaging condition and thus inherits all of its useful characteristics. The improved sensitivity of extended PS energy images likely will be useful in a future microseismic migration velocity analysis framework aimed at updating elastic velocity models based on optimizing the focusing of the EIC gathers.

2.6 Acknowledgments

We thank associate editor Y. E. Li and two reviewers for their comments, which improved the quality of the manuscript. We acknowledge the Center for Wave Phenomena (CWP) consortium sponsors for their financial support. The reproducible numerical examples in this paper were generated using the Madagascar software package using the Wendian HPC systems made available through the Colorado School of Mines.

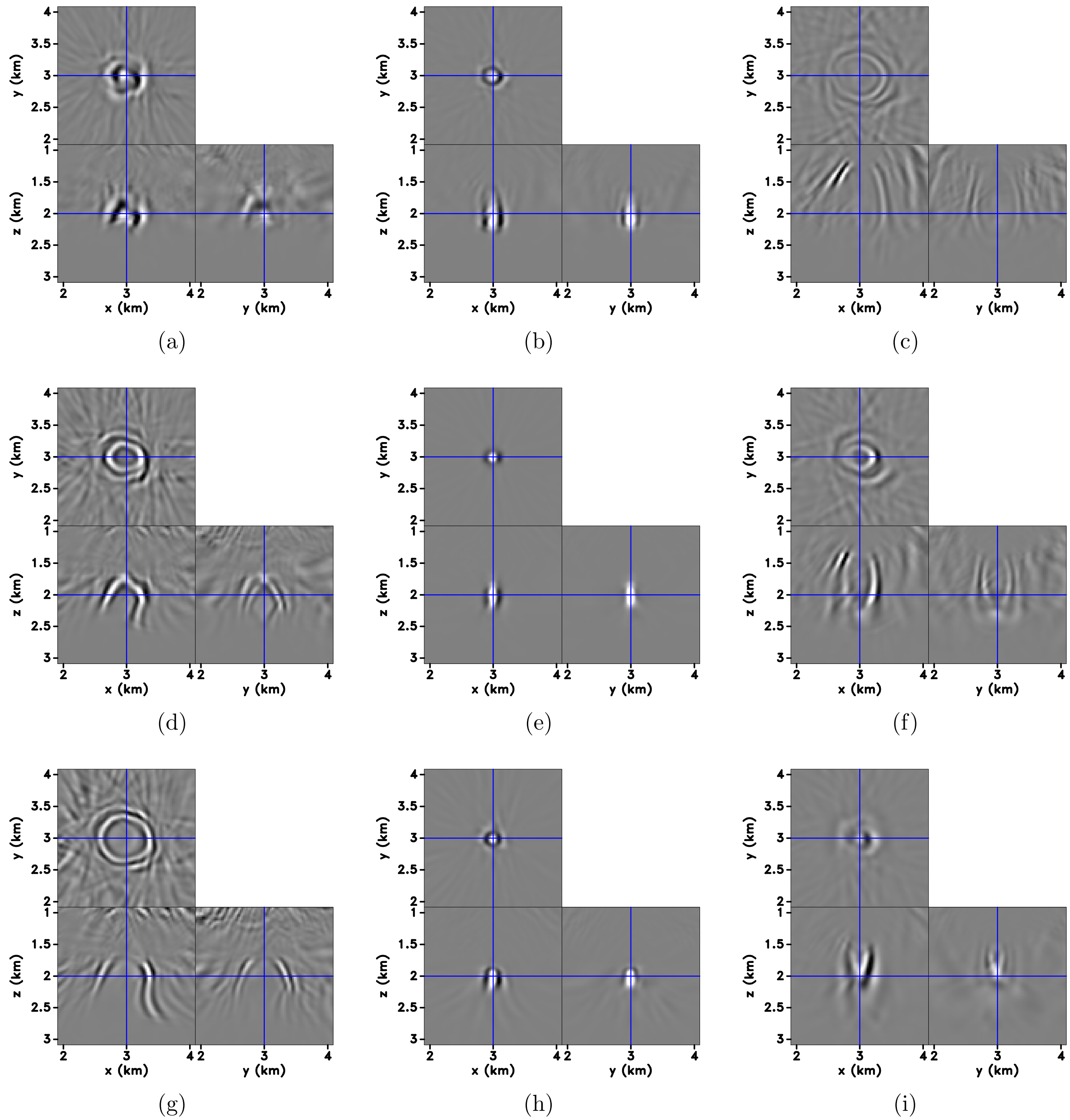

Figure 2.6 Zero-lag PS energy images with incorrect velocities. Top, middle and bottom rows correspond to -10%, 0%, +10% perturbations in the P-wave velocity. Left, middle and right columns correspond to -10%, 0%, +10% perturbations in the S-wave velocity. Note the unfocused events with respect to the focused energy in (e), which is obtained with the correct P- and S-wave velocity models.

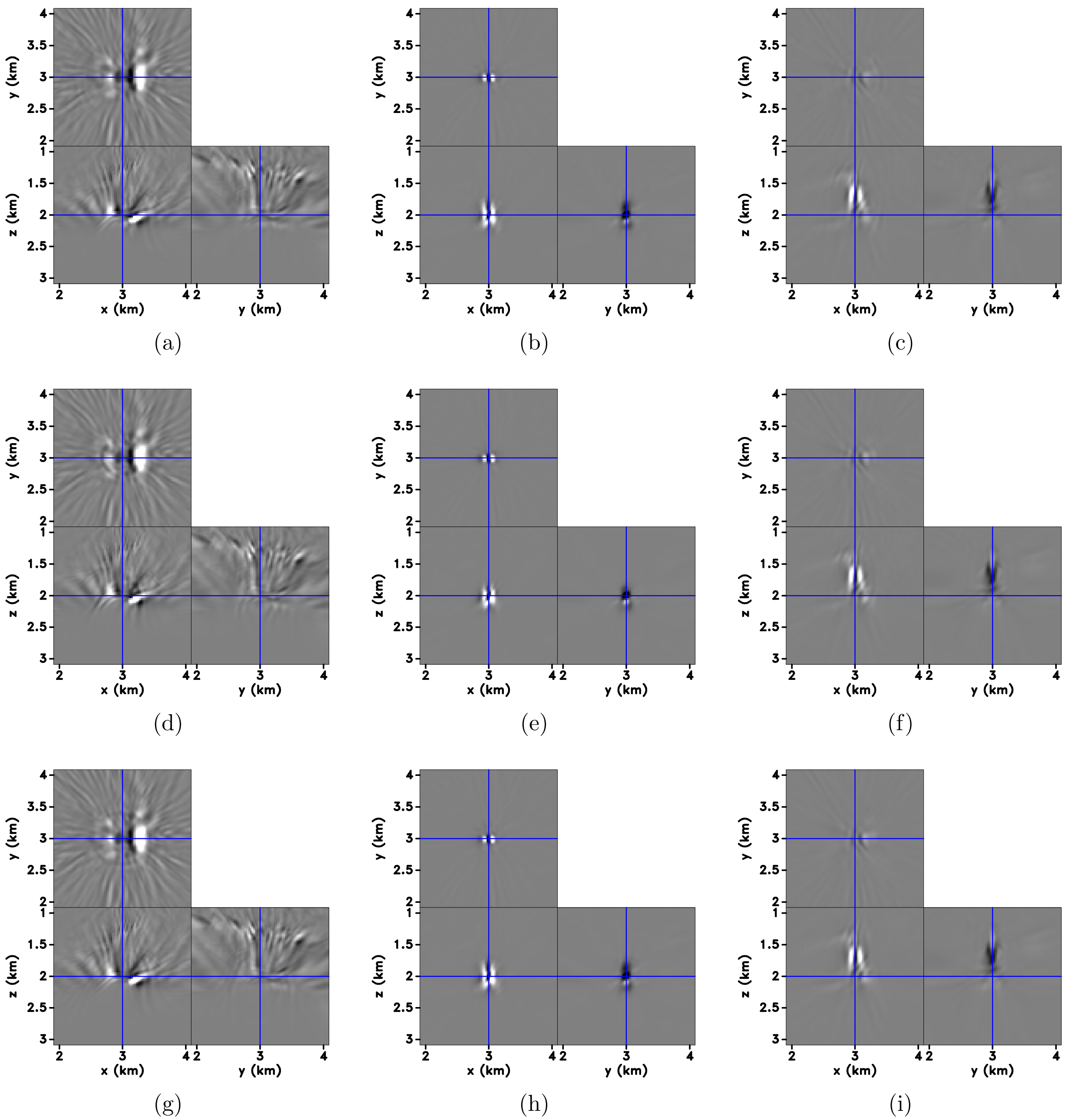

Figure 2.7 Zero-lag energy images with incorrect velocities. Top, middle and bottom rows correspond to -10%, 0%, +10% perturbations in the P-wave velocity. Left, middle and right columns correspond to -10%, 0%, +10% perturbations in the S-wave velocity. Note the unfocused events with respect to the focused energy in (e), which is obtained with the correct P- and S-wave velocity models.

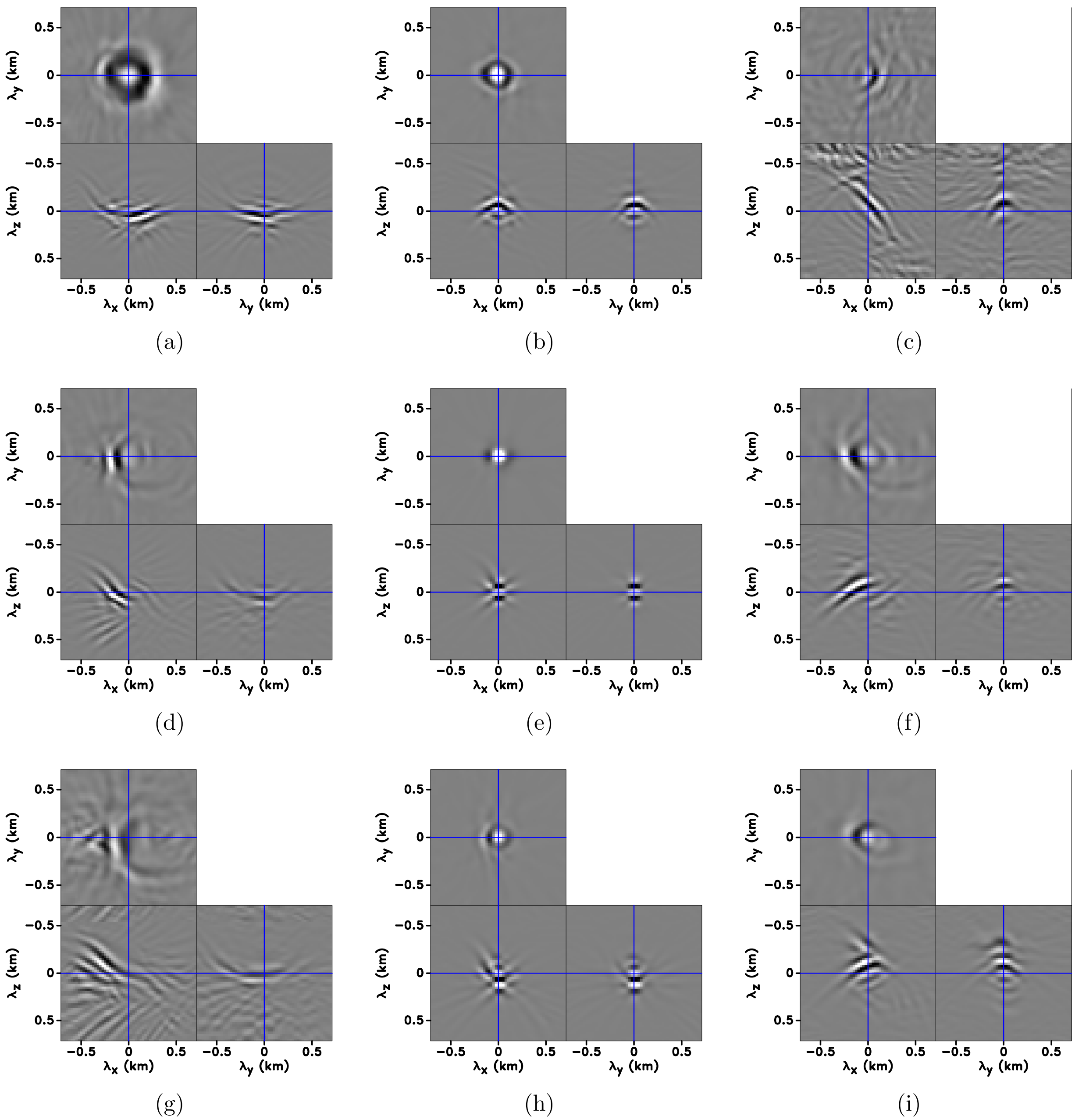

Figure 2.8 PS energy EIC gathers corresponding to the subpanel image layout used in Figure 2.6. PS energy EIC gathers are evaluated at the maximum amplitude point of the corresponding zero-lag PS energy images in Figure 2.6.

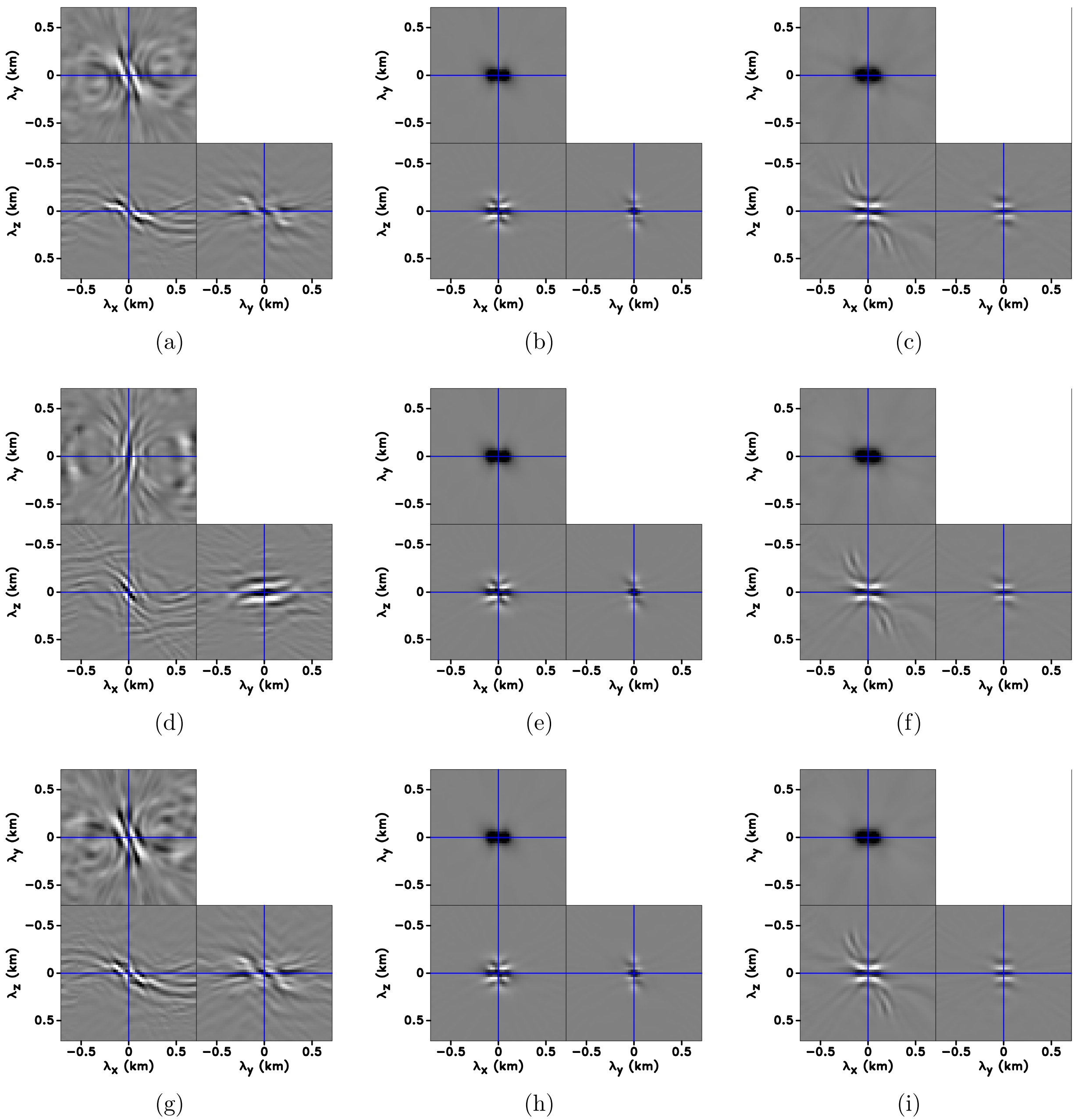

Figure 2.9 Energy EIC gathers corresponding to the subpanel image layout used in Figure 2.7. Energy EIC gathers are evaluated at the minimum amplitude point of the related zero-lag energy images in Figure 2.7.

CHAPTER 3

PS ENERGY IMAGING CONDITION FOR MICROSEISMIC DATA - PART 2: SENSITIVITY ANALYSIS IN 3D ANISOTROPIC MEDIA

A paper published[1] in *Geophysics*

Can Oren[2,3,4], Jeffrey Shragge[4]

In microseismic monitoring, obtaining reliable information about the event properties, such as the location, origin time, and moment tensor components, is critical for evaluating the success of the fluid injection programs. Elastic wavefield-based migration approaches can robustly image microseismic sources by extrapolating data through an earth model and evaluating an imaging condition. The success of these imaging methods, though, primarily depends on the elastic model accuracy. The previously developed extended PS energy imaging condition can provide valuable information about the accuracy of the elastic model parameters including vertical P- and S-wave velocities as well as anisotropy coefficients. Using the SEAM Barrett Unconventional model, we assess the influence of errors in the anisotropy parameters by conducting a sensitivity analysis in three types of 3D models: VTI (transversely isotropic with a vertical symmetry axis), HTI (transversely isotropic with a horizontal symmetry axis), and ORT (orthorhombic) media. Our analysis on zero-lag and extended PS energy images computed with perturbed anisotropy models shows that event images exhibit different moveout patterns of misfocused energy with respect to the distorted Thomsen parameters ϵ and δ; however, for this model, the γ parameters have almost no influence on images regardless of the applied perturbations, which are reflected in minimal traveltime differences in the data. The dependence of microseismic source images on these

---

[1]Reprinted with permission of *Geophysics*, Vol. 86, No. 2, (March-April 2021), p. KS49—KS62
[2]Primary researcher and author.
[3]Author for correspondence
[4]Graduate student and Associate Professor, respectively, Center for Wave Phenomena, Colorado School of Mines, Golden, Colorado, USA.

parameters provides essential insights into anisotropic model accuracy, and suggests that misfocused energy on extended image gathers may be used as a criterion for updating earth models through anisotropic elastic image-domain inversion.

3.1 Introduction

In most hydraulic fracturing applications, the difficult task of building an earth model sufficiently accurate for determining microseismic event locations is made further challenging when unconventional reservoirs are situated in massive shale formations known to exhibit moderate-to-strong anisotropy (Vernik and Liu, 1997; Vernik and Nur, 1992). For this reason, incorporating an anisotropic parameterization is an important consideration when designing a joint model-building and event-location inversion framework (Maxwell et al., 2010). While a number of investigations have examined anisotropic model building using borehole microseismic data (Grechka et al., 2011; Grechka and Yaskevich, 2014; Jarillo Michel and Tsvankin, 2017), few studies using surface-based microseismic monitoring methods exist in the literature. The closest investigation may be Witten and Shragge (2017b), which presents a case study from Marcellus Shale that simultaneously updates isotropic P- and S-wave velocity (V_P and V_S) models along with event locations using a pseudo-acoustic image-domain inversion framework.

Time-reverse imaging (TRI) of microseismic data recorded at surface or borehole receivers have gained interest due to its accuracy in handling wave propagation in complex subsurface structures by using the full waveform information (Artman et al., 2010; Gajewski and Tessmer, 2005; Oren and Shragge, 2019; Rocha et al., 2019; Saenger, 2011; Witten and Shragge, 2015; Yang and Zhu, 2019). Implementing TRI in elastic media typically involves backpropagating P- and S-wave arrivals using an adjoint elastic wave equation and applying some form of imaging condition that effectively stacks over the full microseismic waveform to generate an ideally well-focused microseismic source image. When using sufficiently accurate models, the maximum amplitude of the imaged event corresponds to the true source location; otherwise, inaccurate models can lead to image misfocusing as well as severe location errors inferred from displaced peak image amplitudes. Therefore, using accurate (anisotropic) models in elastic TRI is essential for successful event location applications.

To investigate the effects of anisotropy in the 3D image domain, one must use a 3D imaging condition that is sensitive to variations in the associated anisotropy parameters. The sensitivity information is essential because imaging conditions exhibiting limited sensitivity can produce a wavefield focus at incorrect coordinates, which could lead to misleading event location estimates as well as suboptimal interpretations and engineering decisions derived therefrom. Moreover, image sensitivity can be utilized to refine anisotropic models through image-domain tomography methods to achieve improved accuracy of imaged events and more accurate location estimates. For example, gathers generated from an extended imaging condition (EIC) are known to be sensitive to the presence and magnitude of anisotropy even when using accurate isotropic background P-wave velocities in the acoustic imaging procedure (Li et al., 2016; Sava and Alkhalifah, 2015). For reflection imaging, Sava and Alkhalifah (2015) demonstrate that ignoring anisotropy during acoustic wavefield extrapolation yields different image-domain signatures than those due to purely inaccurate velocity model effects. Similarly, Li et al. (2016) examine the influence of errors in the Thomsen (1986) anisotropy parameters η (Alkhalifah and Tsvankin, 1995) and δ on both acoustic reverse time migration (RTM) extended and angle gathers for VTI (transversely isotropic with a vertical symmetry axis) media and show that errors in η models have a dip-dependent signature while laterally varying δ model errors lead to EIC gather defocusing.

For the elastic TRI of surface-recorded multicomponent microseismic data, Rocha et al. (2019) introduce the extended energy imaging condition, perform a number of sensitivity tests to P- and S-wave velocities, and show its advantages over auto/crosscorrelation imaging conditions. Oren and Shragge (2019) develop the extended PS energy imaging condition that inherits all of the advantages of the energy imaging condition while additionally exhibiting enhanced sensitivity to velocity model perturbations, which makes this imaging condition a candidate for image-domain model building. Oren and Shragge (2021a) present a thorough description of the PS energy imaging condition and demonstrate its improved sensitivity to velocity model perturbations in 3D isotropic media. However, none of these studies investigate anisotropic scenarios.

In this study, we extend the work of Oren and Shragge (2021a) to demonstrate that the PS energy imaging condition handles arbitrary transversely isotropic (TI) media and exhibits increased sensitivity to perturbations in anisotropy parameters compared to the energy imaging condition. We begin by summarizing the 3D anisotropic elastic wave equation along with the extended imaging conditions used in the TRI step. Next, we briefly present the key characteristics of the 3D SEAM Barrett Unconventional model (Regone et al., 2017) used in our sensitivity analysis. We then show how these imaging conditions can handle various TI symmetries, including VTI, HTI (transversely isotropic with a horizontal symmetry axis), and ORT (orthorhombic) when imaging microseismic events with accurate models. We present a detailed analysis to demonstrate the sensitivity of the image volumes to perturbations in anisotropy parameters. We also discuss the error in location estimates inferred from imaged events for different TI symmetries to highlight the potential consequences of ignoring anisotropy during elastic TRI. By doing so, we show that PS energy images exhibit increased sensitivity to anisotropy parameter variations compared to energy images, an observation with important implications for multiparameter image-domain model building. Finally, we discuss the prospectus of undertaking such an analysis in terms of a microseismic image-domain anisotropic tomography considering the sensitivity of each parameter.

3.2 Theory

This section presents the elastic wave equations used in TRI, as well as various passive imaging methods including the extended energy (Rocha et al., 2019) and PS energy (Oren and Shragge, 2021a) imaging conditions applied for extracting the event location using multicomponent microseismic data. Readers unfamiliar with the TRI process or who seek more detailed information are also referred to existing literature (Artman et al., 2010; Gajewski and Tessmer, 2005; Nakata and Beroza, 2016; Oren and Shragge, 2021a; Witten and Shragge, 2015).

3.3 3D elastic wave equation

Assuming linear elasticity, we consider the 3D anisotropic elastic wave equation

$$\rho\, \ddot{u}_i = \partial_j (c_{ijkl} \partial_k u_l + m_{ij}), \tag{3.1}$$

where $u_i(\mathbf{x}, t)$ is the displacement field as a function of space $\mathbf{x}$ and time t, $\rho(\mathbf{x})$ is the medium density, $c_{ijkl}(\mathbf{x})$ is the fourth-rank stiffness tensor, and $m_{ij}(\mathbf{x}, t)$ is the seismic moment tensor source acting as a stress perturbation (Backus and Mulcahy, 1976a,b; Moczo et al., 2014). The two superscript dots on $\ddot{u}_i(\mathbf{x}, t)$ indicate second-order time differentiation, and ∂_j is the spatial derivative in the j^{th} direction. We assume Cartesian geometry in which the $x-$, $y-$, and $z-$axes are respectively expressed by indices $i = 1, 2, 3$, and we use summation notation for repeated indices.

A displacement field $u_i(\mathbf{x}, t)$ computed via numerical implementation of equation 3.1 can be extrapolated forward and backward in time between the window start and end times, $t = [0, T]\,\mathrm{s}$, given the spatial distribution of the stiffness tensor $c_{ijkl}(\mathbf{x})$. In this paper, we represent the earth model in terms of Thomsen (1986) parameters. In the ensuing numerical experiments, we use a moment-tensor source m_{ij} to create realistic source configurations.

Equation 3.1 is derived from two key relationships. The first is a linear constitutive relation describing the elastic material properties through the stiffness tensor $c_{ijkl}(\mathbf{x})$

$$\sigma_{ij} = c_{ijkl}\, \varepsilon_{kl} + m_{ij}, \tag{3.2}$$

which relates the strain tensor $\varepsilon_{kl}(\mathbf{x}, t)$ to the Cauchy stress tensor $\sigma_{ij}(\mathbf{x}, t)$. The second is infinitesimal displacements ($\|\varepsilon\| \ll 1$), which leads to a linear relationship between displacement field $u_i(\mathbf{x}, t)$ and strain tensor $\varepsilon_{kl}(\mathbf{x}, t)$

$$\varepsilon_{kl} = \frac{1}{2}\big(\partial_k u_l + \partial_l u_k\big). \tag{3.3}$$

3.3.1 Extended energy imaging condition

To address a number of issues noted by numerous authors about the conventional cross-correlation imaging condition (e.g., wave-mode decomposition, generation of nodal planes at estimated source locations), Rocha et al. (2019) introduce two extended energy imaging conditions that result in scalar images:

$$I^{EN}_{+/-}(\mathbf{x},\boldsymbol{\lambda}) = \int_{t_{min}}^{t_{max}} \Big(\rho(\mathbf{x}+\boldsymbol{\lambda})\,\dot{u}_i(\mathbf{x}+\boldsymbol{\lambda},t)\,\dot{u}_i(\mathbf{x}-\boldsymbol{\lambda},t) \pm \sigma_{ij}(\mathbf{x}+\boldsymbol{\lambda},t)\,\varepsilon_{ij}(\mathbf{x}-\boldsymbol{\lambda},t)\Big)\mathrm{d}t, \tag{3.4}$$

where $\boldsymbol{\lambda} = (\lambda_x, \lambda_y, \lambda_z)$ is the vector space-lag extension. A zero-lag imaging condition is thus a special case of the extended imaging condition where images are only computed at $\boldsymbol{\lambda} = (0,0,0)\,\mathrm{m}$. A 3D space-lag extended image generally ranges over a volume of $(2N_{\lambda_x}+1, 2N_{\lambda_y}+1, 2N_{\lambda_z}+1)$ spatial points, where N_{λ_i} is the number of positive lag shifts in the i^{th} direction. As described by Oren and Shragge (2021a), one may mitigate further imaging artifacts (i.e., spurious wave-mode correlations) that contaminate zero-lag images by applying an imaging condition within a time window $t = [t_{min}, t_{max}]$ that brackets the true event initiation time, which is narrower than the original window length of the input microseismic data. Therefore, a practical implementation of the integral evaluation in equation 3.4 starts from a designated maximum time ($t_{max} < T\,\mathrm{s}$) and progresses backward in time to a designated minimum time ($t_{min} > 0\,\mathrm{s}$).

Energy image I^{EN}_{+} corresponds to the temporal integration of the total energy of the wavefield kinetic and potential energy terms (Hamiltonian operator), whereas I^{EN}_{-} is related to a differential energy measure (Lagrangian operator) (Ben-Menahem and Singh, 1981). The subtraction operation between the kinetic and potential terms enables one to attenuate low-wavenumber artifacts in the resulting energy images (Rocha et al., 2019).

3.3.2 Extended PS energy imaging condition

Due to the minimal sensitivity of the extended energy imaging condition to the model errors, Oren and Shragge (2021a) propose two related extended PS energy imaging conditions:

$$
\begin{aligned}
I^{\alpha\beta}_{+/-}(\mathbf{x},\boldsymbol{\lambda}) = \int_{t_{min}}^{t_{max}} \Big(& 2\rho(\mathbf{x}+\boldsymbol{\lambda})\, \dot{u}^{\alpha}_{i}(\mathbf{x}+\boldsymbol{\lambda},t)\, \dot{u}^{\beta}_{i}(\mathbf{x}-\boldsymbol{\lambda},t) \\
& \pm \sigma^{\alpha}_{ij}(\mathbf{x}+\boldsymbol{\lambda},t)\, \varepsilon^{\beta}_{ij}(\mathbf{x}-\boldsymbol{\lambda},t) \pm \sigma^{\beta}_{ij}(\mathbf{x}+\boldsymbol{\lambda},t)\, \varepsilon^{\alpha}_{ij}(\mathbf{x}-\boldsymbol{\lambda},t)\Big)\mathrm{d}t, \quad \alpha,\beta = P,S,
\end{aligned}
\tag{3.5}
$$

where one injects the direct P- and S-wave arrivals separated beforehand through a straightforward hyperbolic time muting in the data domain. This procedure is followed by the individual backpropagation of separated P- and S-wave modes using the elastic wave equation (equation 3.1). Although α and β generally respectively represent P- and/or S-wave modes, we use different wave modes for α and β (i.e., $\alpha \neq \beta$) to form PS energy images for the remainder of the paper.

In the following numerical examples, we compute Hamiltonian PS energy images $I^{\alpha\beta}_{+}$ that exhibit enhanced focusing relative to its Lagrangian counterpart $I^{\alpha\beta}_{-}$ (Oren and Shragge, 2021a). For (extended) energy images, though, we use the Lagrangian energy images I^{EN}_{-} that are free of low-wavenumber artifacts and generate superior event image focusing relative to the Hamiltonian formulation (Rocha et al., 2019).

3.4 The Barrett unconventional model

The Barrett unconventional model was designed to represent shale reservoirs in a North America midcontinent basin during SEG Advanced Modeling (SEAM) Phase II (Regone et al., 2017). The Barrett model represents a land seismic scenario constructed based on the geology of the Arkoma Basin, which covers a number of shale plays and expands from eastern Arkansas to western Oklahoma (Houseknecht et al., 2014). The reservoir region of the model is located approximately between 2.5 - 3.3 km in depth and consists of two shale layers detached by thick chalk units. The geology of the upper and lower shale reservoir layers represent the Woodford and Eagle Ford plays in Oklahoma and Texas, respectively, while the thick chalk layers in between these shale units are characteristic of the Austin Chalk and Buda Limestone formations (Regone et al., 2017). The model also includes complex geologic features such as meandering stream channels and faults. Our parameterization of TI symmetries uses Thomsen (1986) notation $[V_{P0}, V_{S0}, \epsilon, \delta, \gamma]$. Figure 3.1a-Figure 3.1c depicts the vertical P- and S-wave velocities along with the density model $[V_{P0}, V_{S0}, \rho]$ as the background medium parameters where all of the complex aforementioned geological structures can be observed.

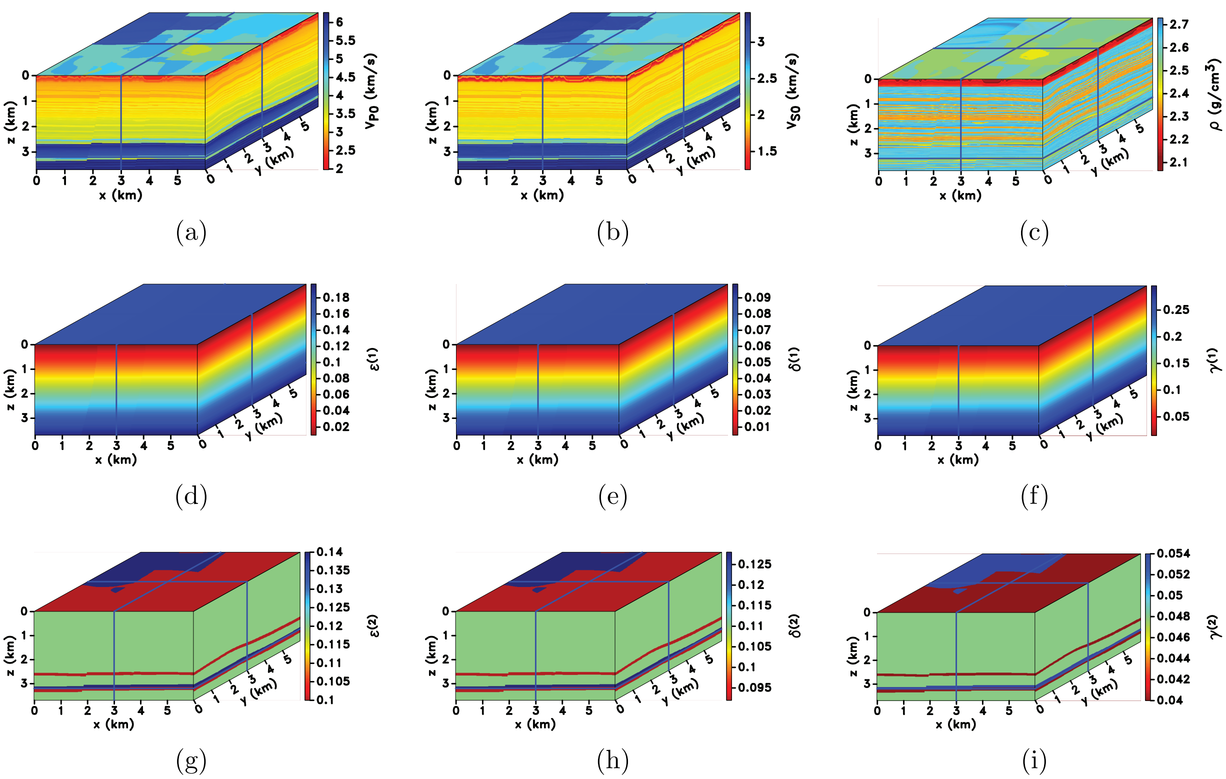

(a) (b) (c)

(d) (e) (f)

(g) (h) (i)

Figure 3.1 The Barrett Unconventional model: Vertical (a) P- and (b) S-wave velocity, and (c) density model components; anisotropy coefficients (d) $\epsilon^{(1)}$, (e) $\delta^{(1)}$, and (f) $\gamma^{(1)}$ along the $[y, z]$-symmetry plane for VTI media, and (g) $\epsilon^{(2)}$, (h) $\delta^{(2)}$, and (i) $\gamma^{(2)}$ along the $[x, z]$-symmetry plane for HTI media. The azimuthal angle defined for the original HTI model is set to 0° in our numerical experiments.

The Barrett model was designed to let users choose from two types of transverse isotropy, VTI and HTI, where the combination of these two models leads to ORT anisotropy (Regone et al., 2017). The anisotropy coefficients [$\epsilon^{(1)}$, $\delta^{(1)}$, $\gamma^{(1)}$] for VTI media are described with linear trends with depth (Figure 3.1d-Figure 3.1f) while the anisotropy coefficients [$\epsilon^{(2)}$, $\delta^{(2)}$, $\gamma^{(2)}$] for HTI media are set to constant values for outside the shale reservoirs and are specified independently within the two shale layers (Figure 3.1d-Figure 3.1f). The azimuthal angle, set to 0° in our numerical experiments, is the HTI model parameter specifying the spatial orientation of the symmetry axis. We also increase the magnitude of the HTI anisotropy model parameters by scaling the original parameters by a factor of two to make them comparable with the VTI parameters. Note that Figure 3.1d-Figure 3.1f presents the scaled HTI model. Finally, combining the VTI and HTI models creates an ORT model that uses six anisotropy coefficients [$\epsilon^{(1)}$, $\delta^{(1)}$, $\gamma^{(1)}$, $\epsilon^{(2)}$, $\delta^{(2)}$, $\gamma^{(2)}$] in addition to $[V_{P0}, V_{S0}]$ (Tsvankin, 1997, 2012). (We note that $\delta^{(3)}$ is not included in the SEAM Barrett model.) In the following numerical experiments, we independently use the VTI, HTI, and ORT models in the imaging tests to examine the sensitivity of the TRI procedure and the resulting images to the various anisotropy parameters.

3.5 Numerical examples

In our numerical experiments, we use 3D anisotropic elastic forward and adjoint (time-reverse) propagators designed using a stress-displacement formulation on a singly staggered grid (SSG). The propagators are based on finite-difference time-domain (FDTD) solutions of the elastic wave equation with a second-order temporal and an eighth-order spatial accuracy stencil that use a graphics processing unit (GPU)-based architecture to accelerate the computation (Weiss and Shragge, 2013).

The original dimensions of the Barrett model are $[N_x, N_y, N_z] = [400, 400, 600]$ grid points at spatial increments of $[\Delta x, \Delta y, \Delta z] = [0.025, 0.025, 0.00625]$ km. Forward-modeled microseismic data are recorded at a surface acquisition geometry extracted from a field experiment (Witten and Shragge, 2017b). The receiver array includes 192 non-uniformly distributed 3C multicomponent receivers covering an approximately 6×6 km^2 area with a 390 m nominal inline and crossline spacing (see Figure 3.2). To make our receiver configuration consistent with the Barrett model, we reduce the size of the original model by selecting every other sample and interpolating it in the lateral spatial dimensions. After this modification, the model has $[N_x, N_y, N_z] = [200, 200, 300]$ grid points at spatial increments of $[\Delta x, \Delta y, \Delta z] = [0.03, 0.03, 0.0125]$ km.

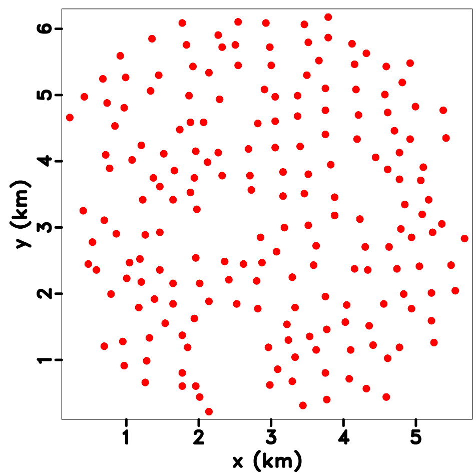

Figure 3.2 Illustration of receiver geometry employed in the numerical experiments. The red dots indicate the locations of the multicomponent receivers deployed at the surface.

We generate a hypothetical microseismic source located at the lower reservoir level $[x, y, z] = [3.0, 3.0, 3.2]$ km using a 25 Hz Ricker wavelet and a $\Delta t = 1$ ms time sampling. We use a moment tensor source (m_{ij} in equation 3.1) oriented at 45° with respect to the horizontal axis with nonzero stress components of m_{xx}=-1 and m_{zz}=1. With this numerical setup, we perform 3D forward modeling using N_t=2400 time steps with no free-surface boundary condition applied. The runtime for the 3D anisotropic elastic forward modeling is about 60 s on a single NVIDIA V100 GPU card.

3.5.1 Experiment 1: Anisotropic TRI for different model parameterizations

Our first numerical experiment investigates the anisotropic TRI results generated by applying the (extended) PS energy and energy imaging conditions (equations 3.5 and 3.4) to confirm that they generate well-focused event images in anisotropic media under correct conditions. We first perform 3D elastic forward modeling to generate the microseismic data on the sparse receiver grid. This step is followed by injecting and backpropagating the recorded data as well as evaluating the imaging conditions given in equations 3.4 and 3.5 at each time step. As previously indicated, the following anisotropic TRI experiments are conducted in VTI, HTI, and ORT media that are respectively characterized by the anisotropy parameters $[V_{P0}, V_{S0}, \epsilon^{(1)}, \delta^{(1)}, \gamma^{(1)}]$, $[V_{P0}, V_{S0}, \epsilon^{(2)}, \delta^{(2)}, \gamma^{(2)}]$, and $[V_{P0}, V_{S0}, \epsilon^{(1)}$, $\delta^{(1)}$, $\gamma^{(1)}$, $\epsilon^{(2)}$, $\delta^{(2)}$, $\gamma^{(2)}]$ shown in Figure 3.1.

Figure 3.3 presents the zero-lag PS energy and energy images constructed in VTI, HTI, and ORT media. For improved visualization, we display close-up sections from the original image volumes. Using the correct models in the TRI procedure, both imaging conditions accurately handle the existing anisotropy and yield strong coherently focused energy at the true source location, which is indicated by the intersecting cross-hair lines on the 3D image panels. The results show that while the PS energy images produce a positive peak amplitude at the correct source location, the energy images generate a negative peak amplitude. The energy images exhibit a negative peak amplitude at the true source coordinates as a result of the subtraction procedure in equation 3.4 applied to attenuate the low-wavenumber artifacts. For HTI and ORT media, we also note that the elastic TRI procedure using either imaging condition accounts for the complex S-wave splitting phenomena after time-reversing the wavefield through accurate anisotropy models (Alford, 1986; Crampin, 1985). Because the source initiation time is known for these synthetic examples, we compute the zero-lag images in the time window $[t_{min}, t_{max}] = [0, 0.15]$ s. We also apply a 40-sample cosine taper to the partial images along the edges of the time window to further enhance the S/N of the resulting stacked image.

Figure 3.4 shows the 3D EIC gathers computed with the PS energy and energy imaging conditions. Each EIC gather is evaluated at the true source location that respectively corresponds to the maximum and minimum amplitude points of the zero-lag PS energy and energy images shown in the corresponding panels of Figure 3.3. Because the TRI procedure in this experiment uses the correct anisotropic models, the EIC gathers exhibit energy that is well-focused at zero lag, though with slightly differing amplitudes.

This experiment illustrates that both the PS energy and energy imaging conditions can handle anisotropy due to the explicit dependence on c_{ijkl} in the formulations. Because of the challenges of robustly estimating anisotropic model parameters, though, TRI is routinely performed by simply making an isotropic media assumption. Hence, it is important to examine the effects of such erroneous model assumptions on the resulting event images.

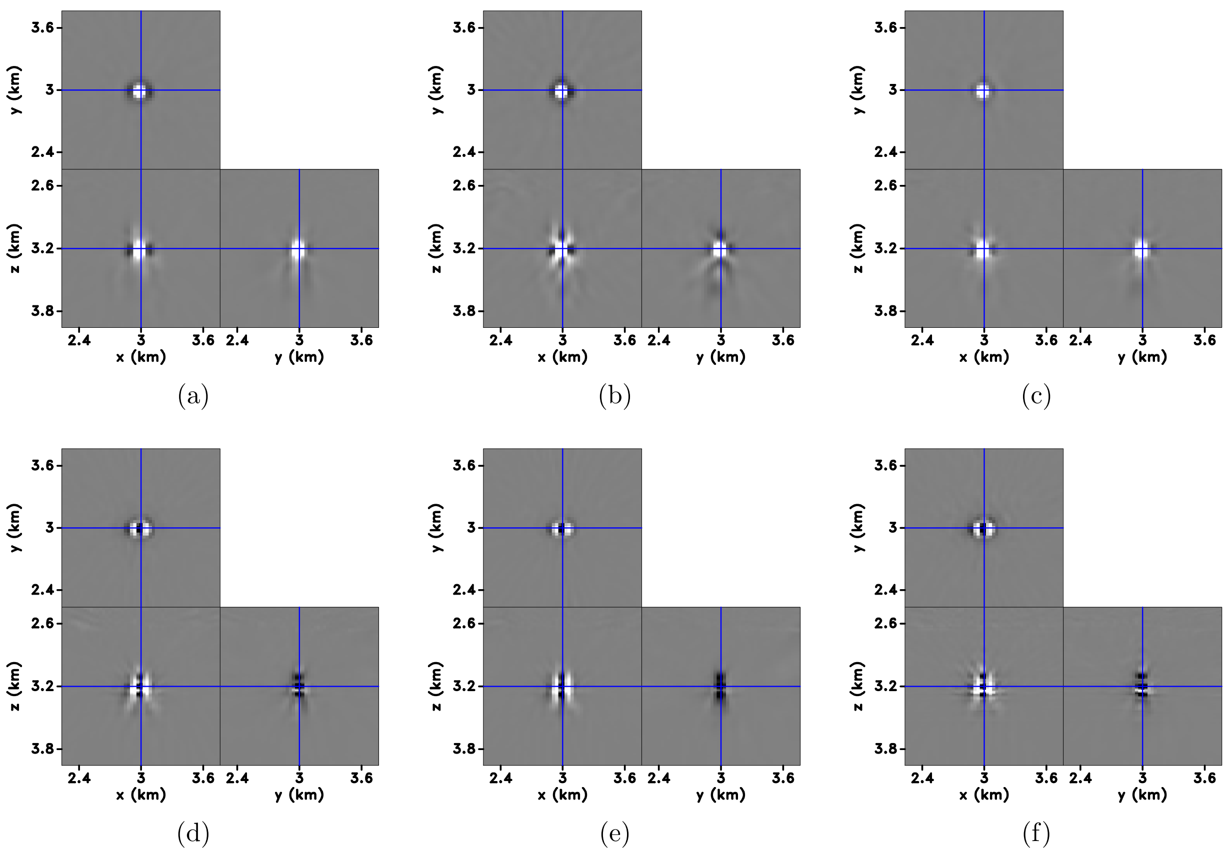

Figure 3.3 Close-up sections of the 3D elastic zero-lag (a)-(c) PS energy and (d)-(f) energy images computed in (a) and (d) VTI, (b) and (e) HTI, and (c) and (f) ORT media. The intersecting cross-hair lines denote the true source location, which corresponds to the maximum image focus for all cases. Both imaging conditions accurately handle the existing anisotropy and produce a focused peak at the correct source location.

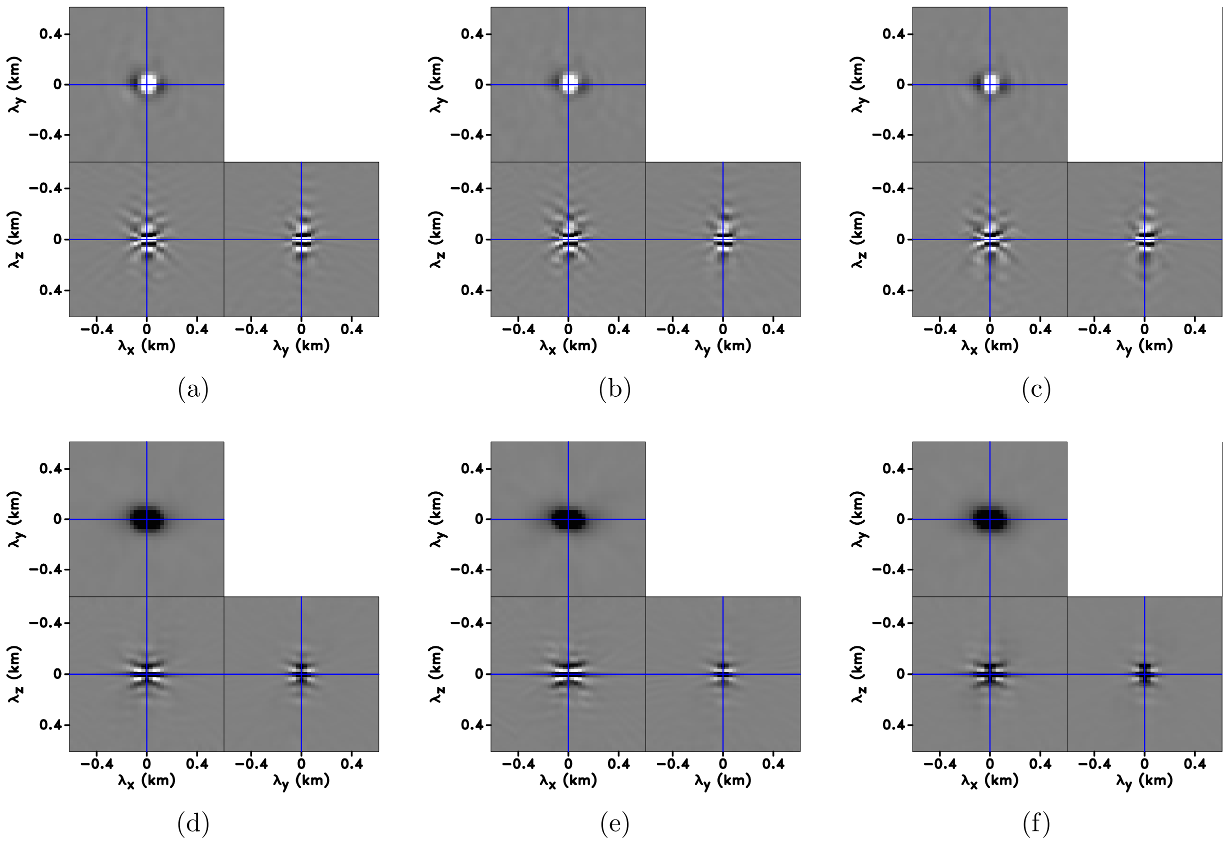

Figure 3.4 3D space-lag (a)-(c) PS energy and (d)-(f) energy EIC gathers for (a) and (d) VTI, (b) and (e) HTI, and (c) and (f) ORT media. We evaluate the EIC gathers at the maximum amplitude point, which corresponds to the true source location for all cases. The energy is well-focused at zero lag for all extended images due to the correct models used in the elastic TRI process.

3.5.2 Experiment 2: Isotropic TRI of anisotropic microseismic data

This experiment analyzes the consequences of using an isotropic TRI operator for the anisotropic 3C microseismic data forward modeled in VTI, HTI, and ORT media, with the goal of understanding the characteristic moveout and sensitivity of imaged events when ignoring anisotropy during the TRI process. For the isotropic TRI, we use the vertical P- and S-wave velocity and density models $[V_{P0}, V_{S0}, \rho]$ shown in Figure 3.1a-Figure 3.1c as the background isotropic medium parameters $[V_P, V_S, \rho]$.

We begin by investigating the sensitivity of the PS energy and energy imaging results to the isotropic TRI of the VTI microseismic data. Figure 3.5a and Figure 3.5d respectively present the zero-lag PS energy and energy images. The zero-lag PS energy image exhibits increased sensitivity (i.e., greater defocusing and event mislocation) to the erroneous isotropic TRI operator compared to the relatively better focused zero-lag energy image. Similarly, the corresponding PS energy EIC gather (Figure 3.6a) evaluated at the maximum amplitude point of the zero-lag image shows greater sensitivity to the incorrect isotropic TRI operator compared to the corresponding energy EIC gather volume (Figure 3.6d) that we evaluate at the negative peak amplitude point of the zero-lag energy image. In particular, the focal maximum of the extended PS energy image separates from zero lag in the λ_z-axis while the energy about zero lag of the energy EIC gather slightly spreads out along the λ_z- and λ_y-axes. In contrast to less sensitive imaging conditions that can yield a wavefield focus at an incorrect event location, this increased sensitivity of the PS energy imaging condition can be exploited to generate refined anisotropic models through image-domain inversion and thereby reduce the event location uncertainty present due to model-induced misfocusing and associated event location errors.

We also examine the sensitivity of both imaging conditions to the isotropic TRI of the HTI microseismic data. Similar to the isotropic imaging of the VTI data experiment, the focusing of the zero-lag and extended PS energy images (Figure 3.5b and Figure 3.6b) appears to be distorted more dramatically than the energy images (Figure 3.5e and Figure 3.6e). Because the magnitude of the anisotropy of the HTI model is slightly stronger than that of the VTI model for the most part, we observe that PS energy images inherently exhibit a higher degree of misfocusing.

Lastly, we conduct the same experiment for ORT media where the resulting zero-lag PS energy and energy images (Figure 3.5c and Figure 3.5f) appear quite distorted and behave similarly with respect to an inaccurate isotropic assumption during the TRI step. Again, the PS energy EIC gather (Figure 3.6c) shows a result similar to the energy EIC gather

(Figure 3.6f), with energy highly distorted throughout the image volumes. As one may expect, the isotropic imaging of ORT data produces more distorted results compared to the VTI and HTI models due to its more complex parameterization and compounded effects of the two anisotropy models.

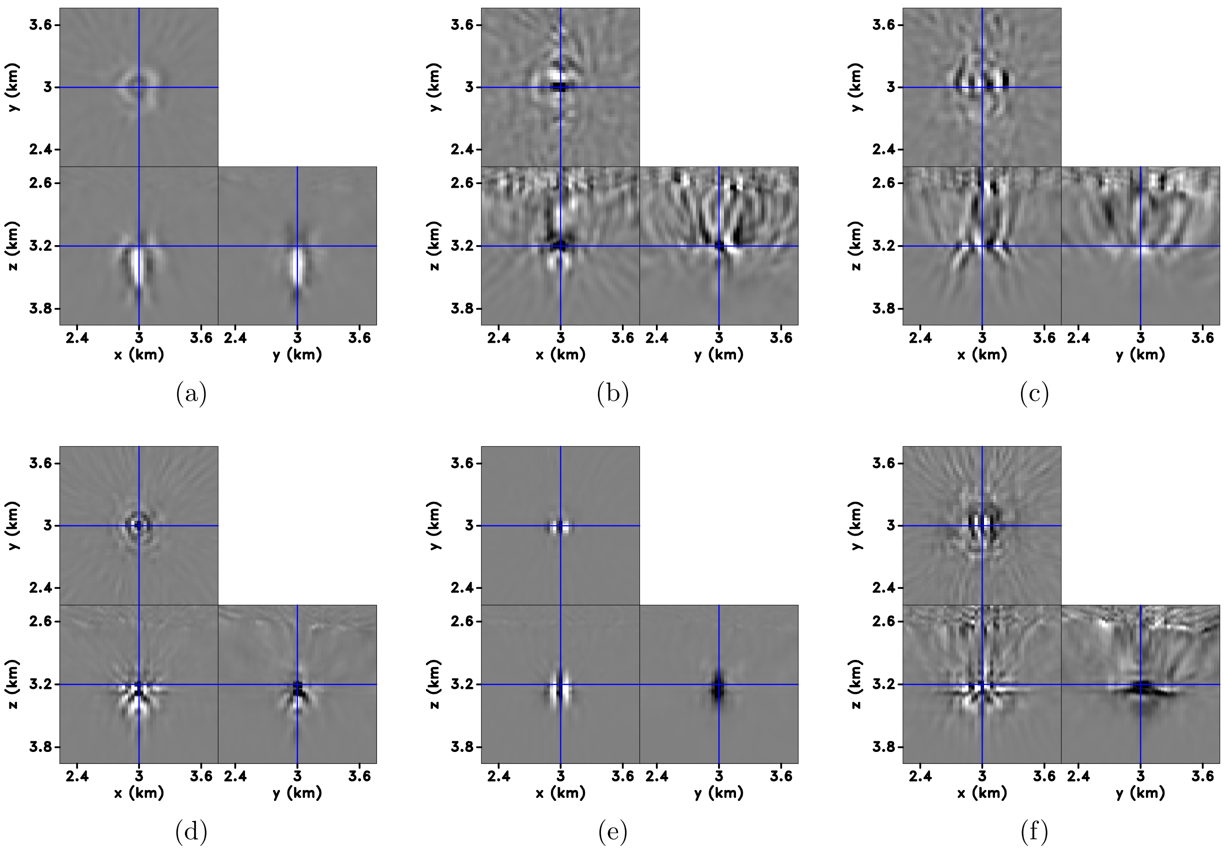

Figure 3.5 3D zero-lag images constructed using the (a)-(c) PS energy and (d)-(f) energy imaging conditions. The source images are obtained by the isotropic TRI of the (a) and (d) VTI, (b) and (e) HTI, and (c) and (f) ORT microseismic data. Compared to the energy images, the PS energy images have increased sensitivity with respect to the incorrect isotropic TRI operator.

The PS energy image in Figure 3.5a is less noisy compared to those presented in Figure 3.5b and Figure 3.5c, which we attribute to the time-reversal accuracy of the backpropagated VTI data being mostly controlled by the true vertical velocities used in the TRI process. The anisotropy coefficients $[\epsilon^{(1)}, \delta^{(1)}, \gamma^{(1)}]$ neglected in the isotropic migration of the VTI data, though, lead to a bulk shift of the imaged event from the true source location.

Furthermore, despite ignoring the $[\epsilon^{(2)}, \delta^{(2)}, \gamma^{(2)}]$ anisotropy parameters in the HTI imaging process, the energy image in Figure 3.5e exhibits a clear focus at the source location. Thus, this image seems to be the most ideal among the other energy images in Figure 3.5d and Figure 3.5f, which we attribute to imaging with the correct models in the HTI isotropy plane.

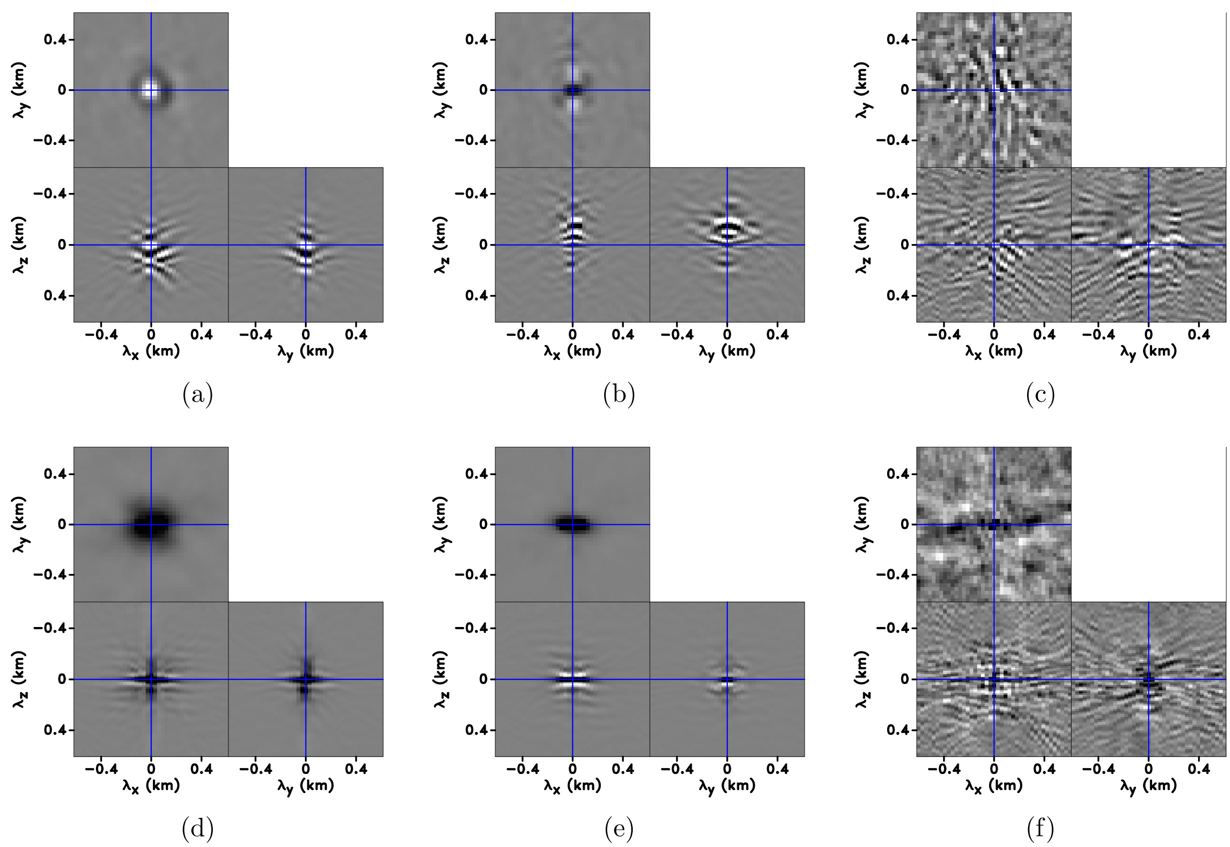

Figure 3.6 3D EIC gathers constructed through the (a)-(c) PS energy and (d)-(f) energy imaging conditions. The EIC gathers are obtained by the isotropic TRI of the (a) and (d) VTI, (b) and (e) HTI, and (c) and (f) ORT microseismic data and are evaluated at the maximum and minimum amplitude points of the zero-lag PS energy and energy images in Figure 3.5, respectively. The PS energy EIC gathers exhibit more interpretable moveout patterns as opposed to the energy EIC gathers showing minimal sensitivity particularly for VTI and HTI media.

This experiment shows that the incorrect isotropic media assumption in the TRI process leads to visible distortions on the imaged events. Also, both imaging conditions exhibit complementary sensitivity attributes for different types of TI symmetries. However, using the enhanced sensitivity of PS energy images, quantifying the location errors of estimated source locations can provide further insights into the anisotropic effects of different TI media on the microseismic imaging process.

3.5.3 Experiment 3: Event location errors when ignoring anisotropy

Our third experiment examines the event location errors estimated from the zero-lag PS energy images when using the correct and incorrect models for microseismic data modeled in VTI, HTI, and ORT media. The event location estimations are calculated based on the peak positive amplitude of imaged events. As in Experiment 2, when building the incorrect model, we assume isotropic media for TRI and examine the misposition error based on the Euclidean distance metric between the estimated and true source positions. The experiment involves 16 microseismic events covering a uniform 4×4 spatial grid at the reservoir interval (z=3.2 km). The events are located at a starting point of $[x, y, z] = [1.5, 1.5, 3.2]$ km with a 1 km incremental grid spacing in the $x-$ and $y-$ directions.

Figure 3.7 displays a crossplot of event location errors estimated by elastic TRI of VTI, HTI, and ORT data when using the correct and incorrect models as shown on the horizontal and vertical axes, respectively. Due to the relatively coarse model grid spacing, $[\Delta x, \Delta y, \Delta z] = [0.03, 0.03, 0.0125]$ km, and irregular and sparse surface acquisition, the source locations estimated using the correct models can deviate from the true locations by up to 50 m, which corresponds to a few image pixels. Except for the two location errors greater than 500 m, the errors computed when using the isotropic model to image the HTI data are scattered around 100 m and appear to be the least affected by the incorrect model assumption among the three cases due to using the correct parameters for waves propagating within the HTI model isotropy plane. The errors calculated in VTI media fall between $130 - 180$ m and are slightly less accurate than the HTI media results. Finally, due to the combined distortions in parameters $[\epsilon^{(1)}, \delta^{(1)}, \epsilon^{(2)}, \delta^{(2)}]$, the location errors in ORT media are typically $500 - 750$ m, which represents a substantial degradation compared to the VTI and HTI media results. (The sensitivity to γ parameter perturbations is examined in the following experiment.) This suggests that even though the VTI parameters of the formation are well constrained, the presence of HTI anisotropy (i.e., vertical fractures) could cause significant event mispositioning errors, even for models with relatively straightforward geological structures.

This experiment illustrates the sensitivity of zero-lag PS energy images by examining event location errors that vary depending on the type and magnitude of TI anisotropy. Overall, the highlighted sensitivity of PS energy images motivates us to perform further analysis. In particular, we investigate whether this imaging approach has sufficient sensitivity with respect to perturbations in anisotropy parameters that may be useful for anisotropic model quality control as well as computing accurate tomographic updates through image-domain inversion.

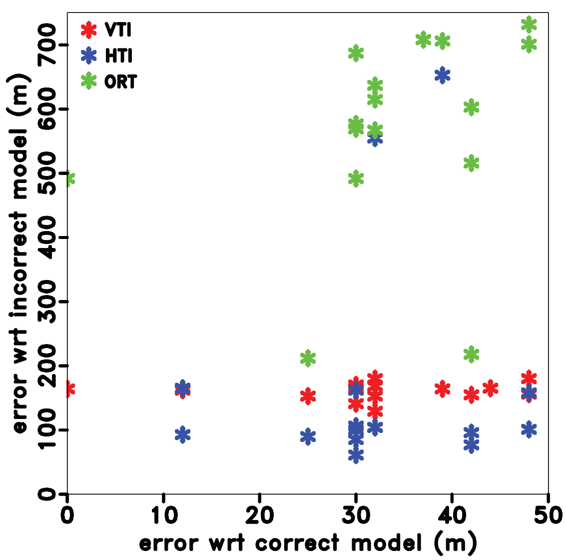

Figure 3.7 Crossplot of event location errors estimated by elastic TRI using the PS energy imaging condition with respect to (wrt) the correct and incorrect (isotropic media assumption) models for microseismic data modeled in VTI (red stars), HTI (blue stars), and ORT (green stars) media. The combination of VTI and HTI model errors generates significantly more location errors in the ORT scenario than those caused by VTI and HTI model errors alone.

3.5.4 Experiment 4: Sensitivity to errors in anisotropy parameters

The final experiment investigates the sensitivity of the PS energy images to the erroneous VTI and HTI model parameters. We create the incorrect models by globally increasing or decreasing the original anisotropy coefficients $[\epsilon^{(1)}, \delta^{(1)}]$ and $[\epsilon^{(2)}, \delta^{(2)}]$ by $\pm 50\%$ for the VTI and HTI media experiments, respectively. This creates nine different model scenarios, only one of which is correct. In addition, because Oren and Shragge (2021a) already perform a detailed sensitivity analysis for TRI results with respect to velocity inaccuracy, we do not perturb the P- and S-wave vertical velocities $[V_{P0}, V_{S0}]$ in this experiment.

Figure 3.8 displays the zero-lag PS energy images computed with the perturbed anisotropy parameters $[\epsilon^{(1)}, \delta^{(1)}]$ in VTI media. In general, the TRI results show that the erroneous $\epsilon^{(1)}$ models lead to greater amount of misfocused energy on the PS energy images relative to the erroneous $\delta^{(1)}$ scenarios. Similarly, the corresponding extended PS energy images in Figure 3.9 exhibit noticeable defocusing along with interpretable moveout patterns due to the errors in $[\epsilon^{(1)}, \delta^{(1)}]$.

Figure 3.10 shows the zero-lag PS energy images calculated using the perturbed anisotropy coefficients $[\epsilon^{(2)}, \delta^{(2)}]$ in HTI media. Similar to the previous analysis in VTI media, perturbations in $\epsilon^{(2)}$ typically lead to more noticeable defocusing in the TRI results compared to those in $\delta^{(2)}$. Figure 3.11 depicts the associated extended PS energy images generally featuring more distinguishable over- and under-migration tails about zero lag compared to the VTI results in Figure 3.9.

We also demonstrate that zero-lag and extended PS energy images show almost no sensitivity to perturbations in $[\gamma^{(1)}, \gamma^{(2)}]$ in VTI and HTI media for the Barrett model. Similar to the previous analyses, we create incorrect models by globally increasing or decreasing the original $\gamma^{(1)}$ and $\gamma^{(2)}$ parameters by $\pm 50\%$ for the VTI and HTI experiments, respectively. Prior to presenting the imaging results, we first analyze the forward modeled data generated with the true and perturbed models. Because $[\gamma^{(1)}, \gamma^{(2)}]$ are mainly responsible for the S-wave kinematic signatures, we pick the S-wave arrival times based on their maximum amplitudes on the x-component. Figure 3.12a presents the modeling results for VTI media where the difference between the picked arrival times at near offsets is negligible, whereas relatively minor time shifts occur and tend to gradually increase from mid-to-far offsets due to the perturbed $\gamma^{(1)}$. Thus, because there are minimal traveltime differences in the data, one should expect limited sensitivity in the image domain. Moreover, Figure 3.12b shows the S-wave arrival times calculated in HTI media where the kinematic signatures observed are mostly identical, and exhibit less variation at mid-to-far offsets compared to the VTI case. We attribute this to the $\gamma^{(2)}$ model (Figure 3.1i) exhibiting lower magnitude of anisotropy relative to $\gamma^{(1)}$ (Figure 3.1f).

Figure 3.13a and Figure 3.13b shows the zero-lag PS energy images computed with the $\pm 50\%$ perturbed $\gamma^{(1)}$ parameter in VTI media. Despite being considerable perturbations, the resulting images still preserve the focusing at the true event location. The PS energy EIC gathers in Figure 3.13e and Figure 3.13f similarly feature energy well-focused at zero lag. Figure 3.13c and Figure 3.13d display the zero-lag PS energy images constructed using the $\pm 50\%$ perturbed $\gamma^{(2)}$ parameter in HTI media. Similar to the VTI experiment, the errors in $\gamma^{(2)}$ appear to not influence the energy focusing at the correct source location. The corresponding PS energy EIC gathers in Figure 3.13g and Figure 3.13h still exhibit focused energy at zero lag. Overall, the forward modeling and imaging results are inherently correlated and consistent with the interpretation of minimal sensitivity to the γ parameters.

Unlike the sensitivity results with respect to the parameters [$\epsilon^{(1)}$, $\delta^{(1)}$, $\epsilon^{(2)}$, $\delta^{(2)}$] presented earlier in this section, the insensitivity to perturbations in $[\gamma^{(1)}, \gamma^{(2)}]$ for VTI and HTI media suggests that they are not useful as a diagnostic for model error and would be inappropriate to include in an anisotropy parameterization for image-domain anisotropic model building. However, it is critical to highlight that these observations of insensitivity may be specific to the Barrett Unconventional model and the surface modeling parameters (e.g., magnitude of anisotropy, source and receiver configuration, and aperture angles) used in this numerical study to generate the sensitivity results.

3.6 Discussion

Determining the time window parameters $[t_{min}, t_{max}]$ through trial and error based on the image focusing quality could be problematic particularly for field investigations due to the unknown origin time of real events. However, for both synthetic and field investigations, one can consider at least two different approaches (other than trial and error) for designing the time windows. First, one could apply the imaging condition only after injecting the earliest arrival of energy from a microseismic event. This is because there is no benefit in evaluating the imaging condition before all of the energy associated with the event has been injected. One could further hold off applying the imaging condition until the apex of the time-reversed P-wavefield energy has reached a user-defined minimum depth. Thus, examining the earliest arrival time of an event could be a useful step to reduce the uncertainty of window lengths. Second, one could investigate the time interval when the backpropagated P and/or S wavefields collapse back to and exit from a focus. One could stop the time-reverse simulation, start moving forward in time, and begin applying the imaging condition over the temporal range of focusing.

The numerical experiments presented herein demonstrate that one may infer information about the anisotropy model parameter accuracy using the PS energy imaging condition. The sensitivity analysis results show that the focusing in the (extended) PS energy images is not only influenced by the vertical P- and S-wave velocities (Oren and Shragge, 2021a), but also by the anisotropy coefficients $[\epsilon, \delta]$ in different TI symmetries. The Barrett model results demonstrate that the moveout sensitivity of ϵ on microseismic event images is slightly greater than that of δ, while the combination of ϵ and δ errors can lead to the more complex defocusing patterns observed in Figure 3.9 and Figure 3.11. In addition, it is likely judicious to consider excluding γ in an inversion model parameterization due to the lack of sensitivity to this parameter in the TRI process. However, the influence of γ may be more significant than the presented analysis results based on the Barrett model depending on a particular model's degree of anisotropy, source and receiver configuration, and resulting aperture angles.

Overall, the extended PS energy imaging condition appears as a suitable candidate for anisotropic inversion algorithms to generate accurate 3D anisotropic models. Our anisotropic sensitivity analysis provides a qualitative measure in terms of determining a prospectus for inversion parameterization. Such an inversion procedure can lead to more robust model parameter recovery, which in turn could yield more accurate source location estimates from TRI analyses.

3.7 Conclusions

We present a sensitivity analysis study of the anisotropy signature in zero-lag and extended PS energy and energy images for VTI, HTI, and ORT models. Using the realistic SEAM Barrett Unconventional model, we analyze the two imaging conditions using the accurate and inaccurate models to test their sensitivity to anisotropy parameters. The TRI results show that the PS energy imaging condition generates results that exhibit greater sensitivity to anisotropy model parameters relative to its energy imaging condition counterpart. The PS energy images feature a range of complementary moveout patterns caused by different perturbations to anisotropy parameters. The event images typically are influenced by errors in $[\epsilon, \delta]$, but exhibit almost no sensitivity to γ. We also quantify event location errors for the aforementioned TI symmetries by making an isotropic media assumption in imaging. While we observe similar event location errors in the Barrett model for VTI and HTI media, these errors are more significant for ORT media. We assert that the sensitivity observed on the extended PS energy images is useful for evaluating the accuracy of the anisotropy model accuracy within the concept of 3D image-domain anisotropic elastic inversion of passive seismic data.

3.8 Acknowledgments

We thank associate editor Y. E. Li and two reviewers for their comments, which improved the quality of the manuscript. We acknowledge the Center for Wave Phenomena (CWP) consortium sponsors for their financial support. We also thank the SEAM consortium for developing and the Reservoir Characterization Project for providing access to the Barrett Unconventional model. The reproducible numerical examples in this paper were generated using the Madagascar software package using the Wendian HPC systems made available through the Colorado School of Mines.

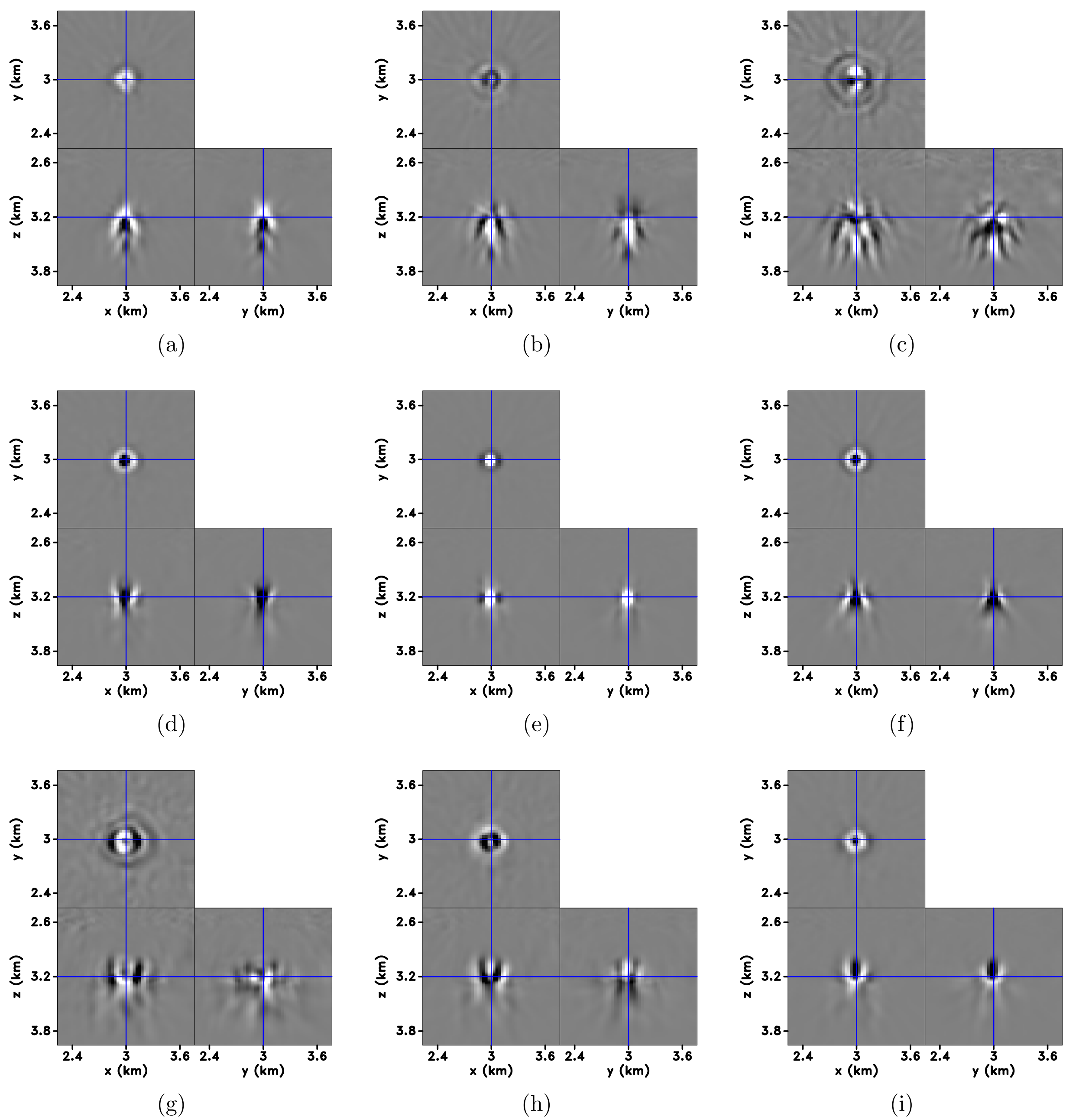

Figure 3.8 Zero-lag PS energy images with incorrect anisotropy parameters in VTI media. Top, middle and bottom rows correspond to -50%, 0%, +50% global perturbations in the $\epsilon^{(1)}$ parameter. Left, middle and right columns correspond to -50%, 0%, +50% global perturbations in the $\delta^{(1)}$ parameter. Note the unfocused events with respect to the focused energy in (e), which is obtained with the correct anisotropy parameters.

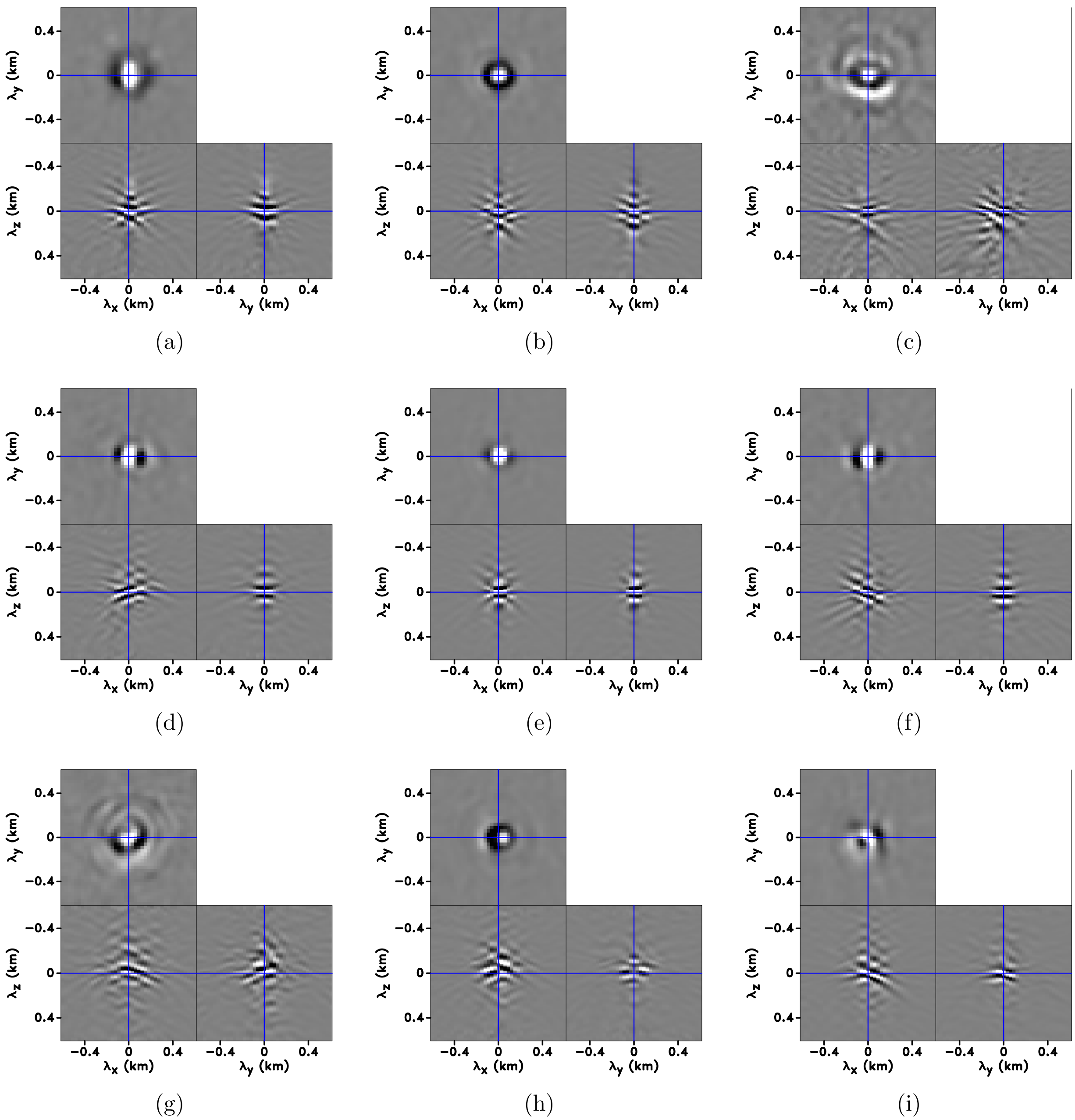

Figure 3.9 PS Energy EIC gathers corresponding to those presented in Figure 3.8. PS Energy EIC gathers are evaluated at the maximum amplitude point of the related zero-lag energy images in Figure 3.8.

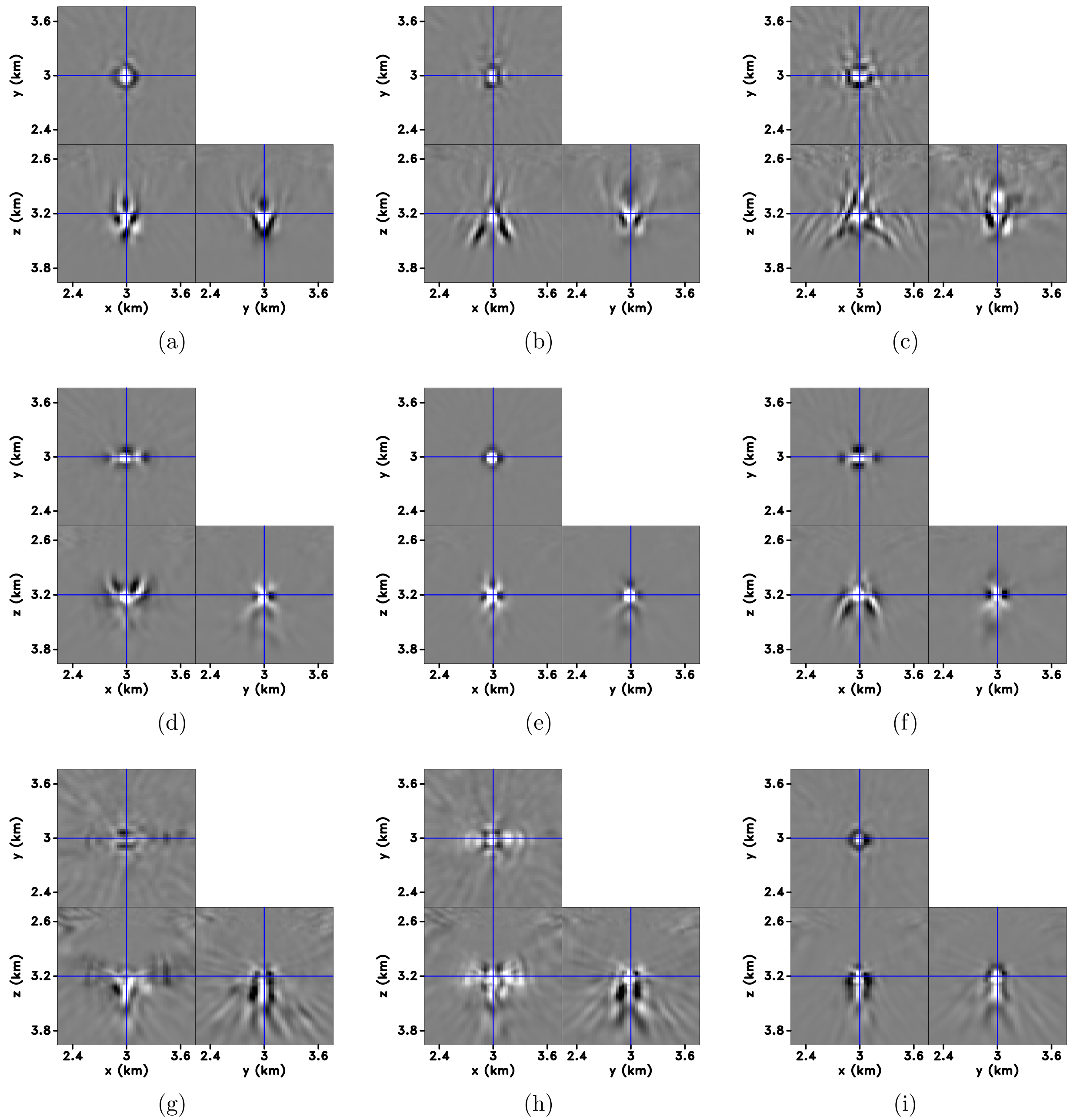

Figure 3.10 Zero-lag PS energy images with incorrect anisotropy parameters in HTI media. Top, middle and bottom rows correspond to -50%, 0%, +50% global perturbations in the $\epsilon^{(2)}$ parameter. Left, middle and right columns correspond to -50%, 0%, +50% global perturbations in the $\delta^{(2)}$ parameter. Note the unfocused events with respect to the focused energy in (e), which is obtained with the correct anisotropy parameters.

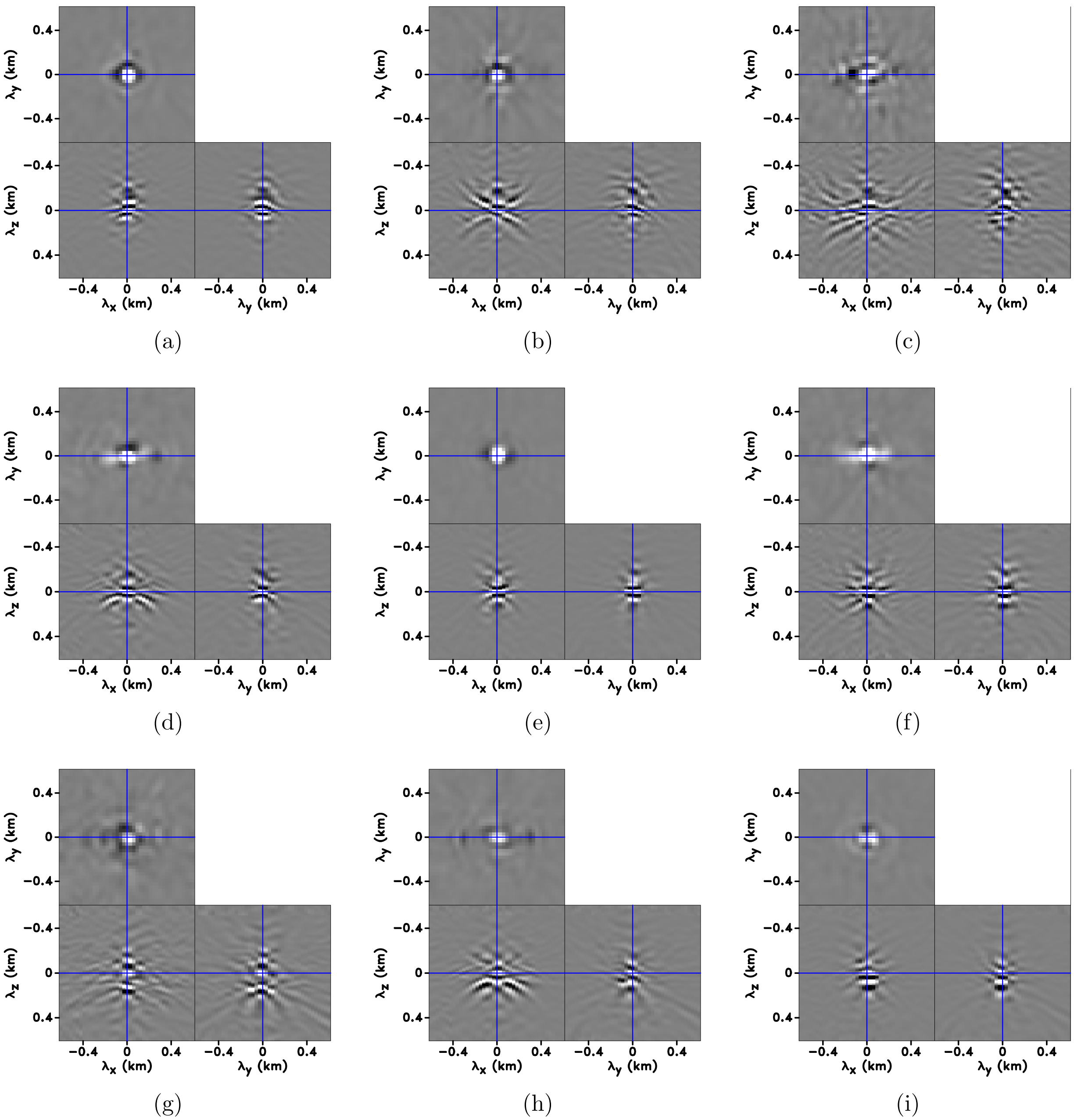

Figure 3.11 PS Energy EIC gathers corresponding to those presented in Figure 3.10. PS Energy EIC gathers are evaluated at the maximum amplitude point of the related zero-lag energy images in Figure 3.10.

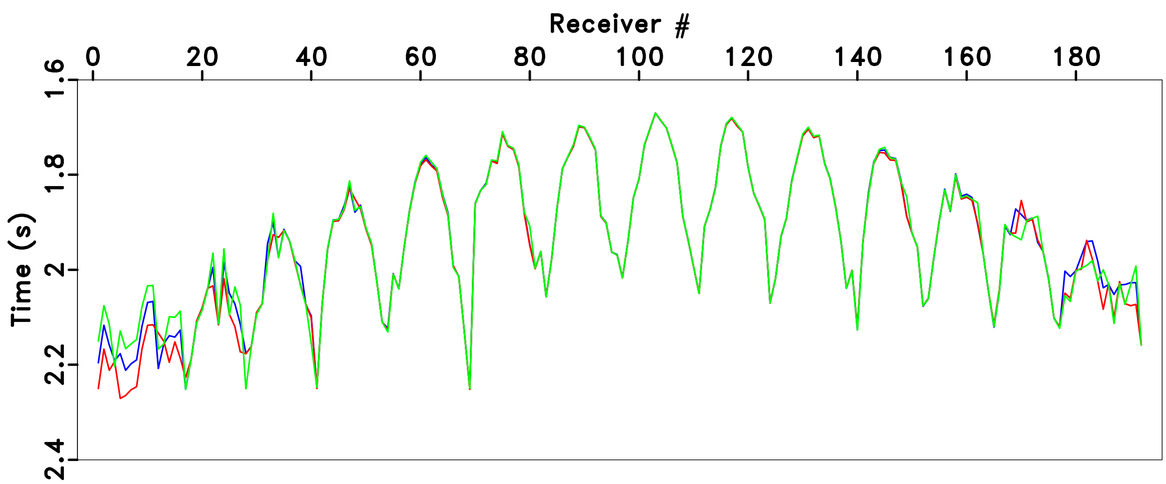

(a)

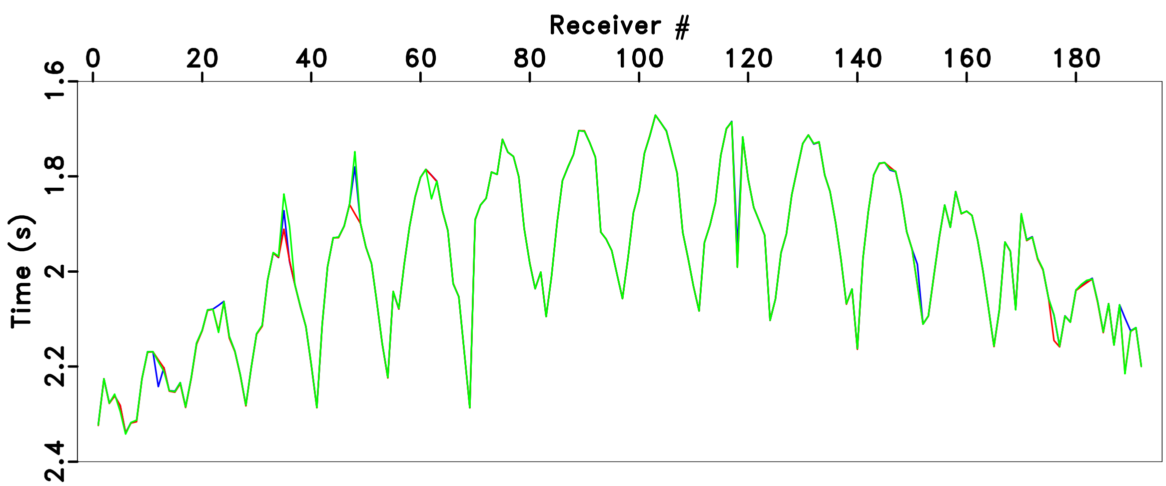

(b)

Figure 3.12 S-wave arrival times picked from the simulated u_x component of 3C microseismic data for (a) VTI and (b) HTI media. Blue curves denote the arrival times calculated using the original $[\gamma^{(1)}, \gamma^{(2)}]$ while red and green curves show the arrival times computed with -50% and $+50\%$ perturbed $[\gamma^{(1)}, \gamma^{(2)}]$, respectively.

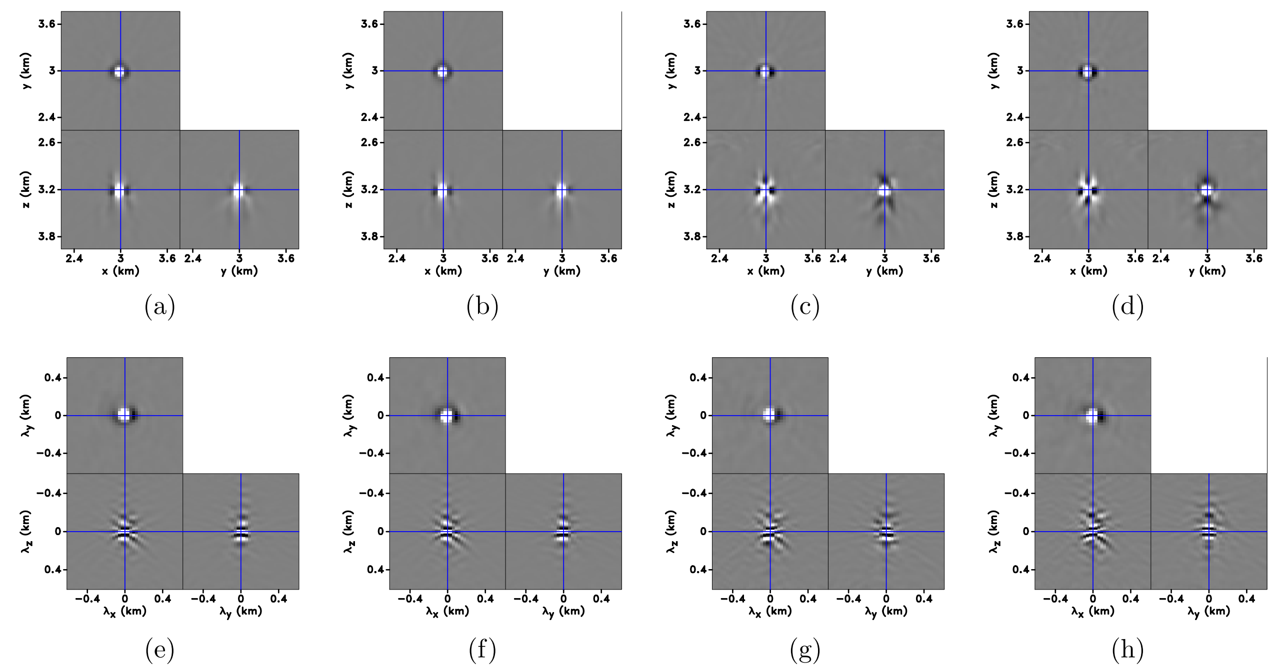

Figure 3.13 (a)-(d) 3D zero-lag and (e)-(h) extended PS energy images constructed with $\pm 50\%$ global perturbations in $[\gamma^{(1)}, \gamma^{(2)}]$ for VTI and HTI media. The images in (a) and (e) and (b) and (f) respectively correspond to -50% and $+50\%$ perturbed $\gamma^{(1)}$ parameter in VTI media whereas the images in (c) and (g) and (d) and (h) respectively correspond to the -50% and $+50\%$ perturbed $\gamma^{(2)}$ parameter in HTI media. A comparison between these images with those in Figure 3.3a and Figure 3.3b and Figure 3.4a and Figure 3.4b illustrates that PS energy images exhibit almost no sensitivity to $[\gamma^{(1)}, \gamma^{(2)}]$ model errors.

CHAPTER 4

PASSIVE-SEISMIC IMAGE-DOMAIN ELASTIC WAVEFIELD TOMOGRAPHY

A paper published[1] in *Geophysical Journal International*

Can Oren[2,3,4], Jeffrey Shragge[4]

Elastic time-reverse imaging offers a robust wavefield-based approach for locating microseismic events; however, event location accuracy greatly depends on the veracity of the elastic velocity models (i.e., V_P and V_S) used for wave propagation. In this study, we propose a methodology for microseismic image-domain wavefield tomography using the elastic wave equation and zero-lag and extended source images, the focusing of which is used as a quality control metric for velocity models. The objective function is designed to measure the focusing of time-reversed microseismic energy in zero-lag and extended event images. The function applies penalty operators to source images to highlight poorly focused residual energy caused by backpropagation through erroneous velocity models. Minimizing the objective function leads to a model optimization problem aimed at improving the image-focusing quality. P- and S-wave velocity model updates are computed using the adjoint-state method and build on the zero-lag and extended image residuals that satisfy the differential semblance optimization criterion. Synthetic experiments demonstrate that one can construct accurate elastic velocity models using the proposed method, which can significantly improve the focusing of imaged events leading to, e.g., enhanced fluid-injection programs.

4.1 Introduction

Understanding the distribution and properties of passive sources is one of the main objectives in seismic monitoring at a variety of different scales. In unconventional oil and gas

[1]Reprinted with permission of *Geophysical Journal International*, 2022, **228(3)**, 1512–1529
[2]Primary researcher and author.
[3]Author for correspondence
[4]Graduate student and Associate Professor, respectively, Center for Wave Phenomena, Colorado School of Mines, Golden, Colorado, USA.

fields, inferring the locations and mechanisms of (micro-) earthquakes caused by induced or triggered seismicity is crucial for evaluating the success and safety of fluid injection programs such as hydraulic fracturing and waste-water disposal (Maxwell and Urbancic, 2001). Accurate event locations provide useful information when characterizing fracture lengths and heights for hydraulic stimulation as well as analyzing reservoir stress change and potential hazards (Maxwell, 2014; Weingarten et al., 2015). Similarly, at regional and global scales, accurately determining event hypocenters is of particular interest to many geoscientists looking to gain better insight into the spatio-temporal characteristics of faults and their potentially devastating effects (Kiser and Ishii, 2017).

A traditional approach for locating (micro-) earthquakes is based on picking the P- and S-wave arrivals. Given V_P and V_S velocity models, the arrival picks can then be inverted to estimate the spatial location of the recorded event. However, the arrival time information can also be used for tomographic updates to improve velocity models. For instance, the double-difference method commonly used in earthquake seismology relies on traveltime differences between pairs of events or stations to find optimal velocity models and event locations (Waldhauser and Ellsworth, 2000; Zhang and Thurber, 2003). In microseismic monitoring, first-break traveltime tomography is commonly used to calibrate isotropic/anisotropic velocity models along raypaths between perforation shots with known spatial and temporal origin and downhole receiver arrays (Bardainne and Gaucher, 2010; Grechka and Yaskevich, 2013). The success of these phase-based picking approaches is, though, heavily dependent on the robustness of arrival picking process, which is a challenging task for low signal-to-noise ratio (S/N) data.

Alternatively, migration-based event location algorithms have been widely used for passive source scenarios. Like pick-based methods, Kirchhoff-migration techniques require computing ray-traced traveltimes from each candidate event location in the velocity model to each receiver (Baker et al., 2005; Kao and Shan, 2004). The data are then stacked across traveltime trajectories and over source origin times within a moving Gaussian window to find the maximum stack power, which is assumed to represent the event location. Although Kirchhoff techniques are computationally efficient, they struggle for noisy data scenarios, which can affect the accuracy of the stack power by shifting the maximum stack in time and/or space analogous to the aforementioned methods. Moreover, ray-based methods typically rely on simplifying assumptions (e.g., infinite frequency approximation) and thereby have limited ability to handle complex subsurface models (e.g., neglecting multipathing).

Full-wavefield time-reverse imaging (TRI) techniques are a second type of migration approach that recently have gained popularity (Artman et al., 2010; Chambers et al., 2014; Douma and Snieder, 2015; Gajewski and Tessmer, 2005; Nakata and Beroza, 2016; Oren and Shragge, 2021a; Rocha et al., 2019; Witten and Shragge, 2015). By solving the acoustic or elastic wave equation, this class of imaging methods accurately handles wave propagation through complex models, and offers numerous imaging conditions that stack wavefield energy over the time axis, ideally obtaining a well-focused event image. However, TRI methods require computationally expensive wavefield extrapolation as well as accurate velocity models to obtain reliable event location estimates. In most cases, though, such information is not available at monitoring sites due to limited well information (e.g., well logs, perf shots) or other direct or indirect subsurface constraints. This lack of knowledge can lead to inaccurate velocity models that significantly degrade the accuracy of event location estimates. Possible failures in such geophysical observations (e.g., inaccurate location estimates) may comprehensively affect the process of assessing and derisking fluid-injection programs as well as understanding the cause of seismicity.

In TRI applications, the full-wavefield migration-based imaging process typically involves two steps: (1) extrapolating recorded microseismic event data in reverse time through subsurface velocity models (McMechan, 1982), and (2) evaluating an imaging condition (i.e., zero-lag auto/crosscorrelation) that generates a zero-lag image (Artman et al., 2010). If the subsurface model is satisfactorily accurate and judicious preprocessing is applied to the recorded event data (e.g., source radiation pattern mitigation windowing and/or noise elimination), the peak amplitude of the resulting zero-lag image can be inferred as the correct spatial event location. In such ideal conditions, one can produce complementary PP, SS, and PS zero-lag images by autocorrelating and crosscorrelating the extrapolated P and S wavefields reconstructed from (multicomponent) event data. When these conditions are not met, though, the zero-lag images exhibit erroneous misfocusing energy at incorrect locations. In these instances, a notable shortcoming of zero-lag images is that they rarely provide sufficient information about how to overcome model inaccuracy through velocity updating.

To address the limited sensitivity of zero-lag images to velocity errors, different types of extended imaging conditions have been proposed that may be useful for updating migration velocities for passive seismic scenarios (Oren and Shragge, 2021a; Rocha et al., 2019; Witten and Shragge, 2015). Extended images are an extension of zero-lag images and are calculated by shifting the extrapolated wavefields in space and/or time relative to each other. In microseismic context, extended images are typically calculated at the estimated event location. Velocity accuracy information can be directly extracted from extended image volumes by examining whether energy focuses at or away from spatial/temporal zero correlation lag (Rickett and Sava, 2002; Sava and Fomel, 2006; Sava and Vasconcelos, 2011; Witten and Shragge, 2015). Given sufficiently accurate elastic velocity models, extended images should focus at zero lag and the complementary PP, SS, and PS zero-lag images should produce a focal maximum at the same spatial location due to a self-consistency principle (Witten and Shragge, 2015). For scenarios where inaccurate models are used, zero-lag images will focus at an incorrect spatial location, which would yield energy focused at non-zero lags in the extended domain.

Extended images are successfully used as a quality control tool to update velocity models using image misfocusing criteria for active and passive seismic surveys (Burdick et al., 2013; Oren and Shragge, 2020; Shabelansky et al., 2015; Shen and Symes, 2008; Witten and Shragge, 2017a; Yang and Sava, 2015). Velocity updating can be achieved by differential semblance optimization (DSO) (Symes and Carazzone, 1991), which is one of the most common migration velocity analysis (MVA) model building approaches in exploration seismology. The principle of DSO is to minimize differences between neighboring lags or angles associated with a given reflection (Shen and Symes, 2008). In reflection seismology, common-image-point space- and time-lag gathers are effective at reconstructing P-wave velocity models for complex geologic structures (Díaz and Sava, 2017; Yang and Sava, 2015). Similarly, space-lag common-image-gathers can be constructed through a crosscorrelation-based converted-phase imaging condition to perform elastic MVA to jointly update P- and S-wave models (Shabelansky et al., 2015). For microseismic data, Witten and Shragge (2017a) develop a pseudo-acoustic image-domain inversion method to invert for P- and S-wave velocity models and successfully apply it to a 3D field data set (Witten and Shragge, 2017b).

There are several advantages of full-wavefield microseismic image-domain tomography methods. They require neither first-arrival picking nor the origin time of events, which can be problematic to determine for surface-recorded data exhibiting low S/N. Also, unlike the recently published full waveform inversion (FWI) approaches (Sun et al., 2016; Wang and Alkhalifah, 2018), image-domain inversion methods hold less stringent requirements for initial velocity model accuracy to achieve a successful optimization, and thereby is typically less sensitive to the well-known FWI cycle-skipping problem. Moreover, image-domain tomography methods tend to be less sensitive to noise relative to data-domain methods due to the enhanced signal-to-noise achieved by effectively stacking the wavefield energy over the full wavelet and the sensing array through the migration procedure.

In this paper, we present a methodology for computing the isotropic elastic model gradients of an image-domain objective function for surface-recorded microseismic data. To achieve this goal, we first use the kinetic energy term of the PS energy imaging condition (Oren and Shragge, 2021a) to form zero-lag and extended source images. We apply several penalty operators to these images to generate image-domain residuals, which form the basis of a multiterm objective function. Finally, we use the adjoint-state formalism to form the gradients and simultaneously invert for P- and S-wave velocity model parameters. Distinct from the pseudo-acoustic approach proposed by Witten and Shragge (2017a), our methodology is fully elastic and explicitly generalizes to multiparameter anisotropic inversion, though this extension is not explored here. Compared to its pseudo-acoustic counterpart, the elastic implementation allows for a more theoretically accurate handling of multicomponent elastic data and does not require the removal of source radiation pattern as a preprocessing step.

We begin by presenting the imaging condition along with the image-domain penalty functions, the combination of which forms the multiterm objective function to be minimized. Next, we derive expressions for the elastic model gradients through adjoint-state tomography (Plessix, 2006). To demonstrate the effectiveness of our inversion methodology, we present a number of synthetic numerical examples. We first highlight the key ingredients of the proposed method by estimating smooth background perturbations on 2D velocity models. We then present a 3D example using a structurally complex earth model with a realistic source and receiver geometry as a more challenging and "semi-realistic" setting for estimating elastic model updates. Finally, we conclude with a discussion of the advantages and shortcomings of the proposed inversion methodology as well as its possible applications across scales from time-lapse monitoring programs (e.g., carbon capture and storage projects) to regional/global tomography.

4.2 Theory

The image-domain adjoint-state elastic inversion of microseismic data presented herein is comprised of an iterative application of the following steps: (1) inject and individually backpropagate separated multicomponent P- and S-wave data of a single event to reconstruct the wavefields (state variables) using the elastic wave equation (EWE); (2) apply an appropriate elastic imaging condition using the backpropagated P and S wavefields to generate zero-lag and extended source images; (3) evaluate the objective function by summing the image-domain residuals formed by applying penalty operators to annihilate energy consistently focused amongst the zero-lag images and in the vicinity of zero lag in extended images; (4) calculate the adjoint-state variable using the residual energy; (5) form the gradients by correlating the state and adjoint-state variables; (6) use a line-search method to find an optimal step length to scale the model gradients and determine the magnitude of the multiparameter model updates; and (7) update the model parameters. We detail each inversion process step below.

4.2.1 Steps 1 & 2: Elastic time-reverse propagation and imaging

We consider the source-free EWE in a slowly varying isotropic medium in an unbounded domain:

$$\ddot{\mathbf{u}} = \hat{\alpha}\, \nabla(\nabla \cdot \mathbf{u}) - \hat{\beta}\, \nabla \times (\nabla \times \mathbf{u}), \tag{4.1}$$

where $\mathbf{u}(\mathbf{x}, t)$ is the displacement field as a function of space ($\mathbf{x}$) and time (t); $\hat{\alpha}(\mathbf{x})$ and $\hat{\beta}(\mathbf{x})$ are defined through the P- and S-wave velocities (i.e., V_P and V_S) as $\hat{\alpha} = V_P^2 = (\lambda+2\mu)/\rho$ and $\hat{\beta} = V_S^2 = \mu/\rho$; $\lambda(\mathbf{x})$, $\mu(\mathbf{x})$, and $\rho(\mathbf{x})$ are the two Lamé parameters and density, respectively; ∇, $\nabla\cdot$, and $\nabla\times$ are the gradient, divergence, and curl operators; and two superscript dots on the displacement field $\mathbf{u}$ denote second-order time differentiation.

To generate microseismic source images from which we derive event location estimates, we use an elastic TRI procedure involving backpropagating injected P- and S-wave data components separated beforehand through data-domain preprocessing (Oren and Shragge, 2021a) and applying an imaging condition. Because we consider isotropic elastic inversion in this study, we find it sufficient to compute zero-lag and extended source images using only the kinetic energy term of the PS energy imaging condition (Oren and Shragge, 2021a) to derive the gradient terms:

$$I_{\alpha\beta}(\mathbf{x}, \boldsymbol{\lambda}, e) = \int_{t_{min}}^{t_{max}} \rho(\mathbf{x}+\boldsymbol{\lambda})\, \dot{\mathbf{u}}_{\alpha}^{\dagger}(\mathbf{x}+\boldsymbol{\lambda}, t, e) \cdot \dot{\mathbf{u}}_{\beta}^{\dagger}(\mathbf{x}-\boldsymbol{\lambda}, t, e)\, \mathrm{d}t, \tag{4.2}$$

where $\dot{\mathbf{u}}_{\alpha}^{\dagger}(\mathbf{x}, t, e)$ and $\dot{\mathbf{u}}_{\beta}^{\dagger}(\mathbf{x}, t, e)$ approximately represent P- and S-wave particle velocity fields where the † symbol denotes adjoint; $\boldsymbol{\lambda} = (\lambda_x, \lambda_y, \lambda_z)$ is the vector space-lag extension (Sava and Vasconcelos, 2011); and e is the event index. The extended imaging condition is described in a generic form and reduces to the zero-lag imaging condition when

$(\lambda_x, \lambda_y, \lambda_z) = (0, 0, 0)$ m. Due to the unknown source origin time, the imaging condition involves a summation over time to marginalize the temporal dependence. While equation 4.2 is specific for computing PS crosscorrelation zero-lag and extended images; it can also be used to generate zero-lag PP and SS autocorrelation images $\Big($i.e,. $I_{\alpha\alpha}(\mathbf{x}, e)$ and $I_{\beta\beta}(\mathbf{x}, e)\Big)$ by calculating the dot product of the corresponding adjoint particle velocity field with itself and summing over time.

To attenuate imaging artifacts (i.e., nonphysical fake modes generated due to incomplete acquisition of stress components in the injected data and/or truncation wavefronts that are correlated with the true wave modes (Rocha et al., 2019; Yan and Sava, 2008)) that arise due to elastic time-reversal wavefield extrapolation, we apply the imaging condition within a time window $t = [t_{min}, t_{max}]$ that is narrower than the original data window $t = [0, T]$ (Oren and Shragge, 2021a). Therefore, the integral evaluation in equation 4.2 in practice starts from a maximum time ($t_{max} < T$ s) and progresses in reverse time back to a minimum time ($t_{min} \geq$ 0 s) using the adjoint isotropic EWE operator. Finally, this imaging condition precludes the costly wave-mode decomposition during backpropagation, which offers an advantage over its crosscorrelation counterpart outlined in Shabelansky et al. (2015). In the elastic TRI procedure, we first compute the zero-lag PP, SS, and PS image volumes using the current velocity models for each event. Because the zero-lag PS image produces higher resolution results compared to its autocorrelation counterparts, we base our event location estimates on the spatial location of maximum absolute amplitude of the PS image. The TRI process is finalized by computing the extended image at the estimated event location. We exclude the negative values in the extended images, which degrade the image residuals as well as the gradient computation procedure in practical implementations.

4.2.2 Step 3: Image-domain residuals and objective function evaluation

For the inversion procedure, we define our multiterm objective function $\mathcal{J}$ over all selected events to be minimized as

$$\mathcal{J} = \frac{1}{2} \sum_e \int \Big[\epsilon_1 \int_{-\boldsymbol{\lambda}}^{\boldsymbol{\lambda}} P_\lambda^2(\boldsymbol{\lambda})\, I_{\alpha\beta}^2(\mathbf{x}, \boldsymbol{\lambda}, e)\, \mathrm{d}\boldsymbol{\lambda} + P_{\alpha\beta}^2(\mathbf{x}, e) \Big(\epsilon_2\, I_{\alpha\alpha}^2(\mathbf{x}, e) + \epsilon_3\, I_{\beta\beta}^2(\mathbf{x}, e) \Big) \Big] \mathrm{d}\mathbf{x}, \quad (4.3)$$

where ϵ_1, ϵ_2, and ϵ_3 are scalar weights that determine the relative contribution of each term in the objective function, and $P_\lambda(\boldsymbol{\lambda})$ and $P_{\alpha\beta}(\mathbf{x}, e)$ are to-be-specified extended and zero-lag image-domain penalty operators. These operators are designed to respectively annihilate the focal energy at and about zero lag and at the estimated event location; whatever energy remains is considered to be the image-domain residual. A number of different extended penalty operators have been proposed to serve this purpose (Díaz and Sava, 2017; Shragge et al., 2013; Yang and Sava, 2015), but herein we use a Gaussian function centered at zero lag to penalize the extended image volumes:

$$P_\lambda(\boldsymbol{\lambda}) = 1 - \exp\left(-\frac{\lambda_x^2}{2\sigma_x^2} - \frac{\lambda_y^2}{2\sigma_y^2} - \frac{\lambda_z^2}{2\sigma_z^2} \right), \quad (4.4)$$

where $\boldsymbol{\sigma} = (\sigma_x, \sigma_y, \sigma_z)$ controls the variances of the Gaussian function in the shift dimensions. Because $I_{\alpha\beta}(\mathbf{x}, e)$ produces the highest resolution among all the zero-lag images due to the P and S wavefields backpropagating at different velocities and coexisting over a narrower zone in space and time, we create the zero-lag penalty operator $P_{\alpha\beta}(\mathbf{x}, e)$ based upon $I_{\alpha\beta}(\mathbf{x}, e)$ to measure the inconsistency in the zero-lag autocorrelation images (Shragge et al., 2013):

$$P_{\alpha\beta}(\mathbf{x}, e) = \operatorname{sech}\left[\frac{w\, I_{\alpha\beta}(\mathbf{x}, e)}{\max\big(I_{\alpha\beta}(\mathbf{x}, e)\big)} \right], \quad (4.5)$$

where w is a dimensionless parameter used to adjust the penalty width. This multiplicative penalty operator removes the maximum focal energy where the PS and PP or SS zero-lag images are consistent, and tends to unity elsewhere. The energy remaining in the penalized images forms the zero-lag image-domain residuals.

4.2.3 Steps 4 & 5: Adjoint-state variables and gradient computation

We calculate the gradients (sensitivity kernels) of the objective function in equation 4.3 with respect to model parameters $\hat{\alpha}$ and $\hat{\beta}$ (see equation 4.1) by using the perturbation theory with the goal of obtaining an expression like

$$\delta \mathcal{J} = \int \Big(\delta\hat{\alpha}\, \mathcal{K}^{\hat{\alpha}}(\mathbf{x}) + \delta\hat{\beta}\, \mathcal{K}^{\hat{\beta}}(\mathbf{x}) \Big) \mathrm{d}\mathbf{x}, \tag{4.6}$$

where $\mathcal{K}^{\hat{\alpha}}(\mathbf{x})$ and $\mathcal{K}^{\hat{\beta}}(\mathbf{x})$ are the gradients of the objective function, which is perturbed with respect to the model parameters $\hat{\alpha}$ and $\hat{\beta}$, respectively. Following the adjoint-state method (Plessix, 2006), we obtain the gradient terms as

$$\mathcal{K}^{\hat{\alpha}}(\mathbf{x}) = -\sum_{e} \int_0^T \mathbf{u}^{\dagger}_{\alpha}(\mathbf{x}, t, e) \cdot \boldsymbol{v}^{\alpha}(\mathbf{x}, t, e)\, \mathrm{d}t \tag{4.7}$$

and

$$\mathcal{K}^{\hat{\beta}}(\mathbf{x}) = \sum_{e} \int_0^T \mathbf{u}^{\dagger}_{\beta}(\mathbf{x}, t, e) \cdot \boldsymbol{v}^{\beta}(\mathbf{x}, t, e)\, \mathrm{d}t, \tag{4.8}$$

where $\boldsymbol{v}^{\alpha}(\mathbf{x}, t, e)$ and $\boldsymbol{v}^{\beta}(\mathbf{x}, t, e)$ denote the P- and S-wave adjoint-state variables, respectively. As seen in equations 4.7 and 4.8, the gradients are computed by correlating the state and adjoint-state variables that are calculated using the forward propagation of an adjoint source, which is a function of backpropagated P- and S-wavefield energy and the penalized zero-lag and extended images. Appendix A presents the full derivation and definitions of the adjoint-state variables as well as the gradient terms. In practice, after calculating the individual gradients for each event, we apply illumination compensation (Warner et al., 2013; Yang et al., 2013) leading to more accurate results by reducing the artifacts at and around source locations. This approach requires dividing the gradient by a stabilized measure of the total adjoint-state wavefield energy. This procedure is followed by the application of a smoothing operator in both vertical and horizontal directions to the individual gradients, which are then summed over the selected events.

4.2.4 Steps 6 & 7: Step length determination and velocity model updating

After calculating the gradients, we determine the final step length through a multiparameter line-search approach (Tang and Ayeni, 2015) based on the gradient-descent optimization scheme (Nocedal and Wright, 2006). We first search for individual P- and S-wave step lengths and then perform a second line search along a 2D vector whose components are defined by the determined individual P- and S-wave step lengths (Witten and Shragge, 2017a). We then scale the negative of gradients by the final step length to determine the magnitude of the update and add it to the current velocity model:

$$m_{i+1}^{k} = m_{i}^{k} - h_i\,\mathcal{K}_i^k, \quad k = \hat{\alpha}, \hat{\beta}, \tag{4.9}$$

where m is the velocity model, h is the step length, and i is the iteration number. We iterate the given steps until reaching convergence or meeting a stopping criterion. In the ensuing numerical experiments, we stop the inversion procedure when the gradient of the objective function becomes zero or turns positive.

4.3 Numerical Experiments

This section describes two synthetic numerical experiments that illustrate the ability of the developed method to reconstruct velocity models leading to improved location estimates. The first numerical experiment presents a 2D example, in which we use elastic velocity models consisting of a smooth 1D gradient background with Gaussian low and high velocity anomalies that represent the inversion targets. The second experiment presents a more realistic example that includes complex 3D subsurface models with sparse acquisition geometry. In our experiments, we model microseismic sources using an Ormsby wavelet specified by the four corner frequencies $[f_1, f_2, f_3, f_4] = [2, 3, 20, 25]$ Hz (experiment 1) and a 15 Hz Ricker wavelet (experiment 2) with events characterized by a moment-tensor stress-source mechanism. In forward modeling, we use a graphics processing unit (GPU)-based finite-difference time-domain (FDTD) solver with the second-order temporal and eighth-order spatial accuracy stencil (Weiss and Shragge, 2013). Our numerical simulations use boundary conditions comprised of two cascading operators: the absorbing boundary conditions derived from a one-way wave equation (Clayton and Enquist, 1977) and an exponential-damping sponge layer (Cerjan et al., 1985) with no free-surface boundary condition applied.

Using the true velocity models, we first forward model synthetic elastic multicomponent microseismic data. We run separate simulations to generate the events using double-couple sources (e.g., non-zero stress components of m_{xx}=−1 and m_{zz}=1) excited at various depths. Prior to imaging, we separate the direct P- and S-wave arrivals by applying hyperbolic mute functions to the data (Oren and Shragge, 2021a). We then individually image all events by following the elastic TRI strategy (equation 4.2) using the inaccurate initial velocity models. This step is followed by calculating the model gradients for each event and stacking over all sources to obtain the final results (equations 4.7 and 4.8). Finally, using the iterative approach described above, we update the velocity models, which are then used in the TRI procedure to obtain enhanced event locations. To stabilize the gradient computation and balance the resolution of the resulting gradients, we apply a low-pass filter below 9 Hz and 6 Hz to the P- and S-wave mode data, respectively, prior to the forward and adjoint wavefield propagations.

4.3.1 Experiment 1: Gradient background model

In the first numerical experiment, we illustrate our method using the P- and S-wave velocity models shown in Figure 4.1. The models share the same kinematics and include smooth background P- and S-wave velocities ($V_P(z) = 3 + z/2$ km/s and $V_S(z) = \sqrt{3} + z/2$ km/s shown in Figure 4.1c and Figure 4.1d) along with two Gaussian low and high velocity variations with maximum and minimum perturbations of $\Delta V_P = \Delta V_S = \pm 0.3\,$km/s visible in Figure 4.1a and Figure 4.1b. We also use a constant density model of $\rho = 2.0\,$g/cm^3. The numerical setup consists of a computational domain of dimension $[N_x, N_z] = [608, 224]$, $N_t = 5001$ time steps, temporal and spatial sampling intervals of $\Delta t = 0.5\,$ms and $\Delta x = \Delta z = 0.01$ km, respectively. The simulated data are recorded at multicomponent (vertical and horizontal motions) receivers placed on the surface at each computation grid point

($\Delta r = 0.01\,\mathrm{km}$).

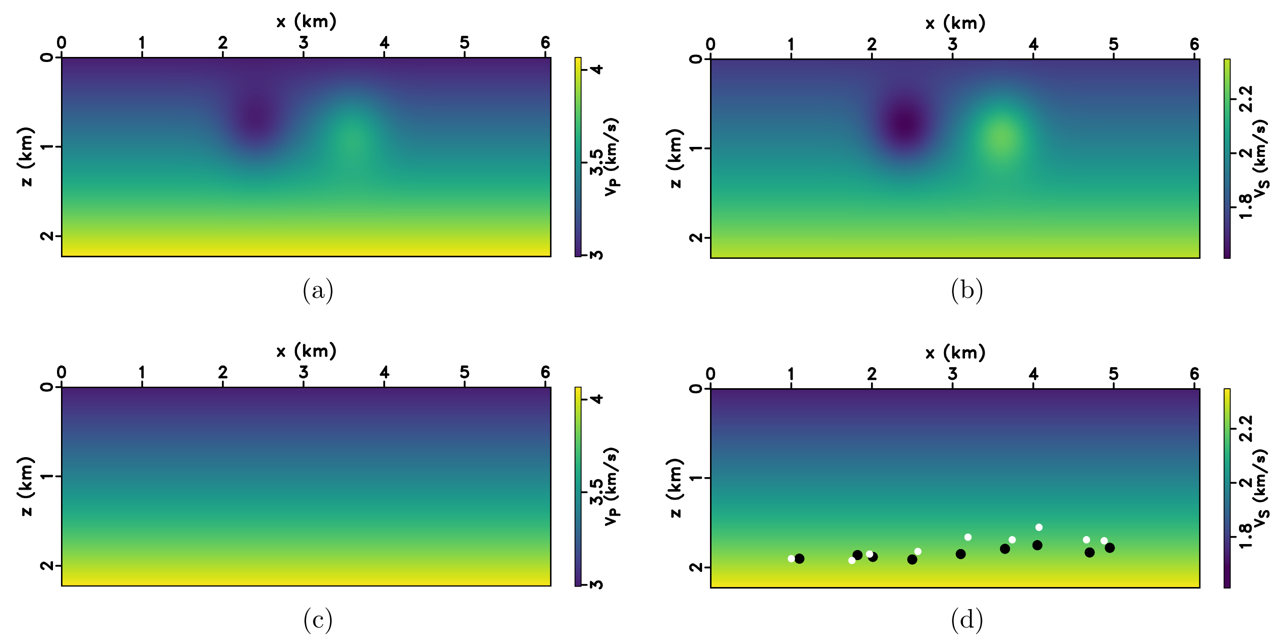

Figure 4.1 True (a) P- and (b) S-wave velocity models with two Gaussian anomalies in homogeneous background gradients. Background (c) V_P and (d) V_S model overlain with the true (black dots) and initial estimated (white dots) event locations.

Figure 4.2a and Figure 4.2b respectively displays the vertical and horizontal components of the surface-recorded 2D elastic data simulated from a single event at $[x, z] = [2.50, 1.91]$ km using the true velocity models in Figure 4.1. To enhance the S/N of the imaging condition results, we apply a mask around the direct P- and S-wave arrivals in the data domain prior to injection. The wave-mode separation procedure (completed using hyperbolic mute operators) is repeated for all events. This operation is followed by the individual backpropagation of the separated wave modes (Figure 4.2c and Figure 4.2d) using the EWE operator (Step 1), and evaluating the imaging condition in equation 4.2 (Step 2).

As shown in Figure 4.1c and Figure 4.1d, we generate the initial velocity models by simply removing the two Gaussian anomalies from the background linear gradient trends. This experiment uses nine irregularly distributed microseismic sources centered about 1.85 km depth, the true locations of which are denoted by black dots in Figure 4.1d. Using the initial models, we construct the zero-lag images for each event to estimate the event locations as the maximum value in each image. To attenuate the imaging artifacts discussed in the previous section, we generate the zero-lag images computed in the time window $[t_{min}, t_{max}] = [0, 0.4]$ s, which is designed through trial and error based on evaluating the quality of the artifact reduction.

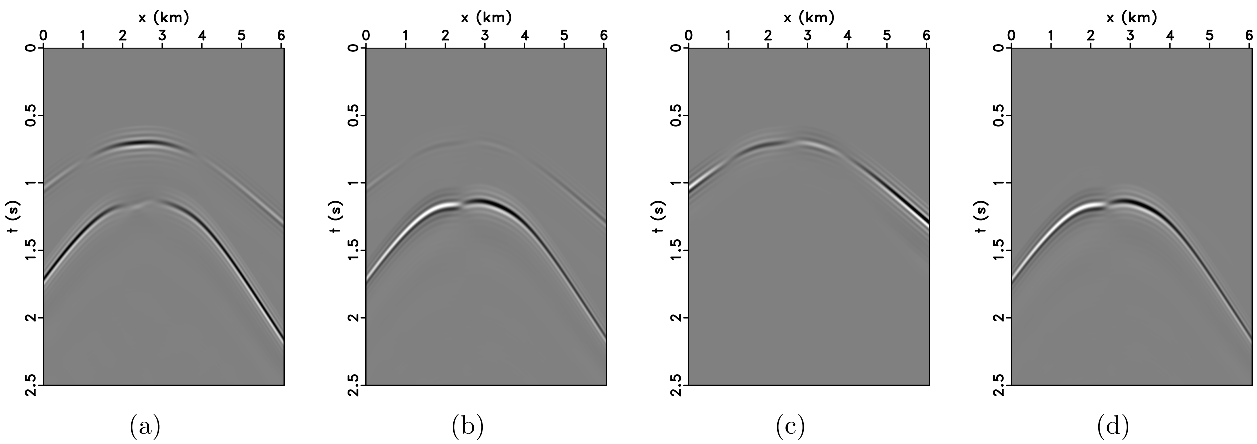

Figure 4.2 Simulated (a) u_z and (b) u_x components of 2D microseismic data associated with a single event located at $[x, z] = [2.50, 1.91]$ km computed using the true velocity models in Figure 4.1. (c) P- and (d) S-wave modes in the u_x component separated in the data domain using hyperbolic time muting. Although not shown here, the corresponding wave modes in the u_z component are similarly separated.

Figure 4.3a and Figure 4.3b respectively shows the zero-lag images calculated using the true and initial velocity models for the multicomponent data shown in Figure 4.2. The energy (red dot) in Figure 4.3a is collapsed at the true source location (larger green dot), which is expected when imaging with the correct velocity models, whereas Figure 4.3b shows a focus (smaller red dot) smeared due to the inaccurate imaging velocities. We also compute the corresponding extended images constructed for $[\,|\lambda_x|, |\lambda_z|\,] \leq 0.2$ km at the estimated event locations (i.e., maximum amplitude points) in the zero-lag images (Figure 4.3a and Figure 4.3b) using the true and background velocity models for evaluating their sensitivity to velocity inaccuracy. As observed in Figure 4.3c, the extended image is well-focused around zero lag due to the correct velocities while the extended image in Figure 4.3d exhibits energy shifted away from zero lag due to the inaccurate velocities. The extended image in Figure 4.3d also reveals the directions of the required velocity updates. Moreover, the event locations estimated from the zero-lag images generated using the initial models are shown as white dots in Figure 4.1d, and have a mean spatial root-mean-square (RMS) error of 128 m.

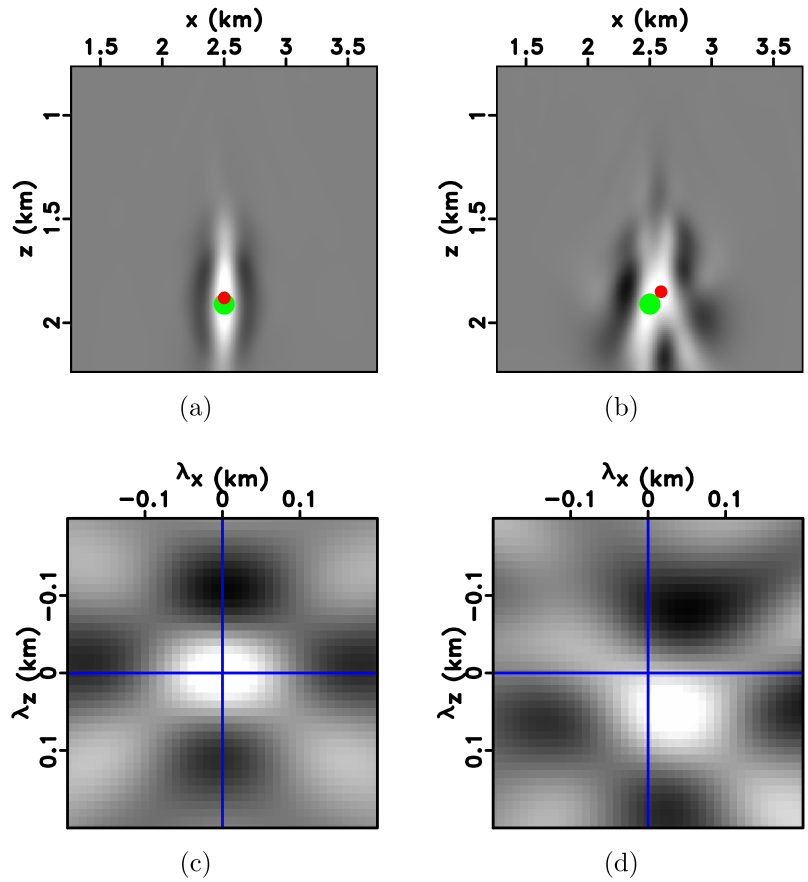

Figure 4.3 (a)-(b) Zero-lag and (c)-(d) space-lag extended images computed using the true (left column) and background (right column) velocity models. The larger green and smaller red dots respectively denote the true and estimated source locations. The blue crosshairs in the extended images highlight the zero lag. Extended images are evaluated only at the estimated source locations, which correspond to the zero-lag image maxima indicated by the red dots.

For the inversion parameterization, we choose the weight parameters that adjust the contribution of each term in the objective function as $[\epsilon_1, \epsilon_2, \epsilon_3] = [1.0, 0.01, 0.0001]$; the broadness of the zero-lag and extended penalty functions that effectively remove the well-focused energy in the images are $w = 5.0$ and $[\sigma_x, \sigma_z] = [0.05, 0.05]$, respectively, determined through trial and error. The values for ϵ_2 and ϵ_3 balance the influence of the zero-lag terms as well as decrease their contributions one order of magnitude compared to the extended term, whose optimization is the primary focus of the inversion procedure due to its highest velocity sensitivity amongst the images. Moreover, because the magnitude of the backpropagated S wavefield $\dot{\mathbf{u}}_\beta^\dagger$ is typically higher than that of the P wavefield $\dot{\mathbf{u}}_\alpha^\dagger$, we downweight the image $I_{\beta\beta}$ more strongly to equalize their relative energy in the waveform.

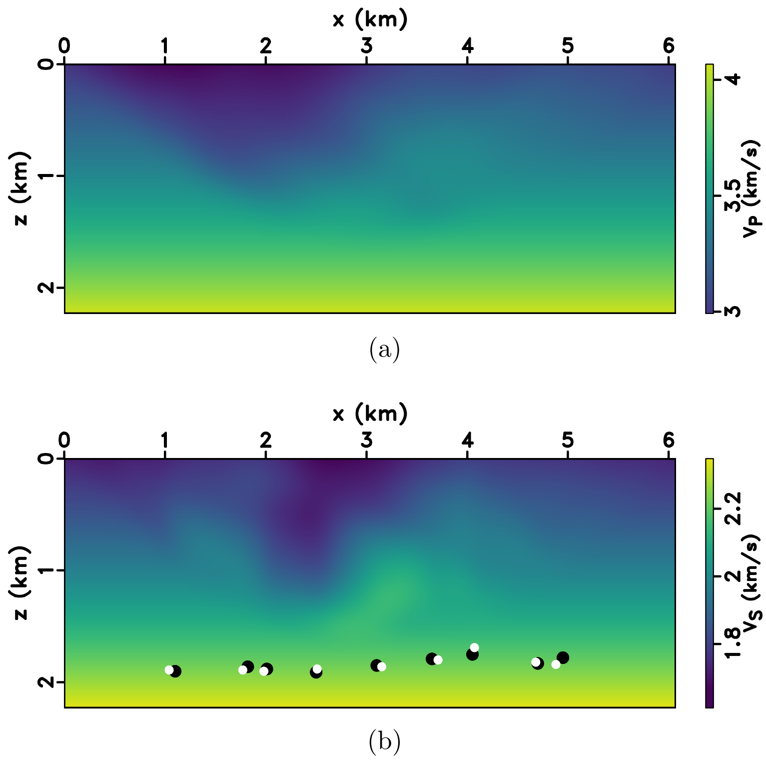

Figure 4.4 Inverted (a) V_P and (b) V_S model overlain with the true (black dots) and final estimated (white dots) event locations.

Figure 4.4 depicts the V_P and V_S velocity models recovered after 12 iterations of the adjoint-state tomography framework described above. Both the inverted V_P and V_S models show the target Gaussian perturbations with different spatial resolutions. Considering the shorter wavelength of S waves relative to P waves, the inverted V_S model typically features a higher-resolution recovery compared to the inverted V_P model. The inversion results also show that the velocity updates are quite smooth due to the low spatial wavenumbers of the images and forward-scattering nature of the microseismic direct-wave image-domain tomography problem. The white dots in Figure 4.4b indicate the imaged event locations obtained using the inverted models, which are now closer to the true event locations denoted by the black dots. Figure 4.5 shows the zero-lag and extended images computed using the inverted models for the multicomponent data shown in Figure 4.2. When compared with the initial imaging results shown in Figure 4.3b and Figure 4.3d, the optimized zero-lag image is better focused and at the correct location while the extended image exhibits energy more tightly focused around zero lag. Finally, Figure 4.6 presents a crossplot between the initial and final RMS location errors for all events. The dashed line implies no change in location, while points falling below or above the dashed line indicate decrease or increase in location errors, respectively. These results demonstrate that the inversion procedure has reasonably improved the event location estimates and has reduced the average spatial RMS error from 128 m to 52 m or about a 60% reduction in misposition error.

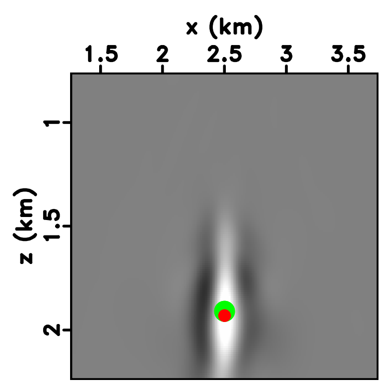

(a)

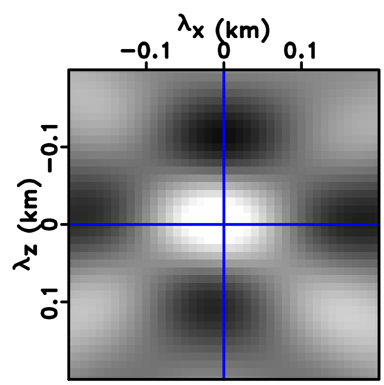

(b)

Figure 4.5 (a) Zero-lag and (b) space-lag extended images computed using the recovered velocity models. The green and red dots respectively show the true and estimated source locations. The extended image is calculated only at the estimated source location, which corresponds to the zero-lag image maximum indicated by the red dot. Note how the image focusing in (a) is improved and the energy in (b) is shifted towards zero lag after using the inverted models compared to the imaging results (Figure 4.3b and Figure 4.3d) obtained using the initial models.

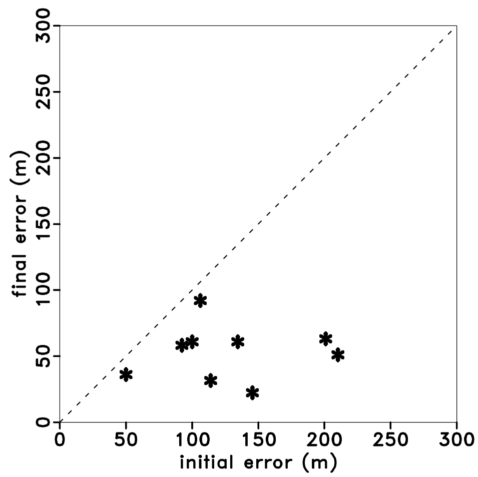

Figure 4.6 Crossplot of the initial and final RMS location errors of nine forward-modeled events. Points falling along the dashed line indicates no change in error whereas those below the line indicate improved event location estimates. The results show an approximately 60% decrease in location errors on average over all events.

4.3.2 Experiment 2: SEG/EAGE 3D Overthrust model

The second numerical experiment applies our proposed inversion method to a more complex velocity model – SEG/EAGE 3D Overthrust model (Aminzadeh et al., 1994) displayed in Figure 4.7a. Because the original 3D Overthrust model includes only the P-wave velocity, we define an S-wave velocity model by assuming an oscillatory PS velocity ratio as a function of depth (Figure 4.7b) as well as an accompanying density model (not shown) that ranges between $\rho = 2.0 - 3.0\,\mathrm{g/cm^3}$. We place 12 microseismic events (larger blue dots in Figure 4.7c) with an irregular distribution at depths ranging between $z = 2.40$ km and $z = 2.55$ km. Our surface receiver geometry is extracted from a field experiment (Witten and Shragge, 2017b) and consists of 192 non-uniformly distributed three-component (3C) receivers (smaller red dots in Figure 4.7c) covering an approximately $3.0 \times 3.0\ \mathrm{km}^2$ area. Using the true models for each event, we forward model synthetic elastic 3C microseismic data using a 3D computational domain of dimension $[N_x, N_y, N_z] = [140, 140, 140]$, $N_t = 2100$ time steps, temporal and spatial sampling intervals of $\Delta t = 1\,\mathrm{ms}$, and $\Delta x = \Delta y = \Delta z = 0.025\,\mathrm{km}$.

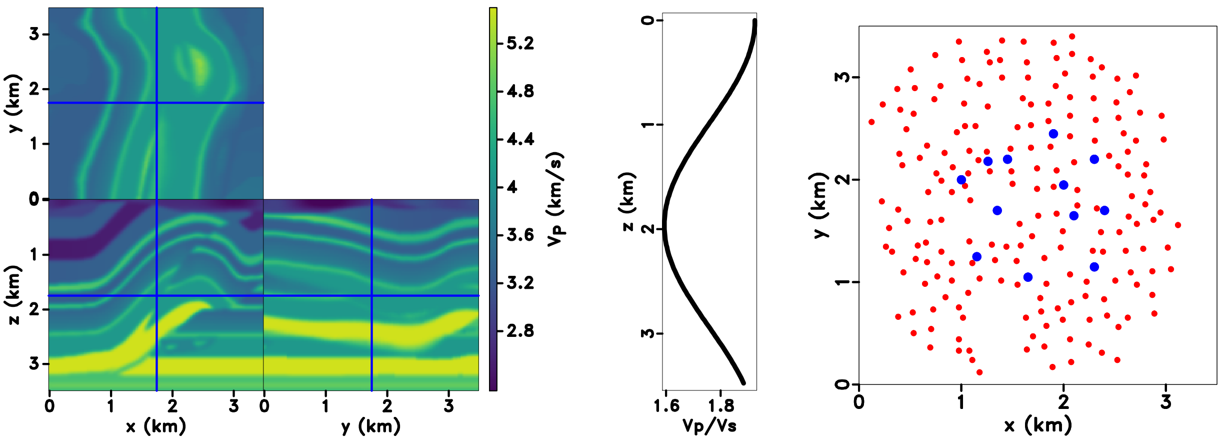

(a) (b) (c)

Figure 4.7 (a) True P-wave velocity from the 3D Overthrust model and (b) V_P/V_S ratio used to generate the true S-wave velocity model. (c) Illustration of source and receiver geometry employed in the 3D inversion experiment. The larger blue dots indicate the projected source coordinates while the smaller red dots indicate the locations of the 3C receivers deployed at the surface.

Our initial model building strategy follows a scenario where we heavily smooth the true V_P model along all the spatial axes to generate an initial V_P model as shown in Figure 4.8a. Using this information, we also assume an erroneous V_P/V_S ratio of $\sqrt{3}$ when constructing the initial V_S model. Figure 4.8b and Figure 4.8c respectively depicts the true percentage V_P and V_S model perturbations (i.e., the difference between the true and initial models), which are the targets of the inversion process.

Following a similar strategy to the previous 2D inversion experiment, we choose ϵ_i values as $[\epsilon_1, \epsilon_2, \epsilon_3] = [1.0, 0.001, 0.0001]$ to favor the optimization of the extended term while balancing the relative contributions of the zero-lag terms in the objective function. Moreover, through trial and error, we select the zero-lag and extended penalty parameterizations to be $w = 5.0$ and $[\sigma_x, \sigma_y, \sigma_z] = [0.1, 0.1, 0.1]$, respectively, to adequately penalize the well-focused energy in images.

Figure 4.9 shows the inverted V_P and V_S models as well as the percentage velocity change after applying ten iterations of the proposed tomography formalism. Most of the update is applied to increase the velocities in both models and corresponds to the smooth part of the high-velocity thrust structure present in the true models. The V_S model updates appear to be more significant compared to those in the V_P model likely due to our double-couple stress-source mechanism radiating stronger S-wave energy that dominates the resulting imaged events (Oren and Shragge, 2021a). Furthermore, because of the events that are relatively deep (i.e., $z = 2.40 - 2.55$ km) compared to the array width and are laterally restricted in the model, the updates are likely affected by this narrow aperture angle between sources and receivers.

Figure 4.10a displays a stacked bar graph including the normalized objective function along with the contributions of each term. The total convergence curve exhibits a reduction of $\sim 60\%$ after ten iterations, beyond which point it becomes flat and little-to-no improvement is achieved in the model updates. We observe that the largest improvement comes from the extended image $I_{\alpha\beta}$ (term 1) with a reduction of $\sim 65\%$ whereas the zero-lag images $I_{\alpha\alpha}$ and $I_{\beta\beta}$ (terms 2 and 3) exhibits a reduction of $\sim 15\%$ and $\sim 45\%$, respectively. Figure 4.10b shows a crossplot of the initial and final RMS location errors calculated based upon the maximum amplitude of the $I_{\alpha\beta}$ images for all sources. We observe a considerable decrease ($\sim 60\%$) in error with the events plotting closer to the horizontal axis.

The zero-lag and extended images constructed using the initial, inverted, and true V_P and V_S models are displayed in Figure 4.11 where the crosshairs in the zero-lag panels indicate the true location of a single event at $[x, y, z] = [1.26, 2.18, 2.47]$ km. We construct the zero-lag images in the time window $[t_{min}, t_{max}] = [0, 0.3]$ s to suppress the imaging artifacts and evaluate the extended image gathers for $[\,|\lambda_x|, |\lambda_y|, |\lambda_z|\,] \leq 0.25$ km. Comparing these results, we note defocused energy in the initial image shifted away from the correct event location, whereas the final image exhibits relatively better focused energy with a positive peak amplitude as shown in white centralized around the true location, which is a similar pattern to the image obtained with the true models. Similarly, the final extended image volume extracted at the maximum location of the relative zero-lag image exhibits a lower degree of moveout pattern in comparison with the initial extended imaging result.

4.4 Discussion

The proposed inversion methodology is typically less prone to the well-known cycle-skipping problem of FWI, but generally produces lower-resolution inversion results relative to FWI (Shabelansky et al., 2015; Witten and Shragge, 2017a). However, our inversion results demonstrate that generating model updates that exhibit relatively lower resolution can still produce sufficiently accurate event locations. Additionally, because stacking-based migration methods enhance the S/N of microseismic data, image-domain inversion generally does not suffer from low S/N data as severely as data-domain methods. We also point out that windowing about arrivals tends to increase the S/N of injected data; however, we caution that narrow windowing, if inappropriately applied, can remove weak signals for low S/N scenarios.

The proposed inversion approach can be extended to anisotropic media by incorporating the potential wavefield energy term in the PS energy imaging condition as described by Oren and Shragge (2021b). Perturbing the stiffness tensor present in the potential energy term with respect to anisotropy parameters can allow for such an extension. To determine a prospectus for image-domain anisotropic elastic inversion, Oren and Shragge (2021b) present a 3D sensitivity analysis of the PS energy imaging condition to the Thomsen (1986) anisotropy parameters for various transversely isotropic symmetries (e.g., transversely isotropic with a vertical and horizontal symmetry axes as well as orthorhombic). Their analysis demonstrates that the imaged events mostly are affected by errors in ϵ and δ, but show almost no sensitivity to γ for the SEG Advanced Modeling (SEAM) Barrett Unconventional model (Regone et al., 2017).

Because the developed inversion method relies on the forward and adjoint numerical solutions of the EWE for each seismic event, the associated computational cost remains the primary drawback, particularly for 3D applications. Each imaging step requires contemporaneous P- and S-wave propagations to construct zero-lag and extended images. The number of space lags used to build extended images is one of the main factors affecting the computational expense. To increase the computational efficiency, we compute the zero-lag and extended images during a single imaging experiment. We first independently propagate the P and S wavefields backward in time within the original data window (i.e., $t = [0, T]$) to form the zero-lag image between t_{min} and t_{max}, which is then used to extract the maximum amplitude point for extended imaging. This step is followed by propagating the P and S wavefields at $t = 0$ forward in time until $t = t_{max}$ and evaluating the extended imaging condition at the maximum zero-lag image point between t_{min} and t_{max}. By doing so, we avoid two extra P- and S-wave propagations for extended image construction, which represents a substantial increase in efficiency considering the high computational expense of iterative inversion process. The gradient computation requires four elastic propagations (i.e., two backward propagations for calculating P- and S-wave adjoint sources and two forward propagations for calculating P- and S-wave adjoint-state wavefields). The computational cost also depends on the number of spatial locations at which the extended images are calculated for the adjoint source computation (see equations 4.26 and 4.35). For extended image calculation, we use the same number of spatial locations and space lags per event in our numerical experiments. Finally, the 2D step length determination process requires three imaging steps (i.e., six propagations for P- and S-wave data) for each event, but we opt to perform the first objective function evaluation within the first imaging step to reduce this requirement to two imaging steps. Therefore, we must compute ten elastic wavefield propagations for a single iteration, which, for instance, takes approximately two hours for the 12 events in the previously presented 3D synthetic example when using a single device on a NVIDIA V100 GPU card. However, the aforementioned computational cost can be further reduced using a data parallelism or domain-decomposition strategy across multiple GPU nodes.

The image-domain tomography approach presented herein could be applied for a variety of different (time-lapse) monitoring programs (e.g., gas hydrates, geothermal, and CO_2 sequestration projects) (Deichmann and Giardini, 2009; Kim et al., 2018; Kumar et al., 2018) using active-/passive-source vertical seismic profiling (VSP) measurements. The active-source VSP acquisition configuration allows one to exploit the principle of reciprocity by exchanging the locations of sources and receivers to set up a computationally efficient imaging and tomography problem with the sources and receivers located at the borehole and surface, respectively. This configuration mimics a conventional surface microseismic monitoring investigation, which is a very similar scenario to the one we have successfully validated our imaging and inversion algorithms. The proposed inversion method may have practical applications not only in exploration seismology, but also in crustal or earthquake seismology to obtain regional or global tomographic models, which could be helpful to further reduce the uncertainty associated with the Earth's heterogeneous structure and dynamics.

4.5 Conclusions

We develop a semi-automatic adjoint-state wavefield tomography method for multicomponent passive data to jointly reconstruct elastic velocity models. We employ an elastic TRI procedure to generate the microseismic source images, which are used to estimate the event locations. We define a multiterm objective function that optimizes the focusing of different types of event images. We conduct 2D and 3D synthetic numerical experiments that gradually present more complex models along with more realistic source and receiver configurations. The numerical experiments show that one can generate accurate elastic models that result in location errors considerably reduced relative to the initial model estimates. In addition to microseismic monitoring, the proposed inversion technique could be applied in other fields including regional/global-scale seismology as well as gas hydrates, geothermal, and CO_2 sequestration monitoring projects.

4.6 Acknowledgments

We thank B. Witten and C. Finger for their comments, which improved the quality of the manuscript. We acknowledge the Center for Wave Phenomena (CWP) consortium sponsors for their financial support. The reproducible numerical examples in this paper were

generated using the Madagascar software package using the Wendian HPC systems made available through the Colorado School of Mines.

4.7 Appendix A - Gradient derivation

To derive the P- and S-wave model gradients $\mathcal{K}^{\hat{\alpha}}(\mathbf{x})$ and $\mathcal{K}^{\hat{\beta}}(\mathbf{x})$ in equations 4.7 and 4.8, we perturb each term in the objective function (equation 4.3) with respect to the image for a single event e. We separately present the derivations for the extended and zero-lag terms of the objective functional in the subsections below.

4.7.1 Term 1: Extended image

We introduce $\mathcal{J}_1$ as the extended term of equation 4.3

$$\mathcal{J}_1 = \frac{\epsilon_1}{2} \iint P_\lambda^2(\boldsymbol{\lambda})\, I_{\alpha\beta}^2(\mathbf{x}, \boldsymbol{\lambda})\, \mathrm{d}\boldsymbol{\lambda}\, \mathrm{d}\mathbf{x}, \tag{4.10}$$

and perturb equation 4.10 with respect to the state variables $\mathbf{u}_\alpha^\dagger$ and $\mathbf{u}_\beta^\dagger$ to obtain

$$\delta\mathcal{J}_1 = \epsilon_1 \iint \delta I_{\alpha\beta}(\mathbf{x}, \boldsymbol{\lambda})\, R(\mathbf{x}, \boldsymbol{\lambda})\, \mathrm{d}\boldsymbol{\lambda}\, \mathrm{d}\mathbf{x}, \tag{4.11}$$

where $R(\mathbf{x}, \boldsymbol{\lambda}) = P_\lambda^2(\boldsymbol{\lambda})\, I_{\alpha\beta}(\mathbf{x}, \boldsymbol{\lambda})$ and

$$\delta I_{\alpha\beta}(\mathbf{x}, \boldsymbol{\lambda}) = \int \rho(\mathbf{x}+\boldsymbol{\lambda}) \Big(\delta\dot{\mathbf{u}}_\alpha^\dagger(\mathbf{x}+\boldsymbol{\lambda}, t) \cdot \dot{\mathbf{u}}_\beta^\dagger(\mathbf{x}-\boldsymbol{\lambda}, t) + \dot{\mathbf{u}}_\alpha^\dagger(\mathbf{x}+\boldsymbol{\lambda}, t) \cdot \delta\dot{\mathbf{u}}_\beta^\dagger(\mathbf{x}-\boldsymbol{\lambda}, t) \Big) \mathrm{d}t. \tag{4.12}$$

Substituting equation 4.12 into equation 4.11 obtains

$$\delta\mathcal{J}_1 := \delta\mathcal{J}_1^{\hat{\alpha}} + \delta\mathcal{J}_1^{\hat{\beta}}, \tag{4.13}$$

where

$$\delta\mathcal{J}_1^{\hat{\alpha}} := \epsilon_1 \iiint \Big(\rho(\mathbf{x}+\boldsymbol{\lambda})\, \delta\dot{\mathbf{u}}_\alpha^\dagger(\mathbf{x}+\boldsymbol{\lambda}, t) \cdot \dot{\mathbf{u}}_\beta^\dagger(\mathbf{x}-\boldsymbol{\lambda}, t)\, R(\mathbf{x}, \boldsymbol{\lambda}) \Big) \mathrm{d}t\, \mathrm{d}\boldsymbol{\lambda}\, \mathrm{d}\mathbf{x} \tag{4.14}$$

and

$$\delta\mathcal{J}_1^{\hat{\beta}} := \epsilon_1 \iiint \Big(\rho(\mathbf{x}+\boldsymbol{\lambda})\, \dot{\mathbf{u}}_\alpha^\dagger(\mathbf{x}+\boldsymbol{\lambda}, t) \cdot \delta\dot{\mathbf{u}}_\beta^\dagger(\mathbf{x}-\boldsymbol{\lambda}, t)\, R(\mathbf{x}, \boldsymbol{\lambda}) \Big) \mathrm{d}t\, \mathrm{d}\boldsymbol{\lambda}\, \mathrm{d}\mathbf{x}. \tag{4.15}$$

To find $\delta\dot{\mathbf{u}}_\alpha^\dagger$ and $\delta\dot{\mathbf{u}}_\beta^\dagger$ in equations 4.14 and 4.15, we rewrite the isotropic EWE (equation 4.1) using linear operator notation (Shabelansky et al., 2015):

$$\mathcal{L}^\dagger\,\mathbf{u}_\alpha^\dagger = \mathbf{d}_\alpha, \tag{4.16}$$

where $\mathbf{d}_\alpha$ is the separated P-wave data vector and $\mathcal{L}^\dagger$ is the adjoint isotropic EWE operator:

$$\mathcal{L}^\dagger = \hat{\alpha}\,\nabla\nabla\cdot - \,\hat{\beta}\,\nabla\times\nabla\times - \,\partial_{tt}. \tag{4.17}$$

We perturb equation 4.16 with respect to the model parameter $\hat{\alpha}$ and obtain

$$\delta\mathcal{L}^\dagger\,\mathbf{u}_\alpha^\dagger + \mathcal{L}^\dagger\,\delta\mathbf{u}_\alpha^\dagger = 0, \tag{4.18}$$

and solve for $\delta\mathbf{u}_\alpha^\dagger$

$$\delta\mathbf{u}_\alpha^\dagger = -(\mathcal{L}^\dagger)^{-1}\delta\mathcal{L}^\dagger\,\mathbf{u}_\alpha^\dagger, \tag{4.19}$$

where

$$\delta\mathcal{L}^\dagger = \delta\hat{\alpha}\,\nabla\nabla\cdot - \,\delta\hat{\beta}\,\nabla\times\nabla\times\,. \tag{4.20}$$

Introducing $\delta\mathcal{L}^\dagger$ into equation 4.19 yields

$$\delta\mathbf{u}_\alpha^\dagger = -(\mathcal{L}^\dagger)^{-1}(\delta\hat{\alpha}\,\nabla\nabla\cdot - \,\delta\hat{\beta}\,\nabla\times\nabla\times)\,\mathbf{u}_\alpha^\dagger. \tag{4.21}$$

Because the adjoint displacement vector field $\mathbf{u}_\alpha^\dagger$ is curl-free in isotropic elastic media and if we take the first-order time derivative of each side, equation 4.21 becomes

$$\delta\dot{\mathbf{u}}_\alpha^\dagger = -\partial_t\Big((\mathcal{L}^\dagger)^{-1}\delta\hat{\alpha}\,\nabla\nabla\cdot\mathbf{u}_\alpha^\dagger\Big). \tag{4.22}$$

If we substitute this expression into equation 4.14

$$\delta\mathcal{J}_1^{\hat{\alpha}} = -\,\epsilon_1\iiint\rho(\mathbf{x}+\boldsymbol{\lambda})\,\partial_t\Big((\mathcal{L}^\dagger)^{-1}\delta\hat{\alpha}\,\nabla\nabla\cdot\mathbf{u}_\alpha^\dagger(\mathbf{x}+\boldsymbol{\lambda},t)\Big)\cdot\dot{\mathbf{u}}_\beta^\dagger(\mathbf{x}-\boldsymbol{\lambda},t)\,R(\mathbf{x},\boldsymbol{\lambda})\mathrm{d}t\,\mathrm{d}\boldsymbol{\lambda}\,\mathrm{d}\mathbf{x}. \tag{4.23}$$

We recognize an inner product and rearrange the integral in equation 4.23 using the inner product rule $\Big[$i.e., $\Big\langle\,\rho\;\partial_t\,(\mathcal{L}^\dagger)^{-1}\,\nabla\nabla\cdot\mathbf{u}_\alpha^\dagger\,,\;\dot{\mathbf{u}}_\beta^\dagger\,R\Big\rangle = \Big\langle\,\mathbf{u}_\alpha^\dagger\,,\;\nabla\nabla\cdot\mathcal{L}^{-1}\,\partial_t\,\rho\,\dot{\mathbf{u}}_\beta^\dagger\,R\Big\rangle\,\Big]$ to remove the operator dependence on $\delta\hat{\alpha}$ (Shabelansky et al., 2015; Witten and Shragge, 2017a):

$$\delta\mathcal{J}_1^{\hat{\alpha}} = -\,\epsilon_1 \int\!\delta\hat{\alpha} \iint\!\mathbf{u}_\alpha^\dagger(\mathbf{x}+\boldsymbol{\lambda},t)\cdot\Big(\nabla\nabla\cdot\mathcal{L}^{-1}\rho(\mathbf{x}+\boldsymbol{\lambda})\,\ddot{\mathbf{u}}_\beta^\dagger(\mathbf{x}-\boldsymbol{\lambda},t)\,R(\mathbf{x},\boldsymbol{\lambda})\,\mathrm{d}\boldsymbol{\lambda}\Big)\mathrm{d}t\,\mathrm{d}\mathbf{x}, \quad (4.24)$$

where $\mathcal{L}^{-1}$ is the inverse of the forward isotropic EWE operator. To further simplify the calculation of equation 4.24, we apply a shift in the spatial coordinates (Shen and Symes, 2008) and rearrange the terms as the following:

$$\begin{aligned}
\delta\mathcal{J}_1^{\hat{\alpha}} &= -\,\epsilon_1 \int\!\delta\hat{\alpha} \int\!\mathbf{u}_\alpha^\dagger(\mathbf{x},t)\cdot\Big(\nabla\nabla\cdot\mathcal{L}^{-1}\int\!\rho(\mathbf{x})\,\ddot{\mathbf{u}}_\beta^\dagger(\mathbf{x}-2\boldsymbol{\lambda},t)\,R(\mathbf{x}-\boldsymbol{\lambda},\boldsymbol{\lambda})\,\mathrm{d}\boldsymbol{\lambda}\Big)\mathrm{d}t\,\mathrm{d}\mathbf{x} \\
&= -\,\epsilon_1 \int\!\delta\hat{\alpha} \int\!\mathbf{u}_\alpha^\dagger(\mathbf{x},t)\cdot\boldsymbol{\upsilon}_1^\alpha(\mathbf{x},t)\,\mathrm{d}t\,\mathrm{d}\mathbf{x} \qquad (4.25)\\
&= \int\!\delta\hat{\alpha}\,\mathcal{K}_1^{\hat{\alpha}}(\mathbf{x})\,\mathrm{d}\mathbf{x},
\end{aligned}$$

where

$$\boldsymbol{\upsilon}_1^\alpha(\mathbf{x},t) = \epsilon_1\,\nabla\nabla\cdot\mathcal{L}^{-1}\int\!\rho(\mathbf{x})\;\ddot{\mathbf{u}}_\beta^\dagger(\mathbf{x}-2\boldsymbol{\lambda},t)\,R(\mathbf{x}-\boldsymbol{\lambda},\boldsymbol{\lambda})\,\mathrm{d}\boldsymbol{\lambda}, \quad (4.26)$$

is the P-wave adjoint wavefield.

The spatial shift that we apply to the residual extended image $R(\mathbf{x},\boldsymbol{\lambda})$ suggests that we compute numerous extended images in the vicinity of the estimated event location $\mathbf{x}$, which are then used in the calculation of the adjoint source $\boldsymbol{\upsilon}_1^\alpha(\mathbf{x},t)$.

Similarly, we rewrite the isotropic EWE (equation 4.1) using linear operator notation to find $\dot{\mathbf{u}}_\beta^\dagger$ in equation 4.15:

$$\mathcal{L}^\dagger\,\mathbf{u}_\beta^\dagger = \mathbf{d}_\beta, \quad (4.27)$$

where $\mathbf{d}_\beta$ is the separated S-wave data vector. We perturb equation 4.27 with respect to the model parameter $\hat{\beta}$ and obtain

$$\delta\mathcal{L}^\dagger\,\mathbf{u}_\beta^\dagger + \mathcal{L}^\dagger\,\delta\mathbf{u}_\beta^\dagger = 0, \quad (4.28)$$

and solve for $\delta\mathbf{u}_\beta^\dagger$

$$\delta\mathbf{u}_\beta^\dagger = -(\mathcal{L}^\dagger)^{-1}\delta\mathcal{L}^\dagger\,\mathbf{u}_\beta^\dagger. \quad (4.29)$$

Introducing $\delta\mathcal{L}^\dagger$ in equation 4.20 into equation 4.29 obtains

$$\delta\mathbf{u}^\dagger_\beta = -(\mathcal{L}^\dagger)^{-1}(\delta\hat{\alpha}\,\nabla\nabla\cdot - \,\delta\hat{\beta}\,\nabla\times\nabla\times)\,\mathbf{u}^\dagger_\beta. \tag{4.30}$$

Because the adjoint S wavefield $\mathbf{u}^\dagger_\beta$ is divergence-free in isotropic elastic media, if we take the first-order time derivative of each side equation 4.30 becomes

$$\delta\dot{\mathbf{u}}^\dagger_\beta = \partial_t\Big((\mathcal{L}^\dagger)^{-1}\delta\hat{\beta}\,\nabla\times\nabla\times\,\mathbf{u}^\dagger_\beta\Big). \tag{4.31}$$

Substituting this expression into equation 4.15 gives

$$\delta\mathcal{J}_1^{\hat{\beta}} = \,\epsilon_1\iiint\Big(\rho(\mathbf{x}+\boldsymbol{\lambda})\,\dot{\mathbf{u}}^\dagger_\alpha(\mathbf{x}+\boldsymbol{\lambda},t)\cdot\partial_t\Big((\mathcal{L}^\dagger)^{-1}\delta\hat{\beta}\,\nabla\times\nabla\times\,\mathbf{u}^\dagger_\beta(\mathbf{x}-\boldsymbol{\lambda},t)\Big)\,R(\mathbf{x},\boldsymbol{\lambda})\Big)\mathrm{d}t\,\mathrm{d}\boldsymbol{\lambda}\,\mathrm{d}\mathbf{x}. \tag{4.32}$$

Using the inner product rule, we remove the operator dependence on $\delta\hat{\beta}$:

$$\delta\mathcal{J}_1^{\hat{\beta}} = \,\epsilon_1\iiint\Big(\nabla\times\nabla\times\mathcal{L}^{-1}\rho(\mathbf{x}+\boldsymbol{\lambda})\,\ddot{\mathbf{u}}^\dagger_\alpha(\mathbf{x}+\boldsymbol{\lambda},t)\cdot\delta\hat{\beta}\,\mathbf{u}^\dagger_\beta(\mathbf{x}-\boldsymbol{\lambda},t)\,R(\mathbf{x},\boldsymbol{\lambda})\Big)\mathrm{d}t\,\mathrm{d}\boldsymbol{\lambda}\,\mathrm{d}\mathbf{x}. \tag{4.33}$$

To further simplify the calculation of equation 4.33, we similarly apply a shift in the spatial coordinates and rearrange the terms as the following:

$$\begin{aligned}
\delta\mathcal{J}_1^{\hat{\beta}} &= \epsilon_1\iint\Big(\nabla\times\nabla\times\mathcal{L}^{-1}\int\rho(\mathbf{x}+2\boldsymbol{\lambda})\,\ddot{\mathbf{u}}^\dagger_\alpha(\mathbf{x}+2\boldsymbol{\lambda},t)R(\mathbf{x}+\boldsymbol{\lambda},\boldsymbol{\lambda})\,\mathrm{d}\boldsymbol{\lambda}\Big)\cdot\delta\hat{\beta}\,\mathbf{u}^\dagger_\beta(\mathbf{x},t)\mathrm{d}t\,\mathrm{d}\mathbf{x}\\
&= \epsilon_1\int\delta\hat{\beta}\int\mathbf{u}^\dagger_\beta(\mathbf{x},t)\cdot\boldsymbol{v}_1^\beta(\mathbf{x},t)\,\mathrm{d}t\,\mathrm{d}\mathbf{x} \qquad (4.34)\\
&= \int\delta\hat{\beta}\,\mathcal{K}_1^{\hat{\beta}}(\mathbf{x})\,\mathrm{d}\mathbf{x},
\end{aligned}$$

where

$$\boldsymbol{v}_1^\beta(\mathbf{x},t) = \epsilon_1\,\nabla\times\nabla\times\mathcal{L}^{-1}\int\rho(\mathbf{x}+2\boldsymbol{\lambda})\;\ddot{\mathbf{u}}^\dagger_\alpha(\mathbf{x}+2\boldsymbol{\lambda},t)\,R(\mathbf{x}+\boldsymbol{\lambda},\boldsymbol{\lambda})\,\mathrm{d}\boldsymbol{\lambda}, \tag{4.35}$$

is the S-wave adjoint wavefield.

4.7.2 Terms 2 and 3: Zero-lag autocorrelation images penalized by crosscorrelation image

We derive the adjoint-state variables for the zero-lag autocorrelation images $I_{\alpha\alpha}(\mathbf{x})$ and $I_{\beta\beta}(\mathbf{x})$ penalized by the zero-lag crosscorrelation image $I_{\alpha\beta}(\mathbf{x})$ by perturbing

$$\mathcal{J}_2 = \frac{\epsilon_2}{2} \int P^2_{\alpha\beta}(\mathbf{x})\, I^2_{\alpha\alpha}(\mathbf{x})\mathrm{d}\mathbf{x}, \tag{4.36}$$

to obtain

$$\delta\mathcal{J}_2 = \epsilon_2 \int \Big(P^2_{\alpha\beta}(\mathbf{x})\, I_{\alpha\alpha}(\mathbf{x})\, \delta I_{\alpha\alpha}(\mathbf{x}) + P_{\alpha\beta}(\mathbf{x})\, \delta P_{\alpha\beta}(\mathbf{x})\, I^2_{\alpha\alpha}(\mathbf{x}) \Big)\, \mathrm{d}\mathbf{x}, \tag{4.37}$$

where

$$\delta P_{\alpha\beta}(\mathbf{x}) = -w\, P_{\alpha\beta}(\mathbf{x})\, T_{\alpha\beta}(\mathbf{x})\, \delta I_{\alpha\beta}(\mathbf{x}), \tag{4.38}$$

where $\delta I_{\alpha\beta}(\mathbf{x})$ is defined in equation 4.12 with $(\lambda_x, \lambda_y, \lambda_z) = (0,0,0)$ m, and $T_{\alpha\beta}(\mathbf{x}) = \tanh\big(w\, I_{\alpha\beta}(\mathbf{x})\big)$. Based on the imaging condition in equation 4.2, one can form the PP autocorrelation image using

$$I_{\alpha\alpha}(\mathbf{x}) = \int \rho(\mathbf{x})\, \dot{\mathbf{u}}^\dagger_\alpha(\mathbf{x},t) \cdot \dot{\mathbf{u}}^\dagger_\alpha(\mathbf{x},t)\, \mathrm{d}t, \tag{4.39}$$

to obtain

$$\delta I_{\alpha\alpha}(\mathbf{x}) = 2 \int \rho(\mathbf{x})\, \dot{\mathbf{u}}^\dagger_\alpha(\mathbf{x},t) \cdot \delta\dot{\mathbf{u}}^\dagger_\alpha(\mathbf{x},t)\, \mathrm{d}t. \tag{4.40}$$

If we substitute $\delta P_{\alpha\beta}(\mathbf{x})$ and $\delta I_{\alpha\alpha}(\mathbf{x})$ into equation 4.37, and separate $\mathcal{J}_2$ into component functions $\delta\dot{\mathbf{u}}^\dagger_\alpha(\mathbf{x},t)$ and $\delta\dot{\mathbf{u}}^\dagger_\beta(\mathbf{x},t)$, we find

$$\begin{aligned} \delta\mathcal{J}_2^{\hat{\alpha}} &= 2\,\epsilon_2 \int \Big(P^2_{\alpha\beta}(\mathbf{x})\, I_{\alpha\alpha}(\mathbf{x}) \int \rho(\mathbf{x})\, \dot{\mathbf{u}}^\dagger_\alpha(\mathbf{x},t) \cdot \delta\dot{\mathbf{u}}^\dagger_\alpha(\mathbf{x},t)\, \mathrm{d}t \\ &- w\, P^2_{\alpha\beta}(\mathbf{x})\, T_{\alpha\beta}(\mathbf{x})\, I^2_{\alpha\alpha}(\mathbf{x}) \int \rho(\mathbf{x})\, \delta\dot{\mathbf{u}}^\dagger_\alpha(\mathbf{x},t) \cdot \dot{\mathbf{u}}^\dagger_\beta(\mathbf{x},t)\, \mathrm{d}t \Big)\, \mathrm{d}\mathbf{x}, \end{aligned} \tag{4.41}$$

and

$$\delta\mathcal{J}_2^{\hat{\beta}} = -\,\epsilon_2\, w \int P^2_{\alpha\beta}(\mathbf{x})\, T_{\alpha\beta}(\mathbf{x})\, I^2_{\alpha\alpha}(\mathbf{x}) \int \rho(\mathbf{x})\, \dot{\mathbf{u}}^\dagger_\alpha(\mathbf{x},t) \cdot \delta\dot{\mathbf{u}}^\dagger_\beta(\mathbf{x},t)\, \mathrm{d}t\, \mathrm{d}\mathbf{x}. \tag{4.42}$$

If we substitute $\delta\dot{\mathbf{u}}^{\dagger}_{\alpha}(\mathbf{x},t)$ (equation 4.21) and $\delta\dot{\mathbf{u}}^{\dagger}_{\beta}(\mathbf{x},t)$ (equation 4.31) into equations 4.41 and 4.42 and rearrange the terms as done in equations 4.26 and 4.35, we find

$$\begin{aligned} \delta\mathcal{J}_2^{\hat{\alpha}} &= \epsilon_2 \int \delta\hat{\alpha} \int \mathbf{u}^{\dagger}_{\alpha}(\mathbf{x},t)\cdot\boldsymbol{v}^{\alpha}_2(\mathbf{x},t)\,\mathrm{d}t\,\mathrm{d}\mathbf{x} \\ &= \int \delta\hat{\alpha}\,\mathcal{K}^{\hat{\alpha}}_2(\mathbf{x})\,\mathrm{d}\mathbf{x}, \end{aligned} \tag{4.43}$$

and

$$\begin{aligned} \delta\mathcal{J}_2^{\hat{\beta}} &= \epsilon_2 \int \delta\hat{\beta} \int \mathbf{u}^{\dagger}_{\beta}(\mathbf{x},t)\cdot\boldsymbol{v}^{\beta}_2(\mathbf{x},t)\,\mathrm{d}t\,\mathrm{d}\mathbf{x} \\ &= \int \delta\hat{\beta}\,\mathcal{K}^{\hat{\beta}}_2(\mathbf{x})\,\mathrm{d}\mathbf{x}, \end{aligned} \tag{4.44}$$

where the adjoint-state variable contributions for this term are as the following:

$$\begin{aligned} \boldsymbol{v}^{\hat{\alpha}}_2(\mathbf{x},t) &= \epsilon_2\,\nabla\nabla\cdot\mathcal{L}^{-1}\Big(-2\,P^2_{\alpha\beta}(\mathbf{x})\,I_{\alpha\alpha}(\mathbf{x})\,\rho(\mathbf{x})\int\ddot{\mathbf{u}}^{\dagger}_{\alpha}(\mathbf{x},t)\,\mathrm{d}t \\ &+ w\,P^2_{\alpha\beta}(\mathbf{x})\,T_{\alpha\beta}(\mathbf{x})\,I^2_{\alpha\alpha}(\mathbf{x})\,\rho(\mathbf{x})\int\ddot{\mathbf{u}}^{\dagger}_{\beta}(\mathbf{x},t)\,\mathrm{d}t\Big), \end{aligned} \tag{4.45}$$

and

$$\boldsymbol{v}^{\hat{\beta}}_2(\mathbf{x},t) = -\epsilon_2\,w\,\nabla\times\nabla\times\mathcal{L}^{-1}\Big(P^2_{\alpha\beta}(\mathbf{x})\,T_{\alpha\beta}(\mathbf{x})\,I^2_{\alpha\alpha}(\mathbf{x})\,\rho(\mathbf{x})\int\ddot{\mathbf{u}}^{\dagger}_{\alpha}(\mathbf{x},t)\,\mathrm{d}t\Big). \tag{4.46}$$

Following a similar strategy used in the derivation for term 2, we find the expressions for term 3 $\left(\mathcal{J}_3 = \frac{\epsilon_3}{2}\int P^2_{\alpha\beta}(\mathbf{x})\,I^2_{\beta\beta}(\mathbf{x})\mathrm{d}\mathbf{x}\right)$ to be

$$\begin{aligned} \delta\mathcal{J}_3^{\hat{\alpha}} &= \epsilon_3 \int \delta\hat{\alpha} \int \mathbf{u}^{\dagger}_{\alpha}(\mathbf{x},t)\cdot\boldsymbol{v}^{\alpha}_3(\mathbf{x},t)\,\mathrm{d}t\,\mathrm{d}\mathbf{x} \\ &= \int \delta\hat{\alpha}\,\mathcal{K}^{\hat{\alpha}}_3(\mathbf{x})\,\mathrm{d}\mathbf{x}, \end{aligned} \tag{4.47}$$

and

$$
\begin{aligned}
\delta\mathcal{J}_3^{\hat\beta} &= \epsilon_3 \int \delta\hat\beta \int \mathbf{u}_\beta^\dagger(\mathbf{x},t)\cdot \boldsymbol{v}_3^\beta(\mathbf{x},t)\,\mathrm{d}t\,\mathrm{d}\mathbf{x} \\
&= \int \delta\hat\beta\,\mathcal{K}_3^{\hat\beta}(\mathbf{x})\,\mathrm{d}\mathbf{x},
\end{aligned}
\tag{4.48}
$$

where the adjoint-state variables are defined as

$$
\boldsymbol{v}_3^{\hat\alpha}(\mathbf{x},t) = \epsilon_3\, w\, \nabla\nabla\cdot\mathcal{L}^{-1}\Big(P_{\alpha\beta}^2(\mathbf{x})\, T_{\alpha\beta}(\mathbf{x})\, I_{\beta\beta}^2(\mathbf{x})\,\rho(\mathbf{x})\int \ddot{\mathbf{u}}_\beta^\dagger(\mathbf{x},t)\,\mathrm{d}t\Big),
\tag{4.49}
$$

and

$$
\begin{aligned}
\boldsymbol{v}_3^{\hat\beta}(\mathbf{x},t) &= \epsilon_3\, \nabla\times\nabla\times\mathcal{L}^{-1}\Big(2\, P_{\alpha\beta}^2(\mathbf{x})\, I_{\beta\beta}(\mathbf{x})\,\rho(\mathbf{x})\int \ddot{\mathbf{u}}_\beta^\dagger(\mathbf{x},t)\,\mathrm{d}t \\
&- w\, P_{\alpha\beta}^2(\mathbf{x})\, T_{\alpha\beta}(\mathbf{x})\, I_{\beta\beta}^2(\mathbf{x})\,\rho(\mathbf{x})\int \ddot{\mathbf{u}}_\alpha^\dagger(\mathbf{x},t)\,\mathrm{d}t\Big).
\end{aligned}
\tag{4.50}
$$

4.7.3 Total gradient

We form the total perturbation of the objective functional using the terms above

$$
\delta\mathcal{J} = \delta\mathcal{J}^{\hat\alpha} + \delta\mathcal{J}^{\hat\beta},
\tag{4.51}
$$

where

$$
\begin{aligned}
\delta\mathcal{J}^{\hat\alpha} &= \int \delta\hat\alpha\,\mathcal{K}^{\hat\alpha}(\mathbf{x})\,\mathrm{d}\mathbf{x} \\
&= \int \delta\hat\alpha \int \mathbf{u}_\alpha^\dagger(\mathbf{x},t)\cdot\sum_{i=1}^{3}\boldsymbol{v}_i^\alpha(\mathbf{x},t)\,\mathrm{d}t\,\mathrm{d}\mathbf{x},
\end{aligned}
\tag{4.52}
$$

and

$$
\begin{aligned}
\delta\mathcal{J}^{\hat\beta} &= \int \delta\hat\beta\,\mathcal{K}^{\hat\beta}(\mathbf{x})\,\mathrm{d}\mathbf{x} \\
&= \int \delta\hat\beta \int \mathbf{u}_\beta^\dagger(\mathbf{x},t)\cdot\sum_{i=1}^{3}\boldsymbol{v}_i^\beta(\mathbf{x},t)\,\mathrm{d}t\,\mathrm{d}\mathbf{x},
\end{aligned}
\tag{4.53}
$$

where $\boldsymbol{v}^\alpha(\mathbf{x},t)$ and $\boldsymbol{v}^\beta(\mathbf{x},t)$ are the adjoint-state variables constructed by forward propagating the summation of the individual adjoint sources derived in the previous subsections. For consistency, we inject the final adjoint source within the same time window $t = [t_{min}, t_{max}]$ as used in the imaging condition. The final adjoint-state variables in equations 4.52 and 4.53 can be written as

$$
\begin{aligned}
\boldsymbol{\upsilon}^{\alpha}(\mathbf{x},t) &= \nabla\nabla\cdot\mathcal{L}^{-1}\Bigg[\epsilon_1 \int \rho(\mathbf{x})\ \ddot{\mathbf{u}}^{\dagger}_{\beta}(\mathbf{x}-2\boldsymbol{\lambda},t)\,R(\mathbf{x}-\boldsymbol{\lambda},\boldsymbol{\lambda})\,\mathrm{d}\boldsymbol{\lambda} \\
&+ \epsilon_2\Big(-2\,P^2_{\alpha\beta}(\mathbf{x})\,I_{\alpha\alpha}(\mathbf{x})\,\rho(\mathbf{x})\int \ddot{\mathbf{u}}^{\dagger}_{\alpha}(\mathbf{x},t)\,\mathrm{d}t + w\,P^2_{\alpha\beta}(\mathbf{x})\,T_{\alpha\beta}(\mathbf{x})\,I^2_{\alpha\alpha}(\mathbf{x})\,\rho(\mathbf{x})\int \ddot{\mathbf{u}}^{\dagger}_{\beta}(\mathbf{x},t)\,\mathrm{d}t\Big) \\
&+ \epsilon_3\,w\,P^2_{\alpha\beta}(\mathbf{x})\,T_{\alpha\beta}(\mathbf{x})\,I^2_{\beta\beta}(\mathbf{x})\,\rho(\mathbf{x})\int \ddot{\mathbf{u}}^{\dagger}_{\beta}(\mathbf{x},t)\,\mathrm{d}t\Bigg], \qquad (4.54)
\end{aligned}
$$

and

$$
\begin{aligned}
\boldsymbol{\upsilon}^{\beta}(\mathbf{x},t) &= \nabla\times\nabla\times\mathcal{L}^{-1}\Bigg[\epsilon_1 \int \rho(\mathbf{x}+2\boldsymbol{\lambda})\ \ddot{\mathbf{u}}^{\dagger}_{\alpha}(\mathbf{x}+2\boldsymbol{\lambda},t)\,R(\mathbf{x}+\boldsymbol{\lambda},\boldsymbol{\lambda})\,\mathrm{d}\boldsymbol{\lambda} \\
&- \epsilon_2\,w\,P^2_{\alpha\beta}(\mathbf{x})\,T_{\alpha\beta}(\mathbf{x})\,I^2_{\alpha\alpha}(\mathbf{x})\,\rho(\mathbf{x})\int \ddot{\mathbf{u}}^{\dagger}_{\alpha}(\mathbf{x},t)\,\mathrm{d}t \qquad (4.55) \\
&+ \epsilon_3\Big(2\,P^2_{\alpha\beta}(\mathbf{x})\,I_{\beta\beta}(\mathbf{x})\,\rho(\mathbf{x})\int \ddot{\mathbf{u}}^{\dagger}_{\beta}(\mathbf{x},t)\,\mathrm{d}t - w\,P^2_{\alpha\beta}(\mathbf{x})\,T_{\alpha\beta}(\mathbf{x})\,I^2_{\beta\beta}(\mathbf{x})\,\rho(\mathbf{x})\int \ddot{\mathbf{u}}^{\dagger}_{\alpha}(\mathbf{x},t)\,\mathrm{d}t\Big)\Bigg].
\end{aligned}
$$

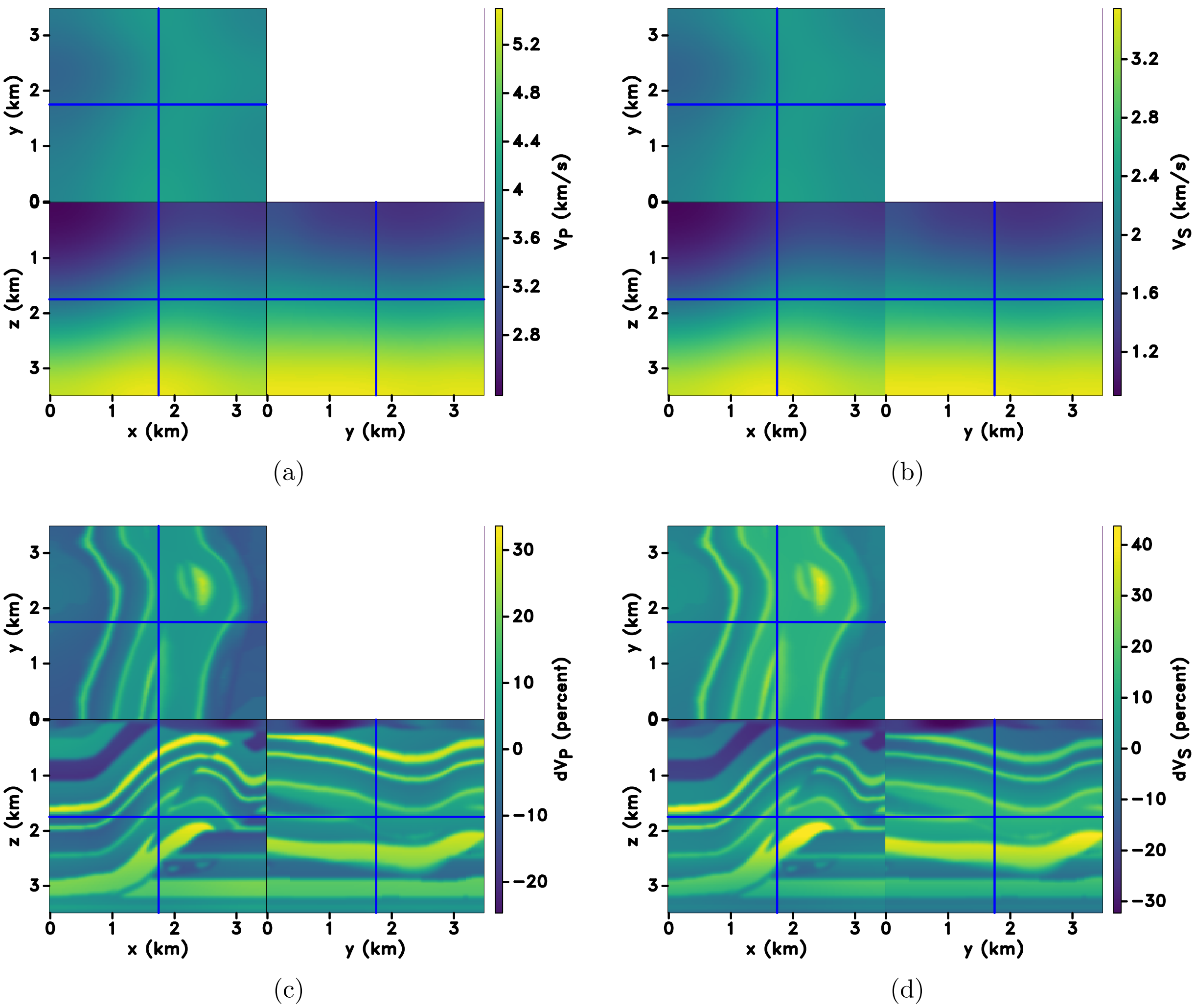

Figure 4.8 Initial (a) V_P and (b) V_S models along with the true model perturbations for the (c) V_P and (d) V_S models, which are the targets of the inversion. The initial V_S model in (b) is constructed by assuming $V_S = V_P/\sqrt{3}$.

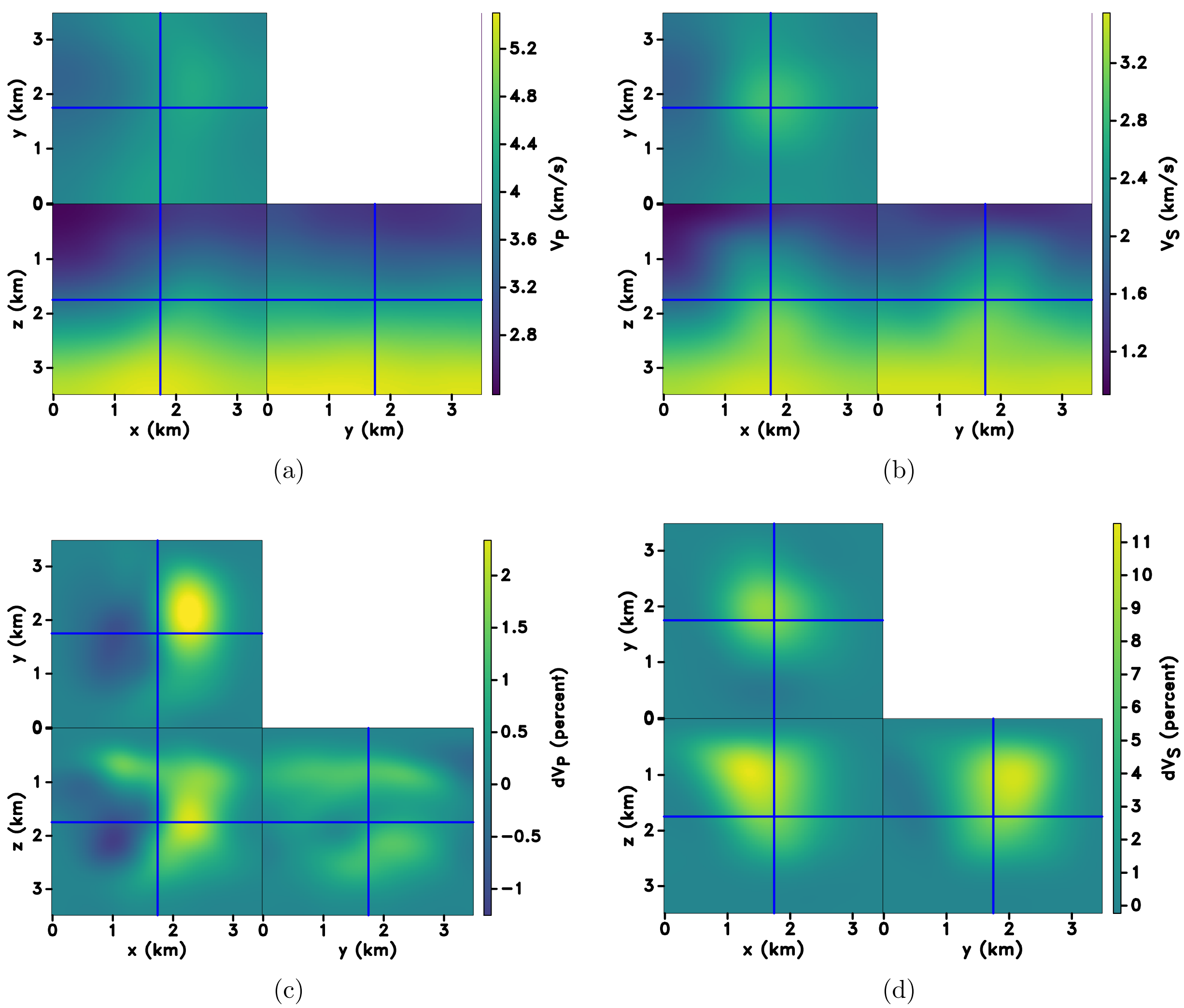

Figure 4.9 Inverted (a) V_P and (b) V_S models, which exhibit the main high-velocity thrust structure. Percentage change in the (a) V_P and (b) V_S models from the inversion procedure.

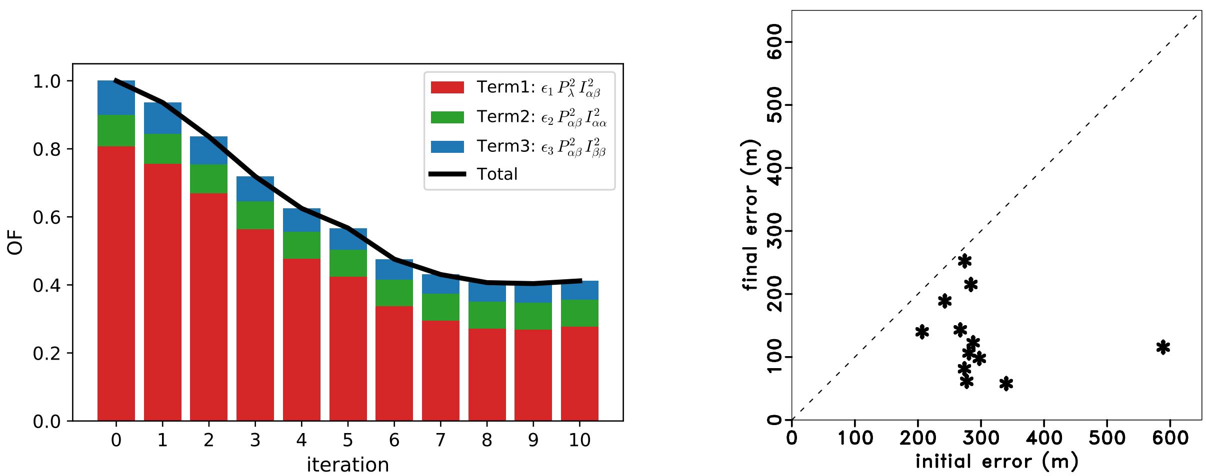

(a) (b)

Figure 4.10 (a) Normalized objective function as a stacked bar graph of each term in equation 4.3 and (b) crossplot of the initial and final RMS location errors of 12 forward-modeled events.

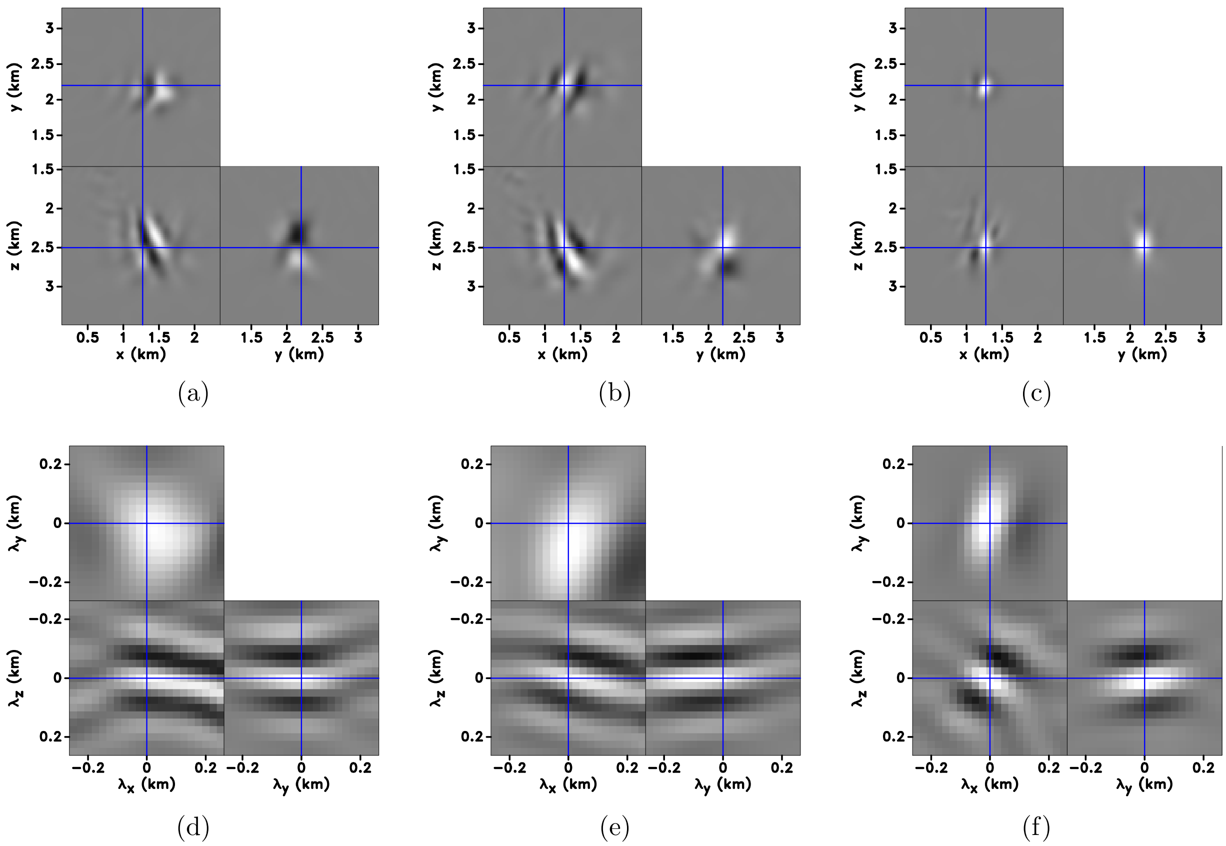

Figure 4.11 Close-up zero-lag image volumes associated with a single event located at $[x, y, z] = [1.26, 2.18, 2.47]$ km computed using the (a) initial, (b) recovered, and (c) true models. The blue crosshairs in the zero-lag images denote the true source location. Note how the maximum positive image amplitude shown in white in (b) gets closer to the true event location. The extended image volumes extracted at the corresponding zero-lag image maxima calculated with the (d) initial, (e) recovered, and (f) true models. Note how the final extended image in (e) shows less moveout relative to (d).

CHAPTER 5

3D IMAGE-DOMAIN DAS-VSP ELASTIC TRANSMISSION TOMOGRAPHY

A paper submitted to *Geophysical Journal International*

Can Oren[1,2,3], Jeffrey Shragge[3]

Full-wavefield elastic imaging of active-source seismic data acquired by downhole receivers commonly offers higher-resolution subsurface images in the vicinity of a borehole compared to conventional surface seismic data sets, which can lack higher-frequency wavefield components due to longer travel paths and increased attenuation. An increasingly used approach for downhole acquisition is vertical seismic profiling (VSP), which has become more attractive when coupled with distributed acoustic sensing (DAS) using optical fibers installed in wells. The main difficulty for generating high-quality images with full-wavefield imaging tools for DAS VSP data, though, is the need for an accurate velocity model. To build plausible velocity models using active-source DAS VSP data, we adopt a 3D image-domain elastic transmission tomography technique, originally developed for surface-recorded passive (microseismic) data, by exchanging the source and receiver positions (i.e., reciprocity) to mimic a passive-seismic surface monitoring scenario. The inversion approach exploits various images for each source constructed through time-reverse imaging (TRI) of downgoing P- and S-wave first-arrival waveforms. The TRI process uses the kinetic term of the (extended) PS energy imaging condition that exhibits sufficient sensitivity to velocity model errors. The method automatically updates the P- and S-wave velocity models to optimize image focusing via adjoint-state inversion. We illustrate the efficacy of the adopted elastic inversion technique using an active-source DAS 3D VSP field data set acquired in the North

[1]Primary researcher and author.
[2]Author for correspondence
[3]Graduate student and Associate Professor, respectively, Center for Wave Phenomena, Colorado School of Mines, Golden, Colorado, USA.

Slope of Alaska. The numerical experiments demonstrate that the inverted velocity models improve the quality of subsurface images constructed through full-wavefield elastic reverse time migration algorithms.

5.1 Introduction

Building accurate velocity models is a key step for successfully imaging the Earth's interior. Unlike ray-based methods (Bishop et al., 1985; Cervenỳ, 2001), velocity analysis tools based on wavefield solutions of governing wave equations can exploit the full waveform and bandwidth of seismic data as well as more accurately handle wave propagation in complex geologic settings. Therefore, the associated full-wavefield tomographic approaches usually provide robust solutions in the velocity updating process, as has been demonstrated in numerous fields including exploration seismology (Pratt, 1999; Tarantola, 1984), global seismology (Bozdağ et al., 2016), near-surface geophysics (Liu et al., 2020), medical imaging (Guasch et al., 2020), and even planetary research (Sava and Asphaug, 2018).

Wavefield tomography represents a class of velocity estimation techniques that can be formulated either in the data (Mora, 1988; Pratt, 1999; Sirgue and Pratt, 2004; Tarantola, 1984; Virieux and Operto, 2009) or the image (Albertin et al., 2006; Sava and Biondi, 2004; Shen and Symes, 2008; Symes and Carazzone, 1991; Weibull and Arntsen, 2013) domain. Data-domain methods are commonly referred to as full waveform inversion (FWI), which produces model updates by means of an objective function whose gradient is simply computed by zero-lag crosscorrelation of forward and adjoint wavefields. Though many different residual metrics have been proposed, the adjoint wavefield is typically computed using the data residual, which is commonly defined as the difference between observed and modeled data. Image-domain methods, generally referred to as migration velocity analysis (MVA), rely on the differential semblance optimization (DSO) principle (i.e., wavefields must produce imaged events well-focused at zero lag when extrapolated with the true velocity) (Symes and Carazzone, 1991). MVA uses objective functions that are defined by image residuals constructed with extended image gathers, which can be functions of surface or subsurface offset, reflection angle or spatial/temporal lags (Rickett and Sava, 2002; Sava and Fomel, 2006; Sava and Vasconcelos, 2011).

Each aforementioned method has its own advantages and limitations. While FWI can produce high-resolution velocity models, this approach commonly suffers from the well-known cycle-skipping problem when the forward and adjoint wavefields are significantly out of phase (i.e., the observed and modeled data difference is more than a half cycle) due to inaccurate initial models and/or insufficiently low data frequencies. Thus, there is a strong amplitude fidelity requirement both for measured data as well as modeled wavefield solutions. Although MVA methods generally produce model updates exhibiting lower relative resolution due to the limited spatial frequency of migrated image gathers, they are significantly more immune to cycle-skipping issues (Symes, 2008). Furthermore, achieving image gather flatness/focusing is more straightforward using MVA techniques relative to FWI, wherein matching data-domain amplitudes and phases can be a highly challenging task, particularly for elastic multicomponent or DAS field data implementations.

Extended image gathers have been successfully used in active- and passive-seismic MVA scenarios as a velocity quality-control tool because they are sensitive to velocity errors and hence can be optimized through tomographic velocity updating (Burdick et al., 2013; Oren and Shragge, 2022; Shabelansky et al., 2015; Shen and Symes, 2008; Witten and Shragge, 2017a; Yang and Sava, 2009). Common-image-point (CIP) gathers are a specific type of extended image gathers, and provide efficient solutions through reduced memory requirements for active-source image-domain wavefield tomography (Yang and Sava, 2015). For active-source scenarios, extended CIP gathers are sparsely constructed by correlating temporally and/or spatially shifted source and receiver wavefields along estimated reflection surfaces and thus can be incorporated into a DSO-type objective function for inversion (Díaz and Sava, 2017; Yang and Sava, 2015).

In passive seismology, extended CIP gathers can be constructed via a process called time-reverse imaging (TRI), where one extrapolates the injected transmitted wavefield energy (i.e., the direct P- and/or S-wave data) in reverse time, and applies an imaging condition to form an event image (Witten and Shragge, 2015). A passive-style elastic adjoint-state tomography method can be formulated based upon the TRI approach by optimizing image-space focusing for jointly locating surface-recorded seismic events and inverting for P- and S-wave velocity models (Oren and Shragge, 2020, 2022; Witten and Shragge, 2017a). In passive seismic investigations (e.g., microseismic), extended CIP gathers are typically calculated at the estimated event location to highlight the spatial and temporal consistencies between P and S wavefields and explore the resulting focusing characteristics (Oren and Shragge, 2021a,b; Rocha et al., 2019; Witten and Shragge, 2015). Accurate imaging velocities lead to focused energy in the vicinity of zero lag of extended CIP gathers, whereas inaccurate velocity models result in poorly focused energy away from zero lag.

Another common seismic survey geometry where sources and receivers do not share the same surface is vertical seismic profiling (VSP). Over the past decade, VSP surveying has seen somewhat of a resurgence due to the maturation of distributed acoustic sensing (DAS) technology and the growing importance of seismic monitoring activities (e.g., production monitoring, CO_2 sequestration). Similarly, various DAS applications have gained considerable popularity within subsurface industries especially for (long-term monitoring) VSP surveys due to the flexibility of fiber optic cables deployments, which enable the acquisition of high-quality and low-cost borehole seismic data with dense spatial sampling (i.e., 1.0 m scale) compared to conventional geophone deployments (Mateeva et al., 2013; Mestayer et al., 2011). DAS also has its own set of acquisition challenges including variable fiber-ground coupling, sensitivity to fiber orientation, and the singular component measurements of the full strain-rate tensor. Seismic energy recorded in DAS VSP surveys typically travels shorter paths and thus is subject to reduced wavefield attenuation compared to conventional seismic reflection data. Imaging and inversion applications using such data sets benefit from these advantages when generating complementary higher-resolution near-well images in contrast with surface-recorded geophone acquisition, which can suffer from the presence of complex near-surface velocity variations as well as strong wavefield attenuation. From DAS VSP measurements, several velocity model building approaches have been proposed using traveltime tomography (Li et al., 2015) and (anisotropic, time-lapse) elastic FWI (Egorov et al., 2018a,b; Podgornova et al., 2017).

Considering the aforementioned challenges of the traveltime tomography and FWI approaches, in this study we use the image-domain elastic transmission tomography framework originally proposed by Oren and Shragge (2022) for microseismic scenarios to build plausible elastic velocity models for DAS VSP investigations. To achieve this goal, we exploit the principle of reciprocity by exchanging the locations of sources and receivers to set up a configuration where the sources and receivers are respectively located in the borehole and on the surface. Such a reciprocal geometry mimics a surface microseismic monitoring scenario where one can conveniently apply the aforementioned passive-style image-domain elastic tomography analysis to DAS VSP data. As a result, velocity models constructed with this full-wavefield methodology can be used in acoustic/elastic depth migration algorithms such as reverse time migration (RTM) (Baysal et al., 1983; McMechan, 1983) to generate high-quality subsurface structural images in the vicinity of the borehole.

We begin by reviewing the theoretical characteristics of the TRI approach along with the image-domain adjoint-state elastic tomography framework. Next, we illustrate the effectiveness of the inversion method with a DAS 3D VSP field data experiment from the North Slope of Alaska. The field data results demonstrate that we can reconstruct 3D P- and S-wave velocity models that improve the source image quality and location estimates even when using a limited number of sources in the presence of permafrost and associated complex velocity inversions. We also show that the inverted velocity models lead to elastic RTM images exhibiting highly accurate well-ties with petrophysical log data. The paper concludes with a discussion of the advantages and shortcomings of the presented approach as well as other possible applications.

5.2 Theory

This section outlines the fundamentals of the image-domain elastic transmission tomography framework proposed by Oren and Shragge (2022) that consists of the following steps: (1) source imaging, (2) image-domain residual computation, (3) gradient calculation, (4) step-length determination, and (5) velocity model updating. We briefly discuss each step below.

5.2.1 Elastic wave equation

We consider the isotropic elastic wave equation (EWE) in a source-free unbounded domain:

$$\ddot{\mathbf{u}} = \hat{\alpha}\,\nabla(\nabla\cdot\mathbf{u}) - \hat{\beta}\,\nabla\times(\nabla\times\mathbf{u}), \tag{5.1}$$

where $\mathbf{u}(\mathbf{x},t)$ is the displacement field as a function of space ($\mathbf{x}$) and time (t); model parameters $\hat{\alpha}(\mathbf{x}) = (\lambda+2\mu)/\rho$ and $\hat{\beta}(\mathbf{x}) = \mu/\rho$ are squared P- and S-wave velocities, respectively, where $\lambda(\mathbf{x})$ and $\mu(\mathbf{x})$ are the Lamé parameters and $\rho(\mathbf{x})$ is density; ∇, $\nabla\cdot$, and $\nabla\times$ are the gradient, divergence, and curl operators; and two superscript dots on $\mathbf{u}$ indicate second-order time differentiation. Equation 5.1 assumes slowly varying Lamé parameters such that one can neglect their spatial gradients (Aki and Richards, 2002).

5.2.2 Elastic time-reverse source imaging

We use an elastic TRI procedure that consists of two steps: (1) extrapolating the direct P and S wavefields backward in time using an elastic wave equation; and (2) evaluating an imaging condition. The elastic TRI process requires an upfront direct arrival separation using a mute function in the data domain as proposed by Oren and Shragge (2021a). Following the work of Oren and Shragge (2020, 2021a), we generate zero-lag and extended source images using the following kinetic energy imaging condition:

$$I_{\alpha\beta}(\mathbf{x},\boldsymbol{\lambda},e) = \int_0^{t_{max}} \rho(\mathbf{x}+\boldsymbol{\lambda})\,\dot{\mathbf{u}}_\alpha^\dagger(\mathbf{x}+\boldsymbol{\lambda},t,e)\cdot\dot{\mathbf{u}}_\beta^\dagger(\mathbf{x}-\boldsymbol{\lambda},t,e)\,\mathrm{d}t, \tag{5.2}$$

where $\dot{\mathbf{u}}_\alpha^\dagger(\mathbf{x},t,e)$ and $\dot{\mathbf{u}}_\beta^\dagger(\mathbf{x},t,e)$ denote separated P- and S-wave particle velocities; symbol † represents adjoint; $\boldsymbol{\lambda} = (\lambda_x, \lambda_y, \lambda_z)$ is the vector space-lag extension (Sava and Vasconcelos, 2011); and e is the source index. When $(\lambda_x, \lambda_y, \lambda_z) = (0,0,0)$ m, the extended imaging condition reduces to the conventional zero-lag imaging condition. As indicated by equation 5.2, we apply the imaging condition by starting the integral evaluation from a time (t_{max}) earlier than the original maximum recording time and progressing back to the estimated origin (or earliest) time, which suppresses most of the imaging artifacts arising due to the elastic wavefield extrapolation (Oren and Shragge, 2021a; Rocha et al., 2019; Yan and Sava, 2008). In addition to the PS crosscorrelation zero-lag $I_{\alpha\beta}(\mathbf{x},e)$ and extended image gathers $I_{\alpha\beta}(\mathbf{x},\boldsymbol{\lambda},e)$, equation 5.2 also generates zero-lag PP and SS autocorrelation images, i.e., $I_{\alpha\alpha}(\mathbf{x},e)$ and $I_{\beta\beta}(\mathbf{x},e)$, all of which collectively form the basis of our objective function.

5.2.3 Objective function and image-domain residual computation

Our inversion framework seeks to minimize the following multiterm objective function $\mathcal{J}$ that measures the image incoherency occurring due to inaccurate P- and S-wave imaging velocities:

$$\mathcal{J} = \frac{1}{2}\sum_e \int \Big[\epsilon_1 \int_{-\boldsymbol{\lambda}}^{\boldsymbol{\lambda}} P_\lambda^2(\boldsymbol{\lambda})\, I_{\alpha\beta}^2(\mathbf{x},\boldsymbol{\lambda},e)\,\mathrm{d}\boldsymbol{\lambda} + P_{\alpha\beta}^2(\mathbf{x},e)\Big(\epsilon_2\, I_{\alpha\alpha}^2(\mathbf{x},e) + \epsilon_3\, I_{\beta\beta}^2(\mathbf{x},e)\Big)\Big]\mathrm{d}\mathbf{x}, \tag{5.3}$$

where $P_\lambda(\boldsymbol{\lambda})$ and $P_{\alpha\beta}(\mathbf{x},e)$ are DSO-type extended and zero-lag image-domain penalty functions that penalize the well-focused energy in the vicinity of zero lag and source location, and thus highlight poorly focused (i.e., residual) energy elsewhere caused by model error. The relative importance of each term in the objective function is controlled by the scalar weights $[\epsilon_1, \epsilon_2, \epsilon_3]$.

To penalize the extended image gathers, a multidimensional Gaussian operator centered at zero lag is expressed as

$$P_\lambda(\boldsymbol{\lambda}) = 1 - \exp\Bigg(-\frac{\lambda_x^2}{2\sigma_x^2} - \frac{\lambda_y^2}{2\sigma_y^2} - \frac{\lambda_x^2}{2\sigma_x^2}\Bigg), \tag{5.4}$$

where $\boldsymbol{\sigma} = (\sigma_x, \sigma_y, \sigma_z)$ independently adjusts the width of the Gaussian function along each space-lag direction. Because a central goal is to minimize the inconsistency among the set of three zero-lag images (i.e., PS, PP, and SS), we design a multiplicative zero-lag penalty operator (Shragge et al., 2013):

$$P_{\alpha\beta}(\mathbf{x}, e) = \operatorname{sech}\left[\frac{w\, I_{\alpha\beta}(\mathbf{x}, e)}{\max\big(I_{\alpha\beta}(\mathbf{x}, e)\big)}\right], \tag{5.5}$$

where w is a dimensionless parameter that determines the broadness of the penalty operator, which is generated based on $I_{\alpha\beta}(\mathbf{x}, e)$ and annihilates energy that coexists between the PS, PP and SS zero-lag images. Thus, only inconsistent energy among the respective zero-lag image pairs remains, which we use for gradient calculation as discussed below.

5.2.4 Gradient calculation

We solve the optimization problem given in equation 5.3 by means of the adjoint-state formalism (Plessix, 2006), which allows us to compute the P- and S-wave velocity model gradients as

$$\mathcal{K}^{\hat{\alpha}}(\mathbf{x}) = -\sum_e \int_0^T \mathbf{u}_\alpha^\dagger(\mathbf{x}, t, e) \cdot \boldsymbol{v}^\alpha(\mathbf{x}, t, e)\, \mathrm{d}t \tag{5.6}$$

and

$$\mathcal{K}^{\hat{\beta}}(\mathbf{x}) = \sum_e \int_0^T \mathbf{u}_\beta^\dagger(\mathbf{x}, t, e) \cdot \boldsymbol{v}^\beta(\mathbf{x}, t, e)\, \mathrm{d}t, \tag{5.7}$$

where the gradient terms are simply computed by taking the dot-product of the state $\left(\mathbf{u}_\alpha^\dagger(\mathbf{x}, t, e) \text{ and } \mathbf{u}_\beta^\dagger(\mathbf{x}, t, e)\right)$ and adjoint-state $\left(\boldsymbol{v}^\alpha(\mathbf{x}, t, e) \text{ and } \boldsymbol{v}^\beta(\mathbf{x}, t, e)\right)$ variables. We calculate the latter by forward-propagating the adjoint sources, which are a function of P- and S-wavefield energy. We refer readers to Oren and Shragge (2022) that includes a detailed mathematical derivation and definitions of the adjoint-state variables.

The practical implementation involves an illumination compensation procedure (Warner et al., 2013; Yang et al., 2013) applied on the each gradient to reduce the artifacts in the vicinity of source locations. The illumination effect can be approximated by the total adjoint-state wavefield energy, which is largely accounted for in the gradients through a stabilized normalization process. Finally, we apply short vertical and horizontal smoothing operators to the individual gradients, which are then summed over the selected shots.

5.2.5 Iterative velocity model updating

The solution to the inverse problem is determined by iteratively minimizing the objective function. In each iteration, the model updates are calculated by a multiparameter line-search method (Tang and Ayeni, 2015) in the steepest-descent direction (Nocedal and Wright, 2006). After searching for individual P- and S-wave step lengths, we conduct a final line search along a 2D vector whose components are the calculated P- and S-wave search directions (Witten and Shragge, 2017a). To find the magnitude of the update, we multiply the negative of gradient by the optimal step length, which is then added to the current velocity model:

$$m^k_{i+1} = m^k_i - h_i\,\mathcal{K}^k_i, \quad k = \hat{\alpha}, \hat{\beta}, \tag{5.8}$$

where m is the velocity model, h is the step length, and i is the iteration number. The iterative inversion process is typically stopped when the gradient of the objective function becomes zero or turns positive.

5.3 Field data experiment: A DAS 3D VSP data set from the North Slope of Alaska

Gas hydrate is a naturally occurring material made up of an open lattice of water molecules that traps molecules of numerous gases (most commonly methane) under specific pressure and temperature conditions (Sloan and Koh, 2007). As such hydrate deposits can trap massive amounts of carbon, and they are studied as a potential energy resource as well as an important part of the global climate cycle (Collett, 2002). Because existing geological and geophysical studies confirm the wide-spread presence and relatively straightforward accessibility of large gas hydrate reservoirs on the Alaskan North Slope, the U.S. Department of Energy (DOE) National Energy Technology Laboratory (NETL), Japan Oil, Gas and Metals National Corporation (JOGMEC), and the U.S. Geological Survey (USGS) have been closely collaborating to develop a long-term hydrate test facility (Boswell et al., 2020; Haines et al., 2020). As a result of this collaboration, the Hydrate-01 stratigraphic test well was drilled in the Prudhoe Bay Unit on the North Slope of Alaska in 2018 to acquire petrophysical and seismic data (Boswell et al., 2022). A DAS fiber optic cable was cemented to the well casing during well completion. A large-scale active-source DAS 3D VSP data set was subsequently acquired in 2019 at the Hydrate-01 well with the goal of generating a high-resolution baseline subsurface seismic image to support the long-term production testing of the hydrate reservoirs and future time-lapse seismic analyses (Fujimoto et al., 2021). Young et al. (2022) present a comprehensive DAS 3D VSP data preprocessing and acoustic prestack depth migration workflow for the same data set that uses a P-wave velocity model estimated using the aforementioned approach to generate high-quality near-well images to improve the understanding of the existing gas-hydrate systems.

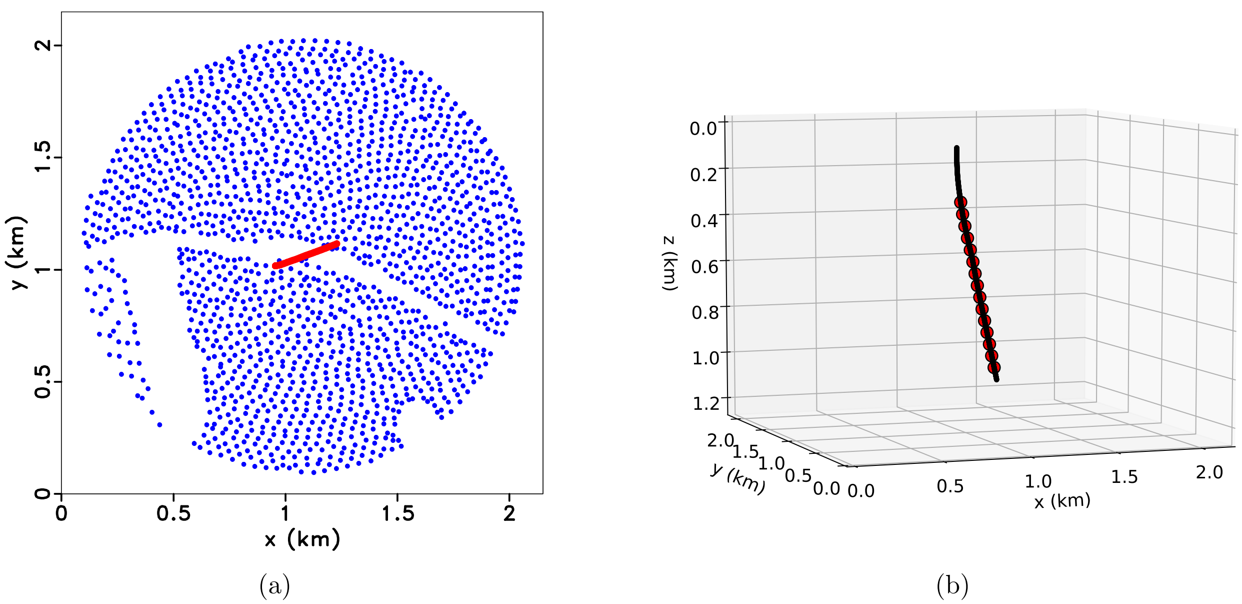

Figure 5.1 Acquisition geometry of the DAS 3D VSP data set. (a) The blue dots denote the source locations while the red dots indicate the well trajectory. (b) The black dots show the DAS cable whereas the red dots represent the "reciprocal" shots used in the inversion experiment after the VSP data are sorted into a common-receiver configuration.

The DAS 3D VSP survey includes a total of 1701 vibroseis source points exhibiting a dense radial acquisition pattern centered around the well head with a 1.1 km maximum source-well head offset. A pair of vibroseis trucks generated a sweep frequency between $2 - 200$ Hz with multiple sweeps at each location. The total number of effective receiver locations is 994 with an approximate 1.0 m sample spacing and a 3.0 m gauge length. The top and bottom receiver measured depths are 0.014 km and 1.069 km, respectively. The total record length is 2000 ms with a 1.0 ms sampling rate. Figure 5.1 displays the acquisition geometry along with the reciprocal source positions in the borehole used in the following inversion experiment.

5.3.1 Data conversion from strain rate into displacement

As indicated above, the image-domain tomography algorithm requires having displacement data input. Because we are originally provided with the strain-rate DAS measurements, a data conversion step to displacement is needed prior to imaging or inversion. To achieve this goal, we follow a strategy discussed in Daley et al. (2016) and Lindsey et al. (2020), which approximates the particle velocity field as:

$$\dot{U}_z(\omega) = -\left(\frac{\omega + \eta_\omega}{k_z + \eta_{k_z}}\right) E_{zz}(k_z, \omega), \tag{5.9}$$

where $E_{zz}(k_z, \omega)$ is the Fourier-transformed strain rate of the wavefield measured in the direction of the fiber axis (i.e., typically vertical for VSP scenarios); k_z is vertical wavenumber; ω is angular frequency; η_ω and η_{k_z} are stability parameters to avoid dividing by small numbers; and $\dot{U}_z(\omega)$ is the resulting approximated frequency-domain vertical particle velocity field. To estimate the displacement field, we apply half-order integration on the particle velocities to recover $U_z(\omega)$. Figure 5.2 depicts a DAS 3D VSP shot gather example illustrating the original strain-rate measurements as well as the approximated displacement data obtained by means of the conversion procedure shown in equation 5.9. Note how the high-quality data in both formats are largely noise-free and clearly exhibit elastic full-wavefield behavior. It is also worth pointing out that although the inversion algorithm used herein is originally formulated for multicomponent data (Oren and Shragge, 2022), we are restricted to using single-component (vertical) DAS VSP recordings as the directivity of our optical fiber measurements is mainly sensitive to the vertical particle motion (Hornman, 2017).

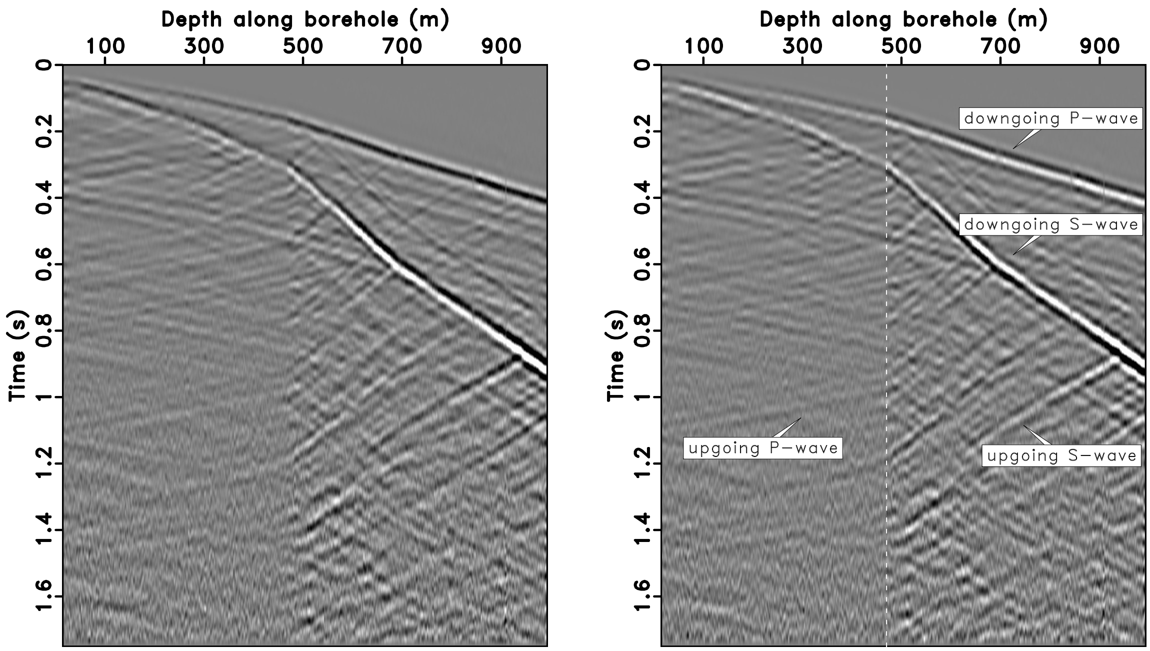

(a) (b)

Figure 5.2 A 3D DAS VSP shot gather showing (a) the original strain rate and (b) the approximated displacement data obtained using the data conversion step presented in equation 5.9. The vertical white dashed line indicates the base of the significant ice bearing permafrost.

5.3.2 Data preconditioning and initial model building

We apply minimal preprocessing to the input data prior to inversion. After obtaining the approximated displacement measurements as described above, we sort the shot gathers into common-receiver gathers, which enables us to generate a reciprocal source and receiver geometry (i.e., the sources and receivers are positioned at the borehole and surface, respectively). This step is followed by applying a 25 Hz high-cut filter to condition the data specifically for inversion, and separating the direct downgoing P- and S-wave arrivals by using linear mute functions. We then select 15 reciprocal shots along the borehole between 0.3 km and 1.0 km in depth spaced at a 50 m interval, which are directly used in the image-domain inversion process. Figure 5.3 shows a reciprocal shot gather extracted at $[x, y, z] = [1.111, 1.072, 0.710]$ km along with the isolated direct P- and S-wave data used in the TRI procedure.

Our starting model building strategy exploits a suite of petrophysical logs that were acquired along the borehole (Figure 5.2) down to the 1.0 km termination depth during the drilling operation with the goal of identifying the key lithological units within the area of interest. The initial 1D P- and S-wave velocity profiles are constructed by heavily smoothing the P- and S-wave sonic logs, and extrapolating these profiles throughout the 3D model domain as shown in Figure 5.4. Note the strong velocity inversion due to the presence of a roughly 600 m thick permafrost zone. With the proposed inversion procedure, we aim at recovering the 3D heterogeneous velocity perturbations required for generating high-quality structural images, which would facilitate future reservoir analyses.

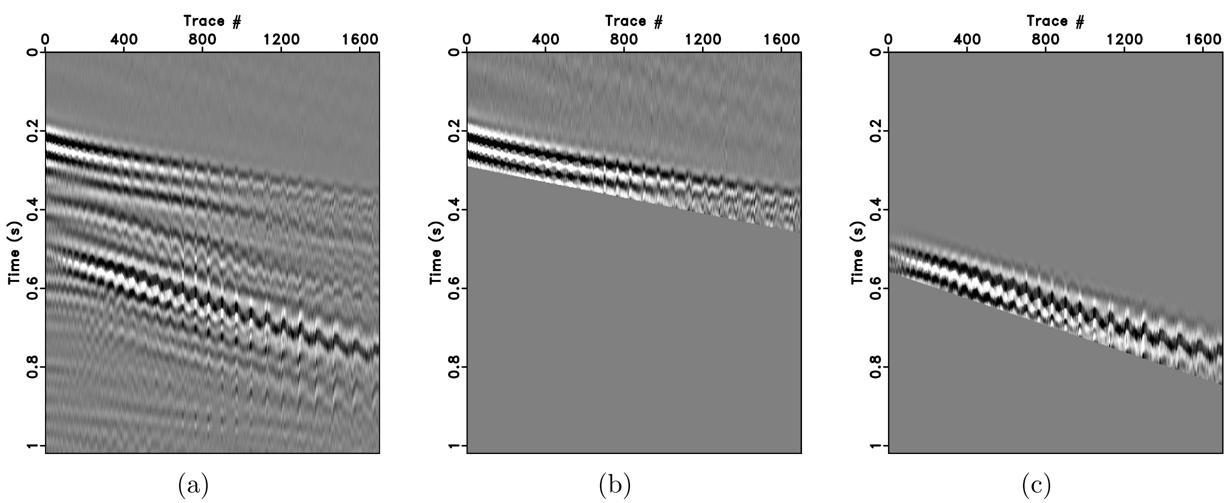

Figure 5.3 (a) An example of a common-receiver (i.e., reciprocal shot) gather extracted at $[x, y, z] = [1.111, 1.072, 0.710]$ km and sorted by radial offset from the borehole, which ranges from 0.01 m to 1.1 km at Traces 1 and 1699, respectively. Windowed downgoing (b) P- and (c) S-wave first-arrival waveforms used in the TRI process.

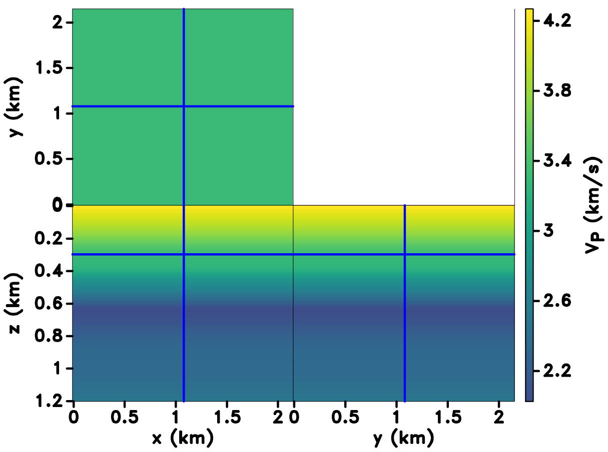

(a)

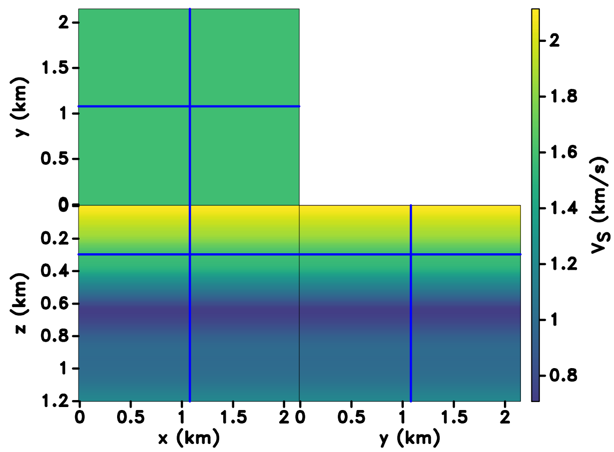

(b)

Figure 5.4 Initial 1D (a) V_P and (b) V_S models. Note the strong velocity inversion in each panel due to the presence of a roughly 600 m thick permafrost zone.

5.3.3 Inversion results

We conduct the tomography process on a grid with a discretization interval of $[\Delta x, \Delta y, \Delta z] = [18, 18, 9]$ m and a 3D model domain of $[N_x, N_y, N_z] = [120, 120, 240]$ grid points, which results in a model size of 2.16×2.16×2.16 km^3. For forward and adjoint wave propagations, we use a graphics processing unit (GPU)-based finite-difference time-domain (FDTD) solver with the second-order temporal and eighth-order spatial accuracy stencil (Weiss and Shragge, 2013) optimized to run on NVIDIA V100 GPU hardware. Our numerical simulations use boundary conditions consisting of absorbing boundary (Clayton and Enquist, 1977) and exponential-damping sponge-layer (Cerjan et al., 1985) operators. We do not apply the free-surface boundary condition because a top absorbing boundary is applied to forestall the generation of multiples, which have been excluded from the windowed data.

We select the inversion parameters to be $[\epsilon_1, \epsilon_2, \epsilon_3] = [1.0, 10^{-5}, 10^{-5}]$ to emphasize the optimization of the extended term while downweighting the contributions of the zero-lag terms by two orders of magnitude relative to the extended term in the objective function. Furthermore, we choose the zero-lag and extended penalty widths to be $w = 10.0$ and $[\sigma_x, \sigma_y, \sigma_z] = [0.08, 0.08, 0.08]$, respectively, to effectively remove the well-focused energy in the images. Finally, we extend the images by $[\,|\lambda_x|, |\lambda_y|, |\lambda_z|\,] \leq 0.15$ km because such an extension adequately captures the shifted energy (see Figure 5.6) arising due to the inaccurate starting models (see Figure 5.4). We construct the extended image gathers at the reciprocal source locations along the borehole as opposed to microseismic scenarios where one typically evaluates extended images at the spatial point that corresponds to the zero-lag PS image maximum (Oren and Shragge, 2021a; Witten and Shragge, 2015).

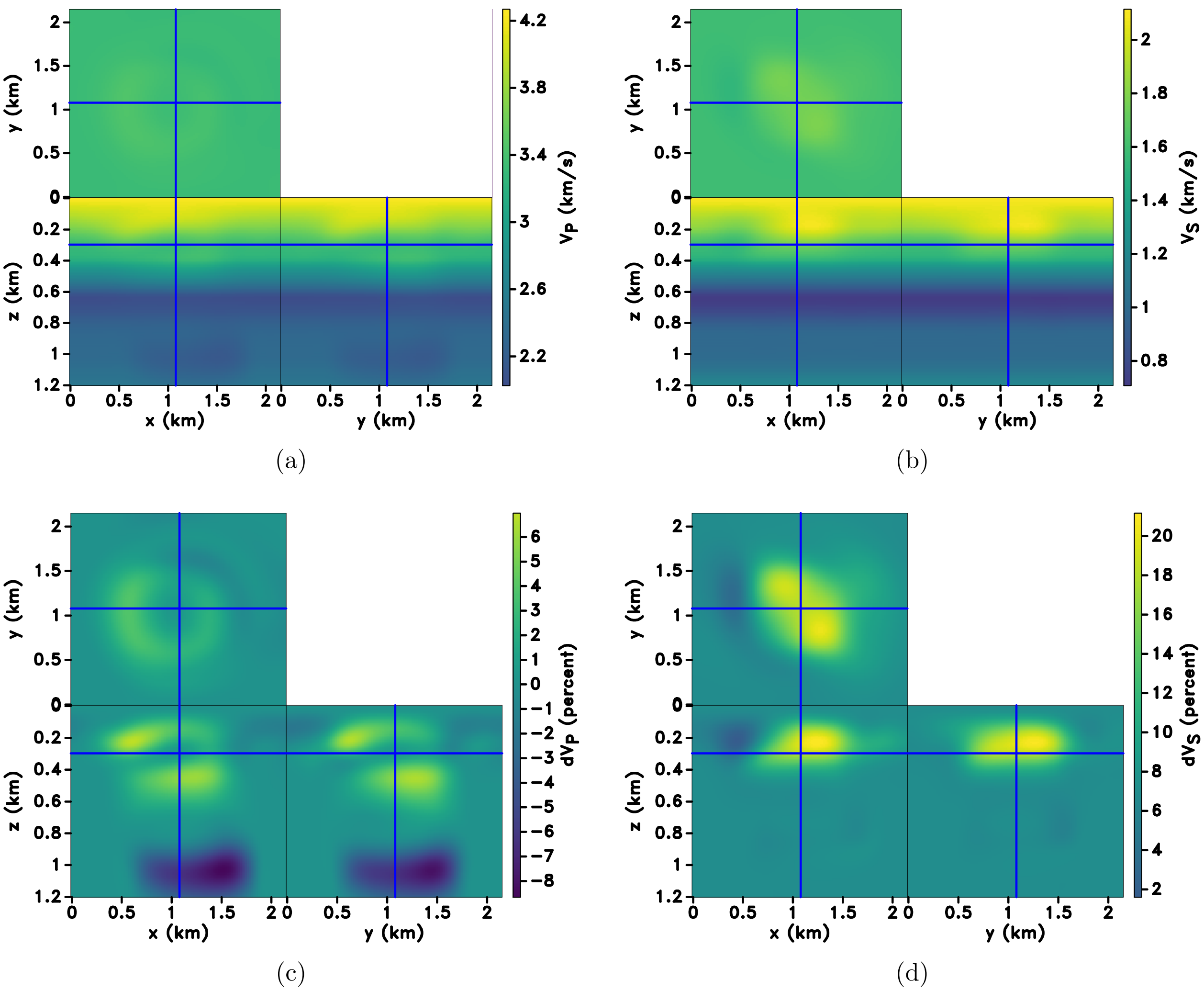

Figure 5.5 Recovered (a) V_P and (b) V_S models along with the percentage change from the background 1D models in the (c) V_P and (d) V_S models.

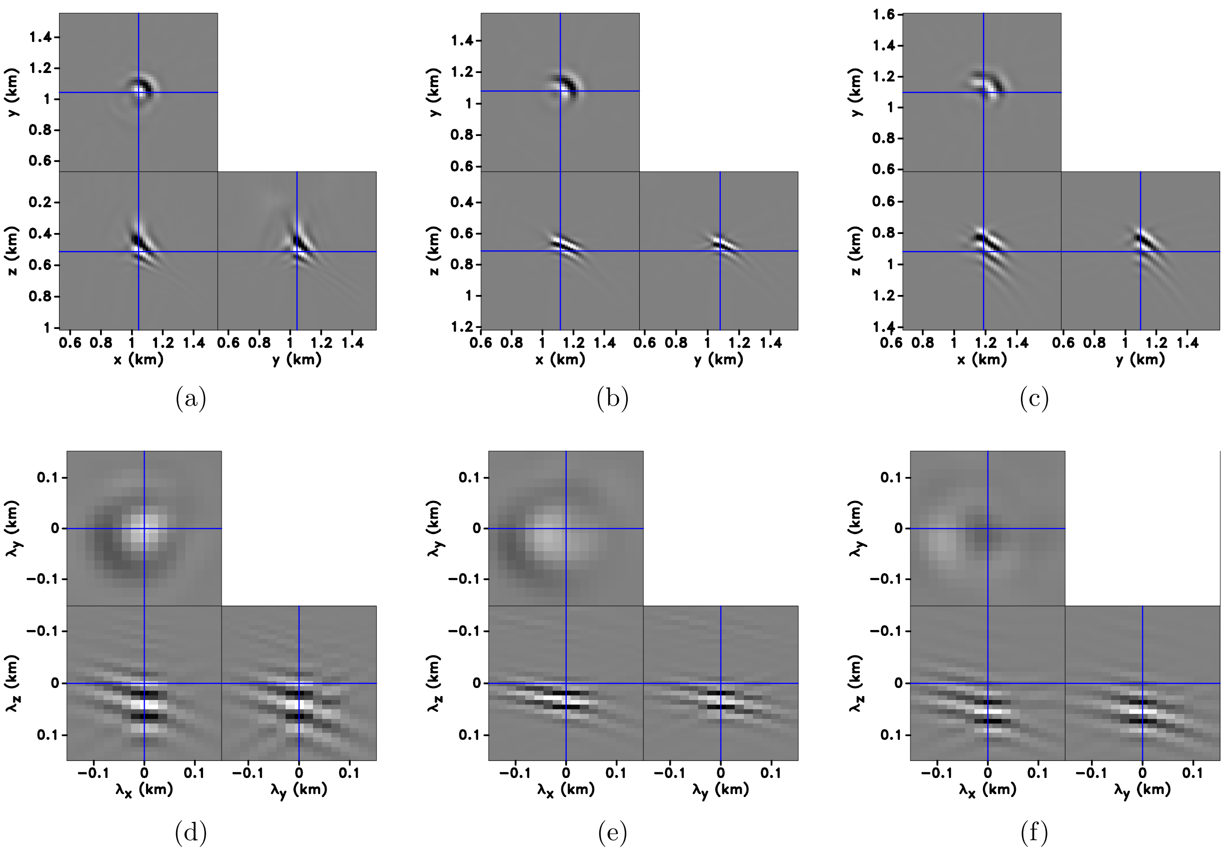

Figure 5.6 (a)-(c) Zero-lag and (d)-(f) space-lag extended image gathers computed using the initial velocity models. The blue crosshairs in the zero-lag and extended images respectively show the true reciprocal source locations and the zero lag. The images in (d)-(f) are respectively computed the following locations in (a) $[x, y, z] = [1.045, 1.047, 0.507]$ km, (b) $[x, y, z] = [1.111, 1.072, 0.710]$ km, and (c) $[x, y, z] = [1.178, 1.096, 0.913]$ km.

Figure 5.5 depicts the inverted V_P and V_S models along with the percentage velocity change after applying ten tomographic iterations. Analyzing the recovered velocity updates in the V_P model, we note increased velocities up to 6.5% within the ice-bearing permafrost zone down to a depth of 0.5 km, whereas the velocities are decreased by up to -8.5% between $0.9-1.2$ km in depth, which partially includes the second hydrate unit. We observe mostly 1D velocity updates within the deep part due to a considerably narrowing aperture angle between reciprocal sources and receivers. Moreover, the recovered V_S model exhibits a significant velocity increase up to 21% throughout the permafrost zone, while the deeper part below that zone exhibits little-to-no model updating.

5.3.4 TRI-based inversion validation

We validate our recovered elastic models based on the focusing of the zero-lag and extended source images constructed with the TRI procedure. We first evaluate the quality of the initial models shown in Figure 5.4. Figure 5.6 presents three representative initial zero-lag images associated with sources that are vertically offset from each other by roughly 200 m, as well as their extended versions that are evaluated at the corresponding true source locations. To attenuate the elastic zero-lag imaging artifacts, we choose t_{max} in equation 5.2 to be 0.3 s through trial and error. While the initial zero-lag images exhibit poorly focused energy outside of the true source locations (i.e., the blue crosshairs in Figure 5.6a-c), the extended image gathers feature energy shifted downwards with respect to zero lag (i.e., the blue crosshairs in Figure 5.6d-f), which clearly indicates the required velocity update direction (i.e., increased velocities). Figure 5.7 shows the final zero-lag and extended image gathers computed using the inverted models in Figure 5.5. Relative to the initial imaging results, we note that the focusing in the final zero-lag images is stronger at the source locations, and the extended images exhibit well-focused energy in the vicinity of zero lag indicating that the updated imaging velocities are more accurate relative to the starting models.

Another approach to validate the recovered velocity models using the TRI results is to interpret the calculated Euclidean distance between the estimated and true source locations as the spatial root-mean square (RMS) error. By following the work of Oren and Shragge (2022), we estimate the source locations by picking the maximum absolute value in each zero-lag image $I_{\alpha\beta}(\mathbf{x}, e)$. Figure 5.8a and Figure 5.8b respectively presents two crossplots between the initial and final total and depth RMS errors for all 15 sources used in the inversion. These results indicate that we achieve a total RMS location error reduction of 70% with the inverted models. The average depth error, which contributes to the total RMS error, decreases from 11.3 m to 0.9 m (i.e., a reduction of 92%). This implies that the majority of the total RMS error arises from the more limited lateral (i.e., $x-$ and $y-$directions) resolution of the source images, which is likely affected by the relatively narrow imaging aperture and Fresnel zone considerations. Moreover, the Figure 5.8 colorbars indicate that the deeper ($z > 0.5$ km) sources generally exhibit lower total and depth errors compared to shallower ($z \leq 0.5$ km) sources. We attribute this observation to the imperfect TRI results at shallow locations mainly affected by the relatively weak amplitudes of the P wavefield backpropagated from wider offsets due to reduced DAS fiber sensitivity to P waves at larger angles as well as the complex permafrost zone, both of which tend to degrade the image quality.

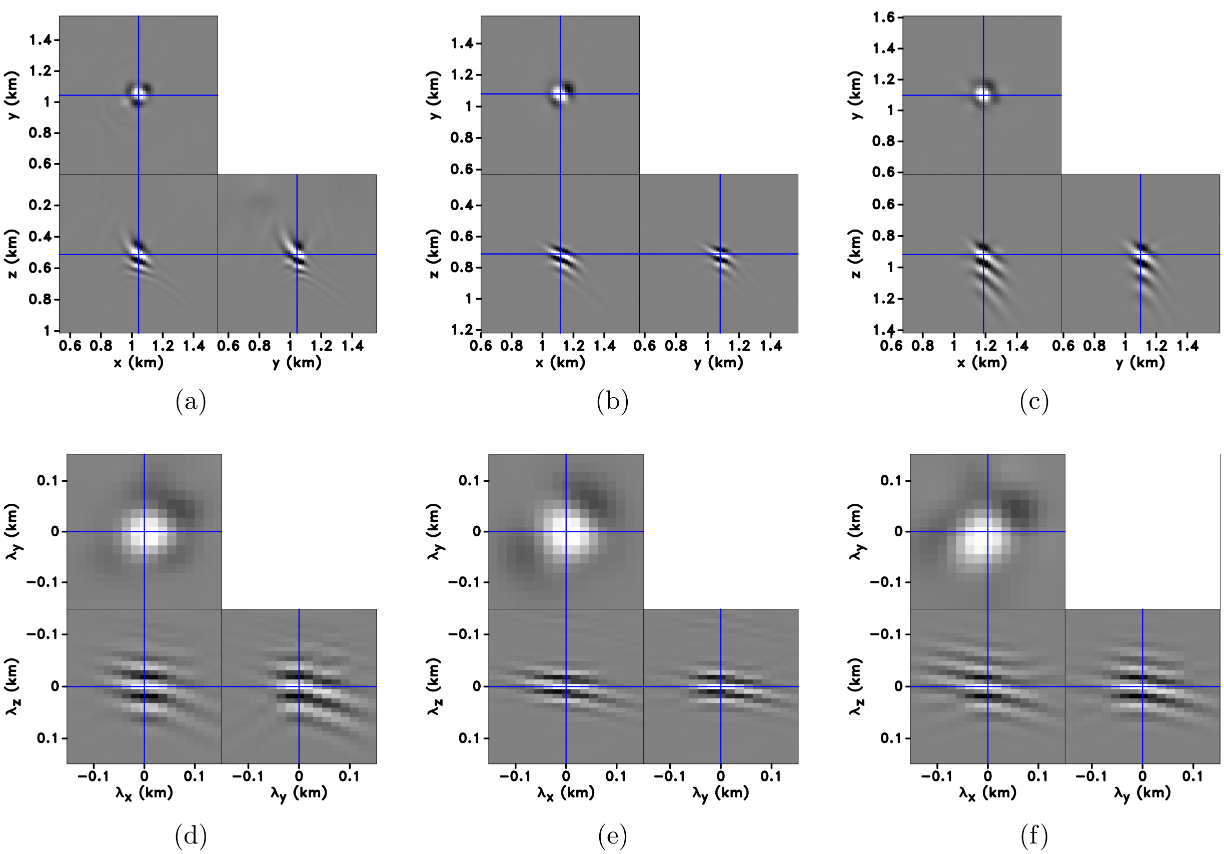

Figure 5.7 (a)-(c) Zero-lag and (d)-(f) space-lag extended image gathers computed using the inverted velocity models. Note how the images exhibit improved focusing around the source location as well as zero lag relative to the initial imaging results shown in Figure 5.6.

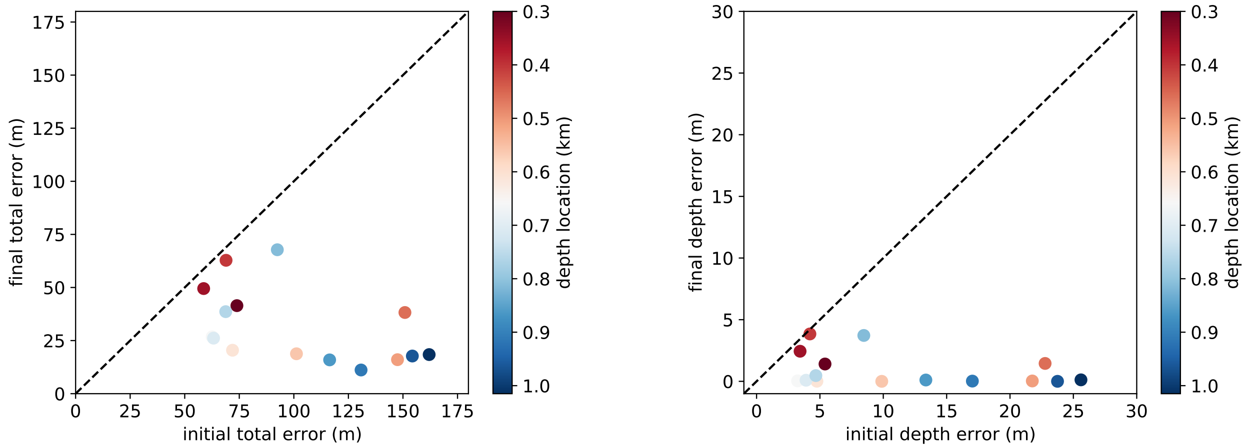

(a) (b)

Figure 5.8 Crossplots of the initial and final (a) total and (b) depth RMS location errors of the reciprocal sources. Points falling along the dashed line indicates no change in error whereas those below the line indicate improved source location estimates. The colorbar represents the depth location of the sources. The results show an approximately 70% decrease in total location errors while a depth error reduction of 92% on average over all sources.

5.3.5 Inversion validation through elastic reverse time migration

We construct elastic RTM images (i.e., energy, PS, and SS) using different imaging conditions with the goal of obtaining complementary reflectivity information of specified wave modes at interfaces of discontinuous physical properties. Besides the previous TRI-based inversion validation step, the elastic RTM images allow us to further evaluate the quality of the inverted models through well-tie analysis. Our elastic RTM algorithm maps the preprocessed upgoing DAS VSP data to a subsurface image using the following steps: (1) forward model a source wavefield using an estimated wavelet while saving this wavefield at the domain boundaries, (2) reconstruct the source and receiver wavefields through reverse-time propagation, and (3) evaluate an imaging condition on-the-fly to extract a reflectivity image from the extrapolated source and receiver wavefields (Chang and McMechan, 1987; Yan and Sava, 2008; Yan and Xie, 2012).

We are provided with two data sets for structural imaging: (1) the full upgoing wavefield data that contain both P- and S-wave arrivals (Figure 5.9a) used in the energy norm imaging condition (Rocha et al., 2017), and (2) the separated upgoing S-wave data (Figure 5.9b) that predominantly includes reflected S waves and P-to-S conversions used to generate the PS and SS images. Minimal preprocessing was carried out on both data sets by deconvolving the source signature to obtain more balanced spectra, as well as by filtering out the wavefield energy beyond 50 Hz to make the elastic imaging process feasible with the available computational GPU resources. Similar to the strategy presented in the previous image-domain inversion approach, we migrated the reciprocal shot gathers after decimating the total number of shots to 25 distributed throughout the borehole because our initial testing showed that migrating an increased number of shot gathers did not significantly improve the results.

Herein we present a number of different elastic images formed by correlating source and receiver wavefields that include either decomposed P- and S-wave modes or non-decomposed data that consist of various wave modes. To construct the energy image, we use the energy norm imaging condition that does not require wave-mode decomposition, and produces a scalar image that is free of backscattering artifacts (Rocha et al., 2017). To generate the converted wave PS and SS images, we exploit the kinetic term of the PS energy imaging condition originally developed for microseismic data (Oren and Shragge, 2021a). Active-source DAS VSP imaging implementation of the PS energy imaging condition requires a straightforward replacement of the first adjoint wavefield with a source wavefield decomposed into its associated P- or S-wave mode. During source wavefield reconstruction, we assume that the medium is isotropic and the following differential operators $\mathbf{u}_\alpha = \nabla\nabla \cdot \mathbf{u}$ and $\mathbf{u}_\beta = -\nabla \times \nabla \times \mathbf{u}$ judiciously decompose the displacement field ($\mathbf{u}$) into its P($\mathbf{u}_\alpha$) and S($\mathbf{u}_\beta$) wavefield components. The separated upgoing S-wave data are injected at the reciprocal receiver locations and then backpropagated through the model domain when reconstructing the receiver wavefield.

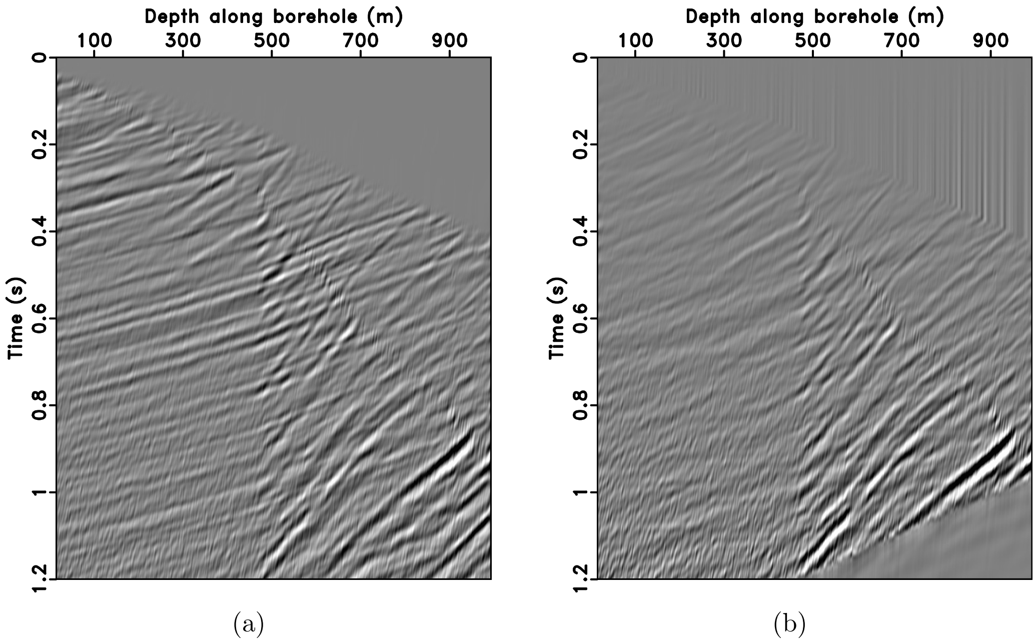

Figure 5.9 DAS 3D VSP shot gathers showing (a) upgoing wavefield energy including both P- and S-wave modes and (b) upgoing S-wave energy separated through preprocessing from data shown in (a).

Figure 5.10 depicts the inline and crossline images extracted from the 3D energy RTM volume and computed with the initial and inverted P- and S-wave velocity models. We have also overlain the P-wave sonic log data shown in blue along with several key interpreted horizons denoted by dashed lines in different colors. In general, both initial and final image quality is rather high with coherently imaged structures in and below the ice-bearing permafrost zone, the base of which is roughly at 574 m in depth. However, the final imaged reflectivity appears to better match the log data and interpreted horizons associated with the base of ice-bearing permafrost levels (green and yellow dashed lines), as well as the target gas hydrate reservoir tops (cyan and magenta dashed lines) relative to those in the initial energy images.

Figure 5.11 displays the initial and final inline sections extracted from the 3D PS and SS RTM volumes. We note that the final images exhibit improved coherency of the imaged reflectivity within the permafrost zone. Moreover, the key gas hydrate reservoirs are successfully imaged in both PS and SS images. Compared to the previous energy imaging results, the PS and SS image quality overall appears to be less coherent because the preprocessing steps (e.g., deconvolution) primarily aimed at optimizing the upgoing P-wave energy that seems to dominate the DAS VSP recordings relative to the upgoing S-wave energy (see Figure 5.9). We assert that S-wave-oriented preprocessing is needed to enrich the higher-frequency S-wavefield components that may result in enhanced PS and SS images. Also, compared to the energy and PS imaging results, SS images exhibit more semicircular migration artifacts, which can be largely attenuated through post-migration filtering.

5.4 Discussion

The actual benefit of the inverted elastic velocity models comes when they are used as input in acoustic/elastic depth imaging algorithms (e.g., RTM), which intrinsically drive the need for accurate models. Relative to traditional surface-recorded seismic data, elastic near-well imaging seems more achievable for VSP data because it is easier to separate upgoing from downgoing waves and upgoing P- from S-wave energy. Moreover, given properly preprocessed S-wave data as discussed above, complementary PS and SS images may lead to more useful geological inference (e.g., higher-resolution reflectivity and sharper fault structures) compared to conventional PP images as the wavelengths of S waves are shorter than those of P waves. We note that the PS and SS imaging results presented herein open up possibilities for robust elastic imaging with different wave paths and illumination of distinct wave modes. In addition to the conventional RTM approach, one can also consider exploiting the elastic least-squares RTM (LSRTM) technology that potentially delivers images with more accurate amplitudes, less artifacts emerged due to incomplete acquisition, and better resolved reflectivity (Feng and Schuster, 2017). However, especially for 3D implementations, the computational cost of the elastic LSRTM procedure remains substantially more expensive than its acoustic counterpart.

As thoroughly discussed in Oren and Shragge (2022), the computational expense of the applied inversion procedure is one of the drawbacks, and primarily depends on the forward and adjoint elastic wavefield propagations. The number of sources and space lags used for the extended image computation are the other factors influencing the cost. For the presented 3D field data experiment, each iteration takes nearly 3.0 hours on a single NVIDIA V100 GPU device when using 15 sources. These results suggest that a real data application similar to the Alaska DAS VSP data set may be carried out within a more reasonable time frame particularly when following a data parallelism or domain-decomposition strategy involving multiple GPU nodes.

Because the current tomographic approach uses an isotropic parameterization, the inverted velocity models may be compensating for anisotropy effects. Unlike the isotropic inversion results presented herein, one could incorporate anisotropy into the current velocity model building approach. One strategy to meet this goal is to invert for the Thomsen (1986) anisotropy coefficients along with the vertical velocities V_{P0} and V_{S0} depending on the symmetry assumption. In this case, one can use the PS energy imaging condition that exhibits sensitivity to anisotropy parameters for various transversely isotropic symmetries as demonstrated by Oren and Shragge (2021b). However, this would require a more challenging multiparameter inversion, which likely will suffer from interparameter cross-talk. A less demanding procedure (though potentially less accurate) is to first estimate the relevant parameters from existing (e.g., borehole) measurements and then only invert for vertical velocities while including the estimated anisotropy in the forward and adjoint wavefield propagations that generate the state and adjoint state variables used for the inversion process.

There is potential to use the presented tomographic framework on a variety of borehole DAS data sets in onshore and offshore environments, including as an essential precursor analysis to generate high-quality starting models essential for elastic VSP FWI applications (Egorov et al., 2018b; Podgornova et al., 2017). In addition to the field data implementation presented herein, another onshore application may be time-lapse reservoir monitoring during hydrocarbon production or CO_2 injection (Yurikov et al., 2021). Potential deepwater applications include but are not limited to 3D near-well imaging of reservoir depths (Jiang et al.,

2016) or complex structures such as salt flanks (Duan et al., 2020), as well as cost-effective 4D monitoring of production-related operations including water injection or other types of recovery stimulation (Kiyashchenko et al., 2019). As opposed to the onshore DAS VSP settings, though, one would expect to observe relatively weak elastic behaviour (recorded P-to-S conversions) in deepwater scenarios, which may affect the success of the proposed elastic inversion method.

5.5 Conclusions

We have successfully adopted a recently proposed passive-style image-domain elastic inversion method for active-source DAS VSP configurations to update P- and S-wave velocity models. This implementation is made possible by source-receiver reciprocity as if the sources were positioned at borehole while the data were recorded at the surface. We apply the inversion approach to an active-source DAS 3D VSP data acquired in the North Slope of Alaska. We use 15 reciprocal sources to reconstruct reasonably accurate V_P and V_S models. We validate the inverted velocities by investigating zero-lag and extended images constructed through TRI, as well as source location estimates. The velocity updates decrease the total source location RMS error by 70% as well as a 92% reduction in the final average depth error. We also generate several elastic RTM images based on the estimated velocity models showing interpretable reflectivity that matches petrophysical log data in well-ties.

5.6 Acknowledgements

We acknowledge the Center for Wave Phenomena (CWP) consortium sponsors for their financial support. We thank DOE NETL, JOGMEC, and USGS for providing access to the Alaskan North Slope DAS VSP data set. Financial support for DAS VSP data acquisition was provided by the U.S. Department of Energy National Energy Technology Laboratory (NETL) the U.S. Geological Survey Energy Resources Program and the Ministry of Economy, Trade and Industry (METI) Japan MH21-S R&D consortium. We also thank Whitney Schultz (Occidental Petroleum Corporation) and Jim Simmons (Reservoir Characterization

Project) for processing the DAS VSP data set. We acknowledge Seth Haines (USGS), Tim Collett (USGS), and Cullen Young (CWP) for many useful discussions regarding this project. The reproducible numerical examples in this paper were generated using the Madagascar software package using the Wendian HPC systems made available through the Colorado School of Mines.

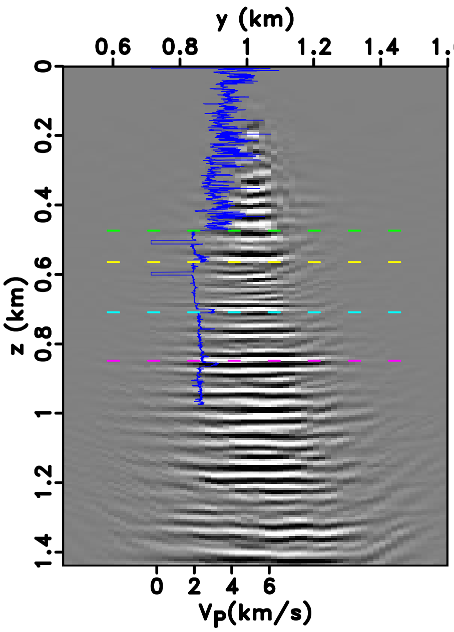

(a)

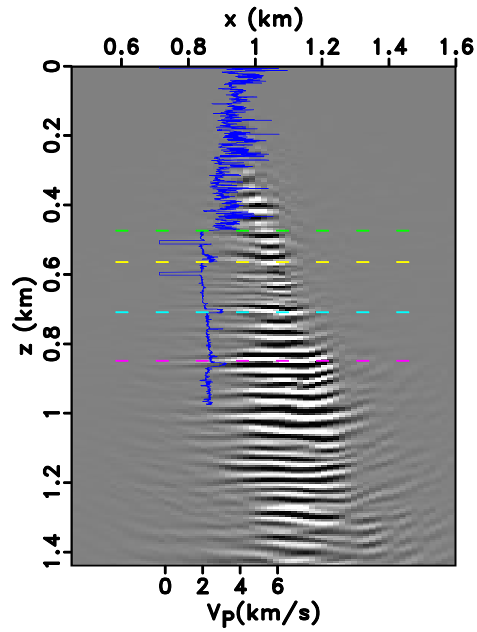

(b)

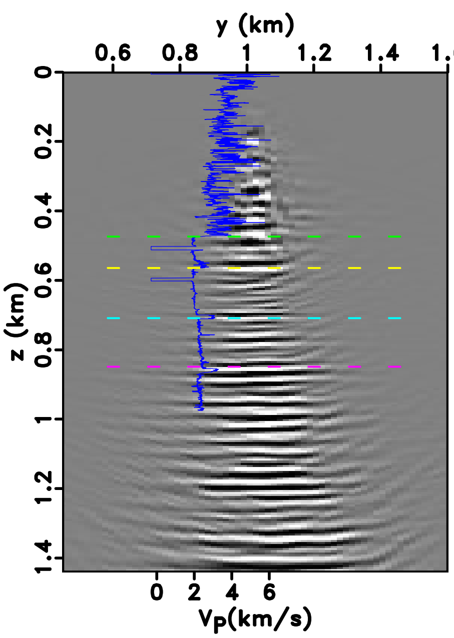

(c)

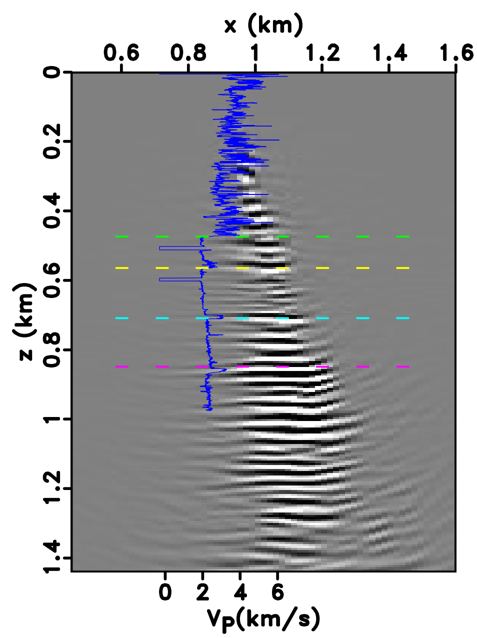

(d)

Figure 5.10 (a)-(b) Initial and (c)-(d) final energy images overlaid with the V_P well log shown in blue, as well as the dashed lines that represent several key target levels. While the yellow and green lines denote the base of ice-bearing permafrost and base of significant ice-bearing permafrost; the cyan and magenta lines indicate the tops of the two gas hydrate reservoirs. Left and right columns respectively represent the inline and crossline sections extracted at $x = 0.97$ km and $y = 1.04$ km. Note how the imaged structures in the final RTM results better match with the highlighted target levels compared to those in the initial RTM results.

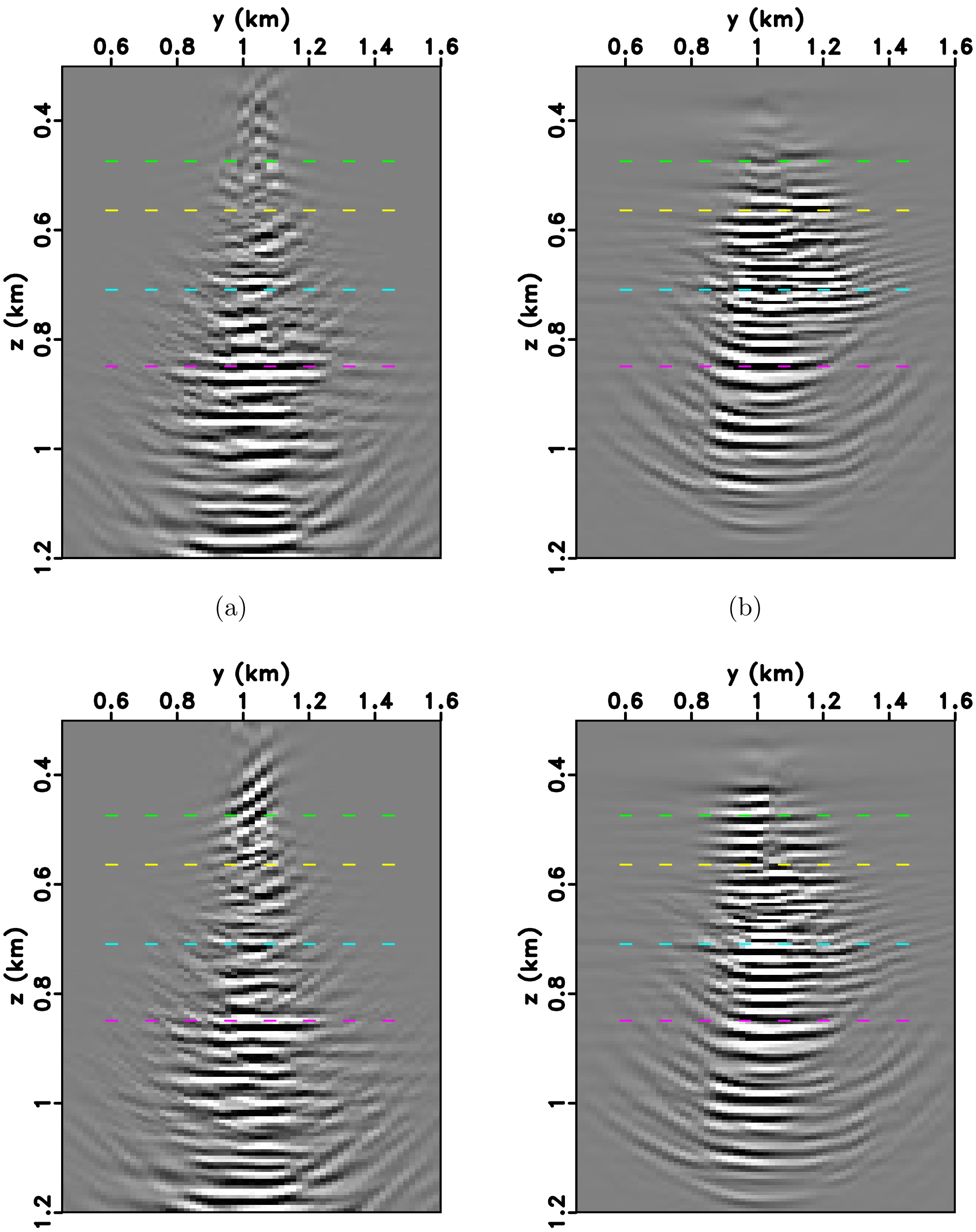

(a) (b) (c) (d)

Figure 5.11 (a)-(b) Initial and (c)-(d) final PS (left column) and SS (right column) images. Both images are the inline sections extracted at $x = 0.97$ km. Note how the imaged reflectors in the final RTM results appear to be more coherent and better match with the key horizons compared to those in the initial RTM results.

CHAPTER 6

CONCLUSIONS

In this thesis, I propose various 3D elastic imaging and tomography algorithms for different types of passive- and active-source seismic data acquired for surface microseismic monitoring or vertical seismic profiling (VSP) surveying coupled with distributed acoustic sensing (DAS) optical fibers. The tomographic velocity model building method is formulated in the image domain and thus requires an elastic imaging condition that is adequately sensitive to model perturbations. In Chapter 2, I introduce a robust (extended) PS energy imaging condition used within the time-reverse imaging (TRI) concept, which is suitable for locating microseismic events in 3D elastic isotropic media. Given a synthetic test, I also show that the proposed imaging technique produces zero-lag and extended source images that exhibit sufficient sensitivity to velocity model errors, which makes this imaging condition suitable for 3D image-domain elastic velocity inversion algorithms.

Making isotropic media assumptions in TRI and image-domain inversion approaches may not be sufficient especially when unconventional reservoirs are located within highly anisotropic massive shale formations. In Chapter 3, I present a sensitivity analysis of the anisotropy signature in zero-lag and extended PS energy images in 3D VTI (transversely isotropic with a vertical symmetry axis), HTI (transversely isotropic with a horizontal symmetry axis), and ORT (orthorhombic) media. Using the realistic SEAM Barrett Unconventional model, I analyze the PS energy imaging results revealing useful moveout patterns due to perturbations in the Thomsen (1986) anisotropy coefficients $[\epsilon, \delta, \gamma]$. The synthetic numerical tests demonstrate that the imaged events are largely influenced by errors in $[\epsilon, \delta]$, but exhibit almost no sensitivity to γ. Furthermore, the sensitivity analysis shows similar event location errors in the Barrett model for VTI and HTI media; however, I observe substantial location errors for ORT media. I assert that the presented sensitivity analysis provides useful information to determine a prospectus for image-domain anisotropic elastic tomography.

By exploiting the kinetic term of the aforementioned PS energy imaging condition, I devise a full-wavefield adjoint-state tomography formalism in Chapter 4 for multicomponent passive data to invert for isotropic P- and S-wave velocity models. I employ a multiterm objective function that incorporates various event images to ensure optimal zero-lag and extended image focusing, as well as consistency between the recovered elastic velocity models. The developed inversion framework does not require arrival picking and thus can offer more robustness to low signal-to-noise data relative to pick-based inversion methods. The realistic synthetic numerical experiments demonstrate that the proposed image-domain tomography approach can generate elastic models that greatly reduce the event location errors compared to the initial model estimates.

In Chapter 5, I extend the application of the proposed passive-style image-domain elastic tomography formalism to active-source DAS 3D VSP configurations for P- and S-wave velocity model updating. By exploiting source-receiver reciprocity, I create a DAS 3D VSP acquisition scenario where the sources and receivers are respectively located at borehole and surface, which mimics a surface microseismic monitoring setting. I illustrate the efficacy of the inversion approach on a DAS 3D VSP data set acquired in the North Slope of Alaska where significant gas hydrate deposits have been detected in two sub-permafrost sand layers. I first validate the estimated V_P and V_S models by examining the focusing of zero-lag and extended images constructed via TRI, as well as source location estimates. The inverted elastic models lead to a reduction of 70% and 92% in the total and depth source location RMS errors, respectively. I further validate the recovered velocity models by generating various elastic reverse time migration (RTM) images that show interpretable reflectivity of several key structures such as ice-bearing permafrost zone and gas hydrate reservoirs. The well-tie analysis results demonstrate that the final RTM images better match the existing petrophysical log data as well as the interpreted key horizons relative to the initial RTM images.

Lastly, I relate the contributions of each chapter as the following. I first develop an elastic TRI procedure to generate (extended) images of passive events in both isotropic and anisotropic media. The proposed imaging technique forms the basis of the elastic velocity model building algorithm that I devise to optimize the P- and S-wave velocity models that can be used in various imaging algorithms. Next, I demonstrate the effectiveness of the developed adjoint-state tomography method on an active-source fiber-optic 3D VSP data set acquired in the North Slope of Alaska. The field data results show that the elastic velocity models reconstructed through adjoint-state inversion improve the focusing of zero-lag and extended image gathers and significantly reduce the source location error. Furthermore, the optimized velocity models yield high-quality elastic RTM images of the target geological structures exhibiting highly accurate well-tie matches. Overall, the developed tools and workflows provide researchers with a complete inversion and imaging framework that can be used for a wide variety of earth investigations including, but not limited to, microseismic, gas hydrates, CO_2 geosequestration, geothermal and groundwater monitoring activities.

6.1 Future work

Considering the underlying physics of the methodology presented in this thesis, the proposed imaging and tomography framework may be applicable to different data types at variety of scales. At the reservoir scales, the presented wavefield methods may be useful for several passive- and active-seismic monitoring projects to investigate the changes in reservoir during hydrocarbon production, CO_2 sequestration, and waste-water injection. There is also potential for use at regional and global seismological scales where near-field and teleseismic earthquake data can be used to further refine the existing large-scale tomographic models. Given the relatively sparse receiver coverage as well as less signal-to-noise data levels at such scales, the presented wavefield imaging and inversion methods will not likely suffer from these restrictions. Moreover, there could be a great potential to apply the proposed framework on non-destructive damage testing used in civil engineering and quantitative structural health monitoring projects (e.g., tunnels, dams, and levees).

REFERENCES

Aki, K., and P. G. Richards, 2002, Quantitative seismology, 2nd ed.: University Science Books.

Albertin, U., P. Sava, J. Etgen, and M. Maharramov, 2006, Adjoint wave-equation velocity analysis, *in* SEG Technical Program Expanded Abstracts 2006: Society of Exploration Geophysicists, 3345–3349.

Alford, R. M., 1986, Shear data in the presence of azimuthal anisotropy: 56th Annual International Meeting, SEG, Expanded Abstracts, 476–479.

Alkhalifah, T., and I. Tsvankin, 1995, Velocity analysis for transversely isotropic media: Geophysics, 60, 1550–1566.

Aminzadeh, F., N. Burkhard, L. Nicoletis, F. Rocca, and K. Wyatt, 1994, SEG/EAEG 3-D modeling project: 2nd update: The Leading Edge, 13, 949–952.

Artman, B., I. Podladtchikov, and B. Witten, 2010, Source location using time-reverse imaging: Geophysical Prospecting, 58, 861–873.

Backus, G., and M. Mulcahy, 1976a, Moment tensors and other phenomenological descriptions of seismic sources - 1. Continuous displacements: Geophysical Journal International, 46, 341–361.

———, 1976b, Moment tensors and other phenomenological descriptions of seismic sources - 2. Discontinuous displacements: Geophysical Journal International, 47, 301–329.

Baker, T., R. Granat, and R. W. Clayton, 2005, Real-time earthquake location using Kirchhoff reconstruction: Bulletin of the Seismological Society of America, 95, 699–707.

Bardainne, T., and E. Gaucher, 2010, Constrained tomography of realistic velocity models in microseismic monitoring using calibration shots: Geophysical Prospecting, 58, 739–753.

Baysal, E., D. D. Kosloff, and J. W. Sherwood, 1983, Reverse time migration: Geophysics, 48, 1514–1524.

Ben-Menahem, A., and S. J. Singh, 1981, Seismic waves and sources: Springer-Verlag.

Bishop, T., K. Bube, R. Cutler, R. Langan, P. Love, J. Resnick, R. Shuey, D. Spindler, and H. Wyld, 1985, Tomographic determination of velocity and depth in laterally varying media: Geophysics, 50, 903–923.

Boswell, R., T. Collett, N. Okinaka, R. Hunter, K. Suzuki, M. Tamaki, J. Yoneda, and S. Haines, 2022, Hydrate-01 Stratigraphic Test Well, Alaska North Slope; Review of Technical Results: submitted to Energy & Fuels.

Boswell, R., T. Collett, K. Suzuki, J. Yoneda, S. Haines, N. Okinaka, M. Tamaki, S. Crumley, D. Itter, and R. Hunter, 2020, Alaska North Slope 2018 Hydrate-01 Stratigraphic Test Well: Technical results: Proceedings of the 10th International Conference on Gas Hydrates (ICGH10).

Bozdağ, E., D. Peter, M. Lefebvre, D. Komatitsch, J. Tromp, J. Hill, N. Podhorszki, and D. Pugmire, 2016, Global adjoint tomography: first-generation model: Geophysical Journal International, 207, 1739–1766.

Burdick, S., M. V. de Hoop, S. Wang, and R. D. van der Hilst, 2013, Reverse-time migration-based reflection tomography using teleseismic free surface multiples: Geophysical Journal International, 196, 996–1017.

Cerjan, C., C. Kosloff, R. Kosloff, and M. Reshef, 1985, A non-reflecting boundary condition for discrete acoustic and elastic wave equation: Geophysics, 50, 705–708.

Cervenỳ, V., 2001, Seismic ray theory: Cambridge University Press, 110.

Chambers, K., B. D. Dando, G. A. Jones, R. Velasco, and S. A. Wilson, 2014, Moment tensor migration imaging: Geophysical Prospecting, 62, 879–896.

Chang, W.-F., and G. A. McMechan, 1987, Elastic reverse-time migration: Geophysics, 52, 1365–1375.

Claerbout, J. F., 1971, Toward a unified theory of reflector mapping: Geophysics, 36, 467–481.

Clayton, R., and B. Enquist, 1977, Absorbing boundary conditions for acoustic and elastic wave equations: Bulletin of the Seismological Society of America, 67, 1529–1540.

Collett, T. S., 2002, Energy resource potential of natural gas hydrates: AAPG bulletin, 86, 1971–1992.

Crampin, S., 1985, Evaluation of anisotropy by shear-wave splitting: Geophysics, 50, 142–152.

Daley, T., D. Miller, K. Dodds, P. Cook, and B. Freifeld, 2016, Field testing of modular borehole monitoring with simultaneous distributed acoustic sensing and geophone vertical seismic profiles at Citronelle, Alabama: Geophysical Prospecting, 64, 1318–1334.

Deichmann, N., and D. Giardini, 2009, Earthquakes induced by the stimulation of an enhanced geothermal system below Basel (Switzerland): Seismological Research Letters, 80, no. 5, 784–798.

Dellinger, J., and J. Etgen, 1990, Wave-field separation in two-dimensional anisotropic media: Geophysics, 55, 914–919.

Díaz, E., and P. Sava, 2017, Cascaded wavefield tomography and inversion using extended common-image-point gathers: A case study: Geophysics, 82, no. 5, S391–S401.

Douma, J., and R. Snieder, 2015, Focusing of elastic waves for microseismic imaging: Geophysical Journal International, 200, 390–401.

Duan, Y., Y. Li, M. Kryvohuz, A. Mateeva, and T. Chen, 2020, 3D salt-boundary imaging with transmitted waves in DAS VSP data acquired in salt, *in* SEG Technical Program Expanded Abstracts: Society of Exploration Geophysicists, 370–374.

Duncan, P. M., and L. Eisner, 2010, Reservoir characterization using surface microseismic monitoring: Geophysics, 75, 139–146.

Dziewonski, A. M., T. A. Chou, and J. H. Woodhouse, 1981, Determination of earthquake source parameters from waveform data for studies of global and regional seismicity: Journal of Geophysical Research: Solid Earth, 86, 2825–2852.

Egorov, A., A. Bona, R. Pevzner, S. Glubokovskikh, and V. Puzyrev, 2018a, A feasibility study of time-lapse FWI on DAS VSP data acquired with permanent sources: 80th EAGE Conference and Exhibition 2018, European Association of Geoscientists & Engineers, 1–5.

Egorov, A., J. Correa, A. Bóna, R. Pevzner, K. Tertyshnikov, S. Glubokovskikh, V. Puzyrev, and B. Gurevich, 2018b, Elastic full-waveform inversion of vertical seismic profile data acquired with distributed acoustic sensors: Geophysics, 83, R273–R281.

Feng, Z., and G. T. Schuster, 2017, Elastic least-squares reverse time migration: Geophysics, 82, no. 2, S143–S157.

Fujimoto, A., T. Lim, M. Tamaki, K. Kawaguchi, T. Kobayashi, S. Haines, T. Collett, and R. Boswell, 2021, DAS 3D VSP survey at Stratigraphic Test Well (Hydrate-01): SEGJ International Symposium.

Gajewski, D., and E. Tessmer, 2005, Reverse modelling for seismic event characterization: Geophysical Journal International, 163, 276–284.

Grechka, V., P. Singh, and I. Das, 2011, Estimation of effective anisotropy simultaneously with locations of microseismic events: Geophysics, 76, no. 6, WC141–WC153.

Grechka, V., and S. Yaskevich, 2013, Inversion of microseismic data for triclinic velocity models: Geophysical Prospecting, 61, 1159–1170.

———, 2014, Azimuthal anisotropy in microseismic monitoring: A Bakken case study: Geophysics, 79, no. 1, KS1–KS12.

Guasch, L., O. C. Agudo, M.-X. Tang, P. Nachev, and M. Warner, 2020, Full-waveform inversion imaging of the human brain: NPJ Digital Medicine, 3, 1–12.

Haines, S., T. Collett, R. Boswell, T.-K. Lim, N. Okinaka, K. Suzuki, and A. Fujimoto, 2020, Gas hydrate saturation estimation from acoustic log data in the 2018 Alaska North Slope Hydrate-01 Stratigraphic Test Well: Technical results: Proceedings of the 10th International Conference on Gas Hydrates (ICGH10).

Hornman, J. C., 2017, Field trial of seismic recording using distributed acoustic sensing with broadside sensitive fibre-optic cables: Geophysical Prospecting, 65, 35–46.

Houseknecht, D. W., W. A. Rouse, S. T. Paxton, J. C. Mars, and B. Fulk, 2014, Upper Devonian-Mississippian stratigraphic framework of the Arkoma Basin and distribution of potential source-rock facies in the Woodford-Chattanooga and Fayetteville-Caney shale-gas systems: AAPG Bulletin, 98, 1739–1759.

Jarillo Michel, O., and I. Tsvankin, 2017, Waveform inversion for microseismic velocity analysis and event location in VTI media: Geophysics, 82, no. 4, WA95–WA103.

Jiang, T., G. Zhan, T. Hance, S. Sugianto, S. Soulas, and E. Kjos, 2016, Valhall dual-well 3D DAS VSP field trial and imaging for active wells, *in* SEG Technical Program Expanded Abstracts: Society of Exploration Geophysicists, 5582–5586.

Kao, H., and S. J. Shan, 2004, The source-scanning algorithm: Mapping the distribution of seismic sources in time and space: Geophysical Journal International, 157, 589–594.

Kim, K.-H., J.-H. Ree, Y. Kim, S. Kim, S. Y. Kang, and W. Seo, 2018, Assessing whether the 2017 M_w5.4 Pohang earthquake in South Korea was an induced event: Science, 360, 1007–1009.

Kiser, E., and M. Ishii, 2017, Back-projection imaging of earthquakes: Annual Review of Earth and Planetary Sciences, 45, 271–299.

Kiyashchenko, D., Y. Duan, A. Mateeva, D. Johnson, J. Pugh, A. Geisslinger, and J. Lopez, 2019, Maturing 4D DAS VSP for on-demand seismic monitoring in deepwater, *in* SEG Technical Program Expanded Abstracts: Society of Exploration Geophysicists, 5286–5289.

Kumar, A., K. Chao, R. Hammack, W. Harbert, W. Ampomah, R. Balch, and L. Garcia, 2018, Surface seismic monitoring of an active CO_2-EOR operation in the Texas Panhandle using broadband seismometers: 88th Annual International Meeting, SEG, Expanded Abstracts, 3027–3031.

Li, V., I. Tsvankin, and T. Alkhalifah, 2016, Analysis of RTM extended images for VTI media: Geophysics, 81, no. 3, S139–S150.

Li, Y., H. Wu, W. Wong, B. Hewett, Z. Liu, A. Mateeva, and J. Lopez, 2015, Velocity analysis and update with 3D DAS-VSP to improve borehole/surface seismic images: 2015 SEG Annual Meeting, Society of Exploration Geophysicists, 5285–5289.

Lindsey, N. J., H. Rademacher, and J. B. Ajo-Franklin, 2020, On the broadband instrument response of fiber-optic DAS arrays: Journal of Geophysical Research: Solid Earth, 125, e2019JB018145.

Liu, Z., J. Li, S. M. Hanafy, K. Lu, and G. Schuster, 2020, 3D wave-equation dispersion inversion of surface waves recorded on irregular topography: Geophysics, 85, no. 3, R147–R161.

Mateeva, A., J. Lopez, J. Mestayer, P. Wills, B. Cox, D. Kiyashchenko, Z. Yang, R. Detomo, and S. Grandi, 2013, Distributed acoustic sensing for reservoir monitoring with VSP: The Leading Edge, 32, 1278–1283.

Maxwell, S., 2014, Microseismic imaging of hydraulic fracturing: Society of Exploration Geophysicists.

Maxwell, S., L. Bennett, M. Jones, and J. Walsh, 2010, Anisotropic velocity modeling for microseismic processing: Part 1—Impact of velocity model uncertainty: 80th Annual International Meeting, SEG, Expanded Abstracts, 2130–2134.

Maxwell, S. C., and T. I. Urbancic, 2001, The role of passive microseismic monitoring in the instrumented oil field: Leading Edge, 20, 636–639.

McMechan, G. A., 1982, Determination of source parameters by wavefield extrapolation: Geophysical Journal International, 71, 613–628.

———, 1983, Migration by extrapolation of time-dependent boundary values: Geophysical Prospecting, 31, 413–420.

Mestayer, J., B. Cox, P. Wills, D. Kiyashchenko, J. Lopez, M. Costello, S. Bourne, G. A. Ugueto, R. Lupton, G. Solano, D. Hill, and A. Lewis, 2011, Field Trials of Distributed Acoustic Sensing for Geophysical Monitoring: SEG Annual Meeting, 4253–4257.

Moczo, P., J. Kristek, and M. Gális, 2014, The finite-difference modelling of earthquake motions: Waves and ruptures: Cambridge University Press.

Mora, P., 1988, Elastic wave-field inversion of reflection and transmission data: Geophysics, 53, 750–759.

Morse, P., and H. Feshbach, 1953, Methods of theoretical physics: 1st vol: McGraw-Hill.

Nakata, N., and G. C. Beroza, 2016, Reverse time migration for microseismic sources using the geometric mean as an imaging condition: Geophysics, 81, no. 2, KS51–KS60.

Nocedal, J., and S. Wright, 2006, Numerical optimization: Springer Science and Business Media.

Oren, C., and J. Shragge, 2019, 3D anisotropic elastic time-reverse imaging of surface-recorded microseismic data: 89th Annual International Meeting, SEG, Expanded Abstracts, 3076–3080.

———, 2020, Image-domain elastic wavefield tomography for passive data: 90th Annual International Meeting, SEG, Expanded Abstracts, 3669–3673.

———, 2021a, PS energy imaging condition for microseismic data – Part 1: Theory and applications in 3D isotropic media: Geophysics, 86, no. 2, KS37–KS48.

———, 2021b, PS energy imaging condition for microseismic data – Part 2: Sensitivity analysis in 3D anisotropic media: Geophysics, 86, no. 2, KS49–KS62.

———, 2022, Passive-seismic image-domain elastic wavefield tomography: Geophysical Journal International, 228, 1512–1529.

Plessix, R. E., 2006, A review of the adjoint-state method for computing the gradient of a functional with geophysical applications: Geophysical Journal International, 167, 495–503.

Podgornova, O., S. Leaney, S. Zeroug, and L. Liang, 2017, On full-waveform modeling and inversion of fiber-optic VSP data, *in* SEG Technical Program Expanded Abstracts 2017: Society of Exploration Geophysicists, 6039–6043.

Pratt, R. G., 1999, Seismic waveform inversion in the frequency domain, part 1: Theory and verification in a physical scale model: Geophysics, 64, 888–901.

Rawlinson, N., and M. Sambridge, 2003, Seismic traveltime tomography of the crust and lithosphere: Advances in Geophysics, 46, 81–199.

Regone, C., J. Stefani, P. Wang, C. Gerea, G. Gonzalez, and M. Oristaglio, 2017, Geologic model building in SEAM Phase II-Land seismic challenges: Leading Edge, 36, 738–749.

Rickett, J., and P. Sava, 2002, Offset and angle-domain common image-point gathers for shot-profile migration: Geophysics, 67, 883–889.

Rocha, D., P. Sava, J. Shragge, and B. Witten, 2019, 3D passive wavefield imaging using the energy norm: Geophysics, 84, no. 2, KS13–KS27.

Rocha, D., N. Tanushev, and P. Sava, 2017, Anisotropic elastic wavefield imaging using the energy norm: Geophysics, 82, no. 3, S225–S234.

Rosales, D. A., S. Fomel, B. L. Biondi, and P. C. Sava, 2008, Wave-equation angle-domain common-image gathers for converted waves: Geophysics, 73, no. 1, S17–S26.

Saenger, E. H., 2011, Time reverse characterization of sources in heterogeneous media: NDT and E International, 44, 751–759.

Sava, P., and T. Alkhalifah, 2015, Anisotropy signature in reverse-time migration extended images: Geophysical Prospecting, 63, 271–282.

Sava, P., and E. Asphaug, 2018, 3D radar wavefield tomography of comet interiors: Advances in Space Research, 61, 2198–2213.

Sava, P., and B. Biondi, 2004, Wave-equation migration velocity analysis - I: Theory: Geophysical Prospecting, 52, 593–606.

Sava, P., and S. Fomel, 2005, Wave-equation common-angle gathers for converted waves: 75th Annual International Meeting, SEG, Expanded Abstracts, 947–950.

———, 2006, Time-shift imaging condition in seismic migration: Geophysics, 71, no. 6, S209–S217.

Sava, P., and I. Vasconcelos, 2011, Extended imaging conditions for wave-equation migration: Geophysical Prospecting, 59, 35–55.

Shabelansky, A. H., A. E. Malcolm, M. C. Fehler, X. Shang, and W. L. Rodi, 2015, Source-independent full wavefield converted-phase elastic migration velocity analysis: Geophysical Journal International, 200, 952–966.

Shen, P., and W. Symes, 2008, Automatic velocity analysis via shot profile migration: Geophysics, 73, no. 5, VE49–VE59.

Shragge, J., T. Yang, and P. Sava, 2013, Time-lapse image-domain tomography using adjoint-state methods: Geophysics, 78, no. 4, A29–A33.

Sirgue, L., and R. G. Pratt, 2004, Efficient waveform inversion and imaging: A strategy for selecting temporal frequencies: Geophysics, 69, 231–248.

Sloan, E. D., and C. A. Koh, 2007, Clathrate hydrates of natural gases: CRC press.

Sun, J., Z. Xue, S. Fomel, T. Zhu, and N. Nakata, 2016, Full waveform inversion of passive seismic data for sources and velocities: 86th Annual International Meeting, SEG, Expanded Abstracts, 35, 1405–1410.

Symes, W., and J. Carazzone, 1991, Velocity inversion by differential semblance optimization: Geophysics, 56, 654–663.

Symes, W. W., 2008, Migration velocity analysis and waveform inversion: Geophysical prospecting, 56, 765–790.

Tang, Y., and G. Ayeni, 2015, Efficient line search methods for multiparameter full wave-field inversion: U.S. Patent 20, 150, 323, 689.

Tarantola, A., 1984, Linearized inversion of seismic reflection data: Geophysical prospecting, 32, 998–1015.

Thomsen, L., 1986, Weak elastic anisotropy: Geophysics, 51, 1954–1966.

Tsvankin, I., 1997, Anisotropic parameters and P-wave velocity for orthorhombic media: Geophysics, 62, 1292–1309.

———, 2012, Seismic signatures and analysis of reflection data in anisotropic media: Society of Exploration Geophysicists.

Vernik, L., and X. Liu, 1997, Velocity anisotropy in shales: A petrophysical study: Geophysics, 62, 521–532.

Vernik, L., and A. Nur, 1992, Ultrasonic velocity and anisotropy of hydrocarbon source rocks: Geophysics, 57, 727–735.

Virieux, J., and S. Operto, 2009, An overview of full-waveform inversion in exploration geophysics: Geophysics, 74, WCC1–WCC26.

Waldhauser, F., and W. L. Ellsworth, 2000, A double-difference earthquake location algorithm: method and application to the northern Hayward fault, California: Bulletin of the Seismological Society of America, 90, 1353–1368.

Wang, H., and T. Alkhalifah, 2018, Microseismic imaging using a source function independent full waveform inversion method: Geophysical Journal International, 214, 46–57.

Warner, M., A. Ratcliffe, T. Nangoo, J. Morgan, A. Umpleby, N. Shah, V. Vinje, I. Štekl, L. Guasch, C. Win, G. Conroy, and A. Bertrand, 2013, Anisotropic 3D full-waveform inversion: Geophysics, 78, no. 2, R59–R80.

Warpinski, N., P. Branagan, R. Peterson, S. Wolhart, and J. Uhl, 1998, Mapping hydraulic fracture growth and geometry using microseismic events detected by a wireline retrievable accelerometer array: Presented at the SPE Gas Technology Symposium.

Weibull, W., and B. Arntsen, 2013, Automatic velocity analysis with reverse-time migration: Geophysics, 78, no. 4, S179–S192.

Weingarten, M., S. Ge, J. W. Godt, B. A. Bekins, and J. L. Rubinstein, 2015, High-rate injection is associated with the increase in u.s. mid-continent seismicity: Science, 348, 1336–1340.

Weiss, R. M., and J. Shragge, 2013, Solving 3D anisotropic elastic wave equations on parallel GPU devices: Geophysics, 78, no. 2, F7–F15.

Witten, B., and J. Shragge, 2015, Extended wave-equation imaging conditions for passive seismic data: Geophysics, 80, no. 6, WC61–WC72.

———, 2017a, Image-domain velocity inversion and event location for microseismic monitoring: Geophysics, 82, no. 5, KS71–KS83.

———, 2017b, Microseismic image-domain velocity inversion: Marcellus Shale case study: Geophysics, 82, no. 6, KS99–KS112.

Yan, J., and P. Sava, 2008, Isotropic angle-domain elastic reverse-time migration: Geophysics, 73, no. 6, S229–S239.

———, 2009, Elastic wave-mode separation for VTI media: Geophysics, 74, no. 5, WB19–WB32.

———, 2011, Elastic wave-mode separation for tilted transverse isotropy media: Geophysical Prospecting, 60, 29–48.

Yan, R., and X.-B. Xie, 2012, An angle-domain imaging condition for elastic reverse time migration and its application to angle gather extraction: Geophysics, 77, no. 5, S105–S115.

Yang, J., and H. Zhu, 2019, Locating and monitoring microseismicity, hydraulic fracture and earthquake rupture using elastic time-reversal imaging: Geophysical Journal International, 216, 726–744.

Yang, T., and P. Sava, 2009, Wave-equation migration velocity analysis using extended images, *in* SEG Technical Program Expanded Abstracts 2009: Society of Exploration Geophysicists, 3715–3719.

———, 2015, Image-domain wavefield tomography with extended common-image-point gathers: Geophysical Prospecting, 63, 1086–1096.

Yang, T., J. Shragge, and P. Sava, 2013, Illumination compensation for image-domain wavefield tomography: Geophysics, 78, no. 5, U65–U76.

Young, C., J. Shragge, W. Schultz, S. Haines, C. Oren, J. Simmons, and T. Collet, 2022, Advanced distributed acoustic sensing vertical seismic profile imaging of an Alaska North Slope gas hydrate field: submitted to Energy & Fuels.

Yurikov, A., K. Tertyshnikov, R. Isaenkov, E. Sidenko, S. Yavuz, S. Glubokovskikh, P. Barraclough, P. Shashkin, and R. Pevzner, 2021, Multiwell 3D distributed acoustic sensing vertical seismic profile imaging with engineered fibers: CO2CRC Otway Project case study: Geophysics, 86, no. 6, D241–D248.

Zhang, H., and C. H. Thurber, 2003, Double-difference tomography: The method and its application to the Hayward fault, California: Bulletin of the Seismological Society of America, 93, 1875–1889.

APPENDIX

PERMISSIONS FOR CHAPTERS

A.1 Permission from journals

This appendix includes the copyright permissions from *Geophysics* (Figure A.1) and *Geophysical Journal International* (Figure A.2) for use of the published papers incorporated as chapters in this thesis. The URL that shows the details of copyright permissions from *Geophysics* is https://library.seg.org/page/policies/open-access. The URL that shows the details of copyright permissions from Oxford University Press, publisher for *Geophysical Journal International*, is https://global.oup.com/academic/rights/permissions/autperm/?cc=us&lang=en&.

Traditional publication (including green open access)

- No author publication charge (APC) is levied, although payment of mandatory page charges are assessed and payment of voluntary charges is requested. Relief from mandatory charges may be requested under SEG's hardship relief policy.
- Copyright is transferred to SEG.
- Authors/employers retain proprietary rights such as the right to patentable subject matter and the right to make oral presentation of the work with full citation and proper copyright acknowledgment.
- Authors/employers enjoy the right to prepare and hold copyright in derivative publications based on the paper provided that the derivative work is published subsequent to the official date of the original paper's publication by SEG.
- Authors/employers may post a final accepted version of the manuscript or the final SEG-formatted version (book chapters excluded) on authors' personal websites, employers' websites, or in institutional repositories operated and controlled exclusively by authors' employers provided that:
    1. the SEG-prepared version is presented without modification;
    2. copyright notice and a full citation appear with the paper;
    3. a link to the SEG version of record in the SEG Library using the digital object identifier (DOI) and a permalink is provided;
    4. the posting is noncommercial in nature, and the paper is made available to users without charge; and
    5. that notice be provided that use is subject to SEG terms of use and conditions.
- Authors/employers may not post their articles in an institutional repository or other site in which the content is required to carry or is implied as carrying a license contrary to SEG copyright and terms of use and terms of this policy.
- Authors may reuse all or part of their papers published with SEG in a thesis or dissertation that authors write and are required to submit to satisfy criteria of degree-granting institutions.
- Authors/employers have the nonexclusive right, after publication by SEG, to give permission to third parties to republish print versions of the paper, or excerpts therefrom, without obtaining permission from SEG, provided that:
    1. the SEG-prepared version is not used for this purpose;
    2. the paper is not republished in another journal or book; and
    3. the third party does not charge a fee. Permission must be obtained from SEG for other republication of the paper.

Figure A.1 A screenshot granting permission (highlighted in yellow) from *Geophysics*.

After publication

After publication you may reuse the following portions of your content without obtaining formal permission for the activities expressly listed below:

- one chapter or up to 10% of the total of your single author or co-authored book,
- a maximum of one chapter/article from your contribution to an edited book or collection (e.g. Oxford Handbooks),
- a maximum of one chapter/article of your contribution to an online only, or digital original publication, or
- three figures/illustrations/tables of your own original work

OUP is pleased to grant this permission for the following uses:

- posting on your own personal website or in an institutional or subject based repository after a **12 month** period for **Science and Medical** titles and a **24 month** period for **Academic, Trade and Reference** titles;
- inclusion in scholarly, not-for-profit derivative reuses, (these can include the extension of your contribution to a book-length work, or inclusion in an edited collection of your own work, or any work of which you are an author or editor);
- reproduction within coursepacks or e-coursepacks for your own teaching purposes, (with the proviso that the coursepacks are not sold for more than the cost of reproduction);
- inclusion within your thesis or dissertation.

Permission for these reuses is granted on the following conditions:

- that the material you wish to reuse is your own work and has already been published by OUP;
- that the intended reuse is for scholarly purposes, for publication by a not-for-profit publisher;
- that full acknowledgement is made of the original publication stating the specific material reused [pages, figure numbers, etc.], [Title] by/edited by [Author/editor], [year of publication], reproduced by permission of Oxford University Press [link to OUP catalogue if available, or OUP website];
- In the case of joint-authored works, it is the responsibility of the authors to obtain permission from co-authors for the work to be reuse/republished.
- that reuse on personal websites and institutional or subject based repositories includes a link to the work as published in an OUP online product (e.g. Oxford Scholarship Online), and/or or to the OUP online catalogue entry; and that the material is not distributed under any kind of Open Access style licences (e.g. Creative Commons) which may affect the Licence between yourself and OUP.

Figure A.2 A screenshot granting permission (highlighted in yellow) from Oxford University Press, publisher for *Geophysical Journal International*.

A.2 Permission for field data set

I include a copy of the email exchanged with company representatives who granted permission for the use of the North Alaska DAS 3D VSP data set presented in Chapter 5 of this dissertation.

Fwd: [EXTERNAL] Re: new item for JOGMEC approval: PhD thesis chapter for CSM student

From: shimoda-naoyuki@jogmec.go.jp
Date: December 24, 2021 at 3:59:48 AM EST
To: "Haines, Seth S" <shaines@usgs.gov>
Cc: okinaka-norihiro <okinaka-norihiro@jogmec.go.jp>, "Collett, Timothy S" <tcollett@usgs.gov>
Subject: [EXTERNAL] Re: new item for JOGMEC approval: PhD thesis chapter for CSM student

This email has been received from outside of DOI - Use caution before clicking on links, opening attachments, or responding.

Thank you for wainting.
I have got the both approvals.

All the best,

差出人: Haines, Seth S <shaines@usgs.gov>
送信日時: 2021年12月16日 9:16
宛先: 下田 直之 <shimoda-naoyuki@jogmec.go.jp>
CC: 沖中 教裕 <okinaka-norihiro@jogmec.go.jp>; Collett, Timothy S <tcollett@usgs.gov>
件名: new item for JOGMEC approval: PhD thesis chapter for CSM student

Hello Shimoda-san,
I'm attaching a new publication for which we would like to request JOGMEC publication approval. Can you please try to obtain this?

The document is a chapter from the PhD thesis of Can Oren. It is the same work that he presented to you and the JOGMEC group recently. It is also the same work that is presented in the journal manuscript that I have previously sent you for approval -- these documents are nearly identical. But I assume that separate approval is needed, because it is for two separate publication types.

In addition, we are eagerly awaiting JOGMEC approval for Can's journal manuscript.

Thank you for your help with these documents.

thanks,
Seth

Figure A.3 Permission granted by JOGMEC for the use of the North Alaska DAS 3D VSP data set presented in Chapter 5.